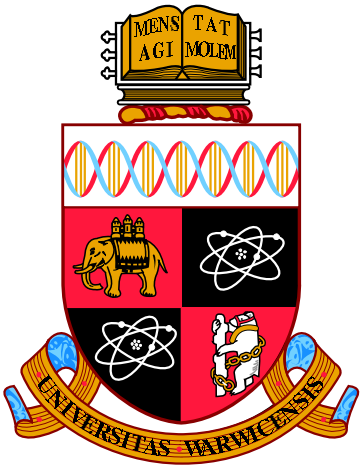

Muon and Neutron Studies of Unconventional Superconductors

by

Natalia Anna Parzyk

Thesis

Submitted to the University of Warwick

for the degree of

Doctor of Philosophy

Department of Physics

November 2014

THE UNIVERSITY OF WARWICK

Contents

List of Tables

List of Figures

Acknowledgments

I would like to thank my supervisors Prof. Don M^{c}K. Paul and Prof. Geetha Balakrishnan for inspiration. I am grateful for the experience and knowledge they shared with me. Don, without your mentorship, immense knowledge, invaluable advices and Scottish sense of humour this thesis would not be possible thank you. Geetha, I am truly grateful for your patience, encouragement and guidance.

Special thanks to Dr. Adrian Hillier (ISIS, RAL) for inspiring conversations, experience and knowledge about muons. I am also grateful to Dr. Ravi P. Singh for valuable advices and knowledge he shared. I would also like to thank Dr. Charles Dewhurst (ILL) for his advices and knowledge about small angle neutron scattering. I would like to extend my gratitude to Dr. Martin Lees for his experience and knowledge about magnetic and transport measurements and to Dr. Oleg Petrenko for introducing me to Laue diffraction technique. Many parts of this thesis would not been possible without technical support of Tom Orton, thank you. Special thanks to Dr. Dean Keable for his experience with single crystal X-ray diffraction and Dr. Steven York for his expertise in EDX analysis.

I am extremely grateful to friends from the department, members and former members of Superconductivity and Magnetism group (as well as Nano-Silicon group) for creating intellectually stimulating environment. I am also in debt to friends and staff from Wolfson Research Exchange for creating enjoyable thesis writing place. Special thanks to my friends from Warwick Mountains for many chances to enjoy the tranquillity of mountains together. Words cannot express how grateful I am for having amazing friends. Special thanks, for everything, to Catarina and Nessa. I

am also thankful to Agnieszka, Emilia, Karolina, Adam, Kasia, Nick, Amna, Ania, Mmaki and so many others people who crossed my path and made me who and where I am. Special thanks to Nick for taking the time to proofread most of this thesis. I would also like to thank Gareth and Cookie for answering countless questions about English grammar and not giving up hope that I would eventually learn how to write in their language :)

To God and prof. Richard Feynman (and his *Lectures in Physics*), without them I am sure, I would not have turned my attention towards physics.

Last but not least I would like thank my parents: Gabriela and Tadeusz for the amazing opportunities they have been giving me over the years, and my brother Franciszek for being part of my life.

My PhD and the work presented in thesis thesis would not have been possible without financial support of EPSRC for which I am grateful.

Declarations

All experiments presented in this thesis were carried out by me or under my directions, except where explicitly stated. The experiments were performed in the Department of Physics, University of Warwick, in the Institut Laue-Langevin and in ISIS, Rutherford Appleton Laboratory. For experiments in the central facilities, I was either the sole experimentalist or a leading member of the experimental team. Those experiments were performed with the assistance of an instrument scientist, Dr. Adrian Hillier in ISIS and Dr. Charles Dewhurst in ILL.

The single crystal samples of Ru_7B_3, $Ru_7{}^{11}B_3$ and ZrB_{12} were made by Prof. G. Balakrisknan and Dr. R.P. Singh. Polycrystalline α-BiPd was produced by Dr. R.P. Singh. Polycrystalline $ZrNi_2Ga$ and $NbNi_2Ga$ were supplied by Dr. A.D. Hillier. Single crystal CCD X-ray diffraction for Ru_7B_3 crystal were performed by Dr. D. Keable. EDX on SEM measurements for Ru_7B_3 crystal were carried out by Dr. S. York.

No part of this thesis has been submitted for examination at any other institution. Parts of the work described in this thesis have been published in the following articles:

R.P. Singh, N.A. Parzyk, M.R. Lees, D.M^{c}K. Paul, and G. Balakrishnan. Crystal growth and properties of the non-centrosymmetric superconductor, Ru_7B_3. *J. Cryst. Growth*, 395:22, 2014.

A.D. Hillier, N. Parzyk, and D.M^{c}K. Paul. Probing the superconducting state of the Heusler superconductor: $ZrNi_2Ga$. ArXiv e-prints, June 2012, 1206.1182.

Parts of the work have been presented by the thesis author as an oral presentation during following conferences:

Frontiers of Muon Spectroscopy, Oxford 2012: *Unconventional superconductivity in non - centrosymmetric* Ru_7B_3

CMMP11, Manchester 2011 : *Unconventional superconductivity in the Heusler compound* $ZrNi_2Ga$ *a* μSR *study*

Abstract

The mechanism of unconventional superconductivity is still mysterious, despite extensive studies. Muon spectroscopy (μSR) and small angle neutron scattering (SANS) studies of some unconventional superconductors were carried out. The NCS superconductors: Ru_7B_3 and α-BiPd, Heusler compounds: $ZrNi_2Ga$ and $NbNi_2Ga$ and the marginal superconductor ZrB_{12} were investigated. This thesis reports new phenomena observed in those systems and advances the knowledge of the ground state properties of unconventional superconductors.

Polycrystalline samples and single crystals of the non-centrosymmetric superconductor (NCS) Ru_7B_3 were studied. Evidence for time-reversal symmetry (TRS) breaking in the superconducting state of Ru_7B_3 were found using μSR. So far, it is the third known NCS superconductor which breaks TRS. Potentially multigap behaviour was observed. The presence of two distinct superconducting gaps was suggested in polycrystalline Ru_7B_3 using μSR. Additionally, SANS and μSR measurements indicate unusual behaviour for the observed distorted hexagonal flux line lattice (FLL) in Ru_7B_3, yet the nature of this behaviour remains inconclusive.

μSR studies of another NCS superconductor α-BiPd give evidence that two superconducting gaps are present in α-BiPd, either two s-wave gaps or s-wave and d-wave gaps exist in α-BiPd. Additionally, unusual temperature evolution of the upper critical field of α-BiPd was observed.

Two superconducting compounds belonging to the Heusler family, $ZrNi_2Ga$ and $NbNi_2Ga$, were investigated using μSR. Temperature dependence of the penetration depth of $ZrNi_2Ga$ suggests an s-wave, conventional behaviour in this superconductor. Evidence of a structural change in the morphology of the FLL was observed: a square FLL potentially exists at low temperatures and a hexagonal FLL is present closer to T_c. Additionally, μSR experiments suggest that TRS is preserved in both measured Heusler compounds.

SANS studies of a marginal, low-κ superconductor ZrB_{12} were carried out. SANS studies were performed in a range of temperature and magnetic field so to access different parts of the superconducting phase diagram of ZrB_{12}. A square vortex lattice was found in all measured temperatures and fields.

Abbreviations

AC	alternating current
AFM	antiferromagnetic
BCS	Bardeen – Cooper – Schrieffer
CCD	charged-coupled device
DC	direct current
EDS	energy-dispersive spectrometer
EDX	energy-dispersive X-ray spectroscopy
FC	field cooled
fcc	face-centred cubic
FFLO	Fulde - Fernell - Larkin - Ovchinnikov
FLL	flux line lattice
FM	ferromagnetic
GL	Ginzburg - Landau
HF	heavy fermion
ILL	Institut Laue-Langevin
KT	Kubo - Toyabe
LF	longitudinal field
MPMS	magnetic property measurement system
MR	magnetoresistance
NCS	non-centrosymmetric

PPMS	physical property measurement system
RRR	residual resistivity ratio
SANS	small angle neutron scattering
SEM	scanning electron microscopy
SOC	spin-orbit coupling
SQUID	superconducting quantum interference device
TF	transverse field
TRS	time-reversal symmetry
VL	vortex lattice
WHH	Werthamer - Helfand - Hohenberg
XRD	X-ray diffraction
ZF	zero field
ZFC	zero field cooled
μSR	muon spectroscopy

Chapter 1

Preface

> *Certainly, the phase space of materials to explore is astronomical, and it will definitely take a lot of imagination, both from theory and experiment, to explore its infinite richness [1].*
>
> M.R. Norman: *Unconventional superconductivity*

Superconductivity is a fascinating and complex phenomenon. Over 100 years ago Heike Kamerlingh-Onnes made a discovery which continues to inspire many generations of scientists [2]. Kamerlingh-Onnes discovered superconductivity in 1911 but it was not till the late 1950's that Bardeen, Cooper and Schrieffer (BCS) reported a microscopic theory of superconductivity [3]. The BCS theory seemed to fully explain superconductivity, but based on this theory, many concluded that superconductivity cannot exist at temperatures greater than 25-30 K. Several years passed since Kamerlingh-Onnes discovery before superconductors with relatively high transition temperature were found. It was not till 1980's when discovery of superconductivity in a family of cuprates was reported at temperatures greater than liquid nitrogen boiling point [2, 4]. Shortly after, superconductivity in many new families was reported. Cuprates and many other superconducting compounds cannot be simply described by the BCS theory. They were then called *unconventional superconductors*.

In pursuit of higher critical temperatures and higher critical currents, new classes of superconductors emerged. Theoretical and experimental efforts were undertaken to fully understand the mechanism of superconductivity [1, 2, 5]. A myriad of unconventional superconductors have been identified so far and the current stage of research in this area is well summarized by M.R. Norman [1]. Extensive studies of cuprates, molecular superconductors, iron-based compounds or heavy fermions have been performed to understand unconventional superconductivity. This thesis presents studies of a few compounds which do not belong to those main classes of unconventional superconductors. Novel superconducting families were studied. Studies of exotic phenomena, which so far were observed only in a few compounds, were undertaken: evidence of TRS breaking, presence of a square vortex lattice and evidence for a non-BCS character of Cooper pairs were observed.

A substantial part of this work concerns the flux line lattice (FLL) in superconductors. In a mixed state of type-II superconductor magnetic field can penetrate inside superconductor in form of vortices arranged in a periodic FLL. The majority of superconductors are type-II superconductors so a full understanding of the nature of the FLL is crucial. Studies of the FLL provide informations about the fundamental length-scales in superconductors: the coherence length and penetration depth, hence the superfluid density of the superconductor can be examine and the nature of the Fermi surface can be investigated. The powerful techniques to study the FLL in superconductors are small angle neutron scattering (SANS) and muon spectroscopy (μSR), which provides information about the FLL over a range of temperatures and magnetic fields. The symmetry of the FLL can be directly determined from the SANS diffraction pattern [6, 7]. μSR can measure local magnetic fields as low as 0.1 G [8], so studies of the field distribution of the FLL can be performed. μSR experiments provide information about the absolute values of the energy of the superconducting gap. Both techniques measure the superfluid density of a superconductor. μSR measures a field distribution within the FLL and SANS provides information about

the spatial variation of the magnetic field of the FLL so the methods are complementary [9]. Additionally, μSR is an excellent probe of TRS breaking in superconductors because unlike many other techniques, μSR does not require a magnetic field to be applied to perform the measurements [10].

Unconventional superconductivity is possible in an enormous quantity of materials. Those materials belong to several chemical classes and develop various exotic phenomena, not accounted for in the BCS theory. This thesis presents muon and neutron studies of some unconventional superconductors. This thesis reports time-reversal symmetry breaking in a NCS superconductor (so far it was reported only in two other NCS superconducting compounds), the presence of a non s-wave order parameter of Cooper pairs, as well as the extensive studies of the flux line lattices in superconductors. It is a valuable contribution to the challenging undertaking to understand unconventional superconductivity.

1.1 Thesis overview

Chapter 2 sets the scene of this thesis and contains a brief overview of superconductivity with a focus on unconventional phenomena. Chapter 3 introduces experimental techniques used during this research. Particular attention is given to μSR and SANS, which were the main techniques used in this work. Chapters 4 and 5 present the superconducting properties of a couple of non-centrosymmetric compounds: Ru_7B_3 and α-BiPd. Chapter 4 presents extensive μSR and SANS studies of Ru_7B_3 and Chapter 5 shows μSR studies of α-BiPd. Another interesting family of compounds are Heusler compounds and superconducting properties of two Heusler materials, $ZrNi_2Ga$ and $NbNi_2Ga$, are discussed in Chapter 6. Chapter 7 reports SANS diffraction studies of a low-κ superconductor ZrB_{12}.

Finally, conclusions are reported in Chapter 8, suggestions of further work are also included.

Chapter 2

Background

2.1 Superconductivity – an overview

Warm sun was shining in July 1908, when Heike Kamerlingh-Onnes liquidized helium, which provided a method of cooling materials down to temperatures close to absolute zero. He then measured the behaviour of various elements at low temperatures and in 1911 he found that electrical resistance vanishes in mercury below 4.2 K. Kamerling-Onnes had discovered a new state of matter - superconductivity [2]. In 1933, Walther Meissner and Robert Ochsenfeld observed that an applied magnetic field is expelled from a superconducting material, later called *the Meissner effect* [2].

It was not until 1957 that a microscopic theory of superconductivity would emerge. The work of Bardeen, Cooper and Schrieffer (BCS) which describes well conventional superconductors, is so far the only complete microscopic description of superconducting behaviour [3]. A few years before BCS presented their model, in 1950, Ginzburg and Landau (GL) proposed a phenomenological approach to superconductivity, which was based on Landau's theory of second order phase transitions [11]. They defined an order parameter $\psi(\mathbf{r})$, where $|\psi(\mathbf{r})|^2$ represents the density of the superconducting electrons. GL introduced an expansion of the Gibbs free energy, which describes not only isotropic, conventional superconductors,

but also represents superconductors with a spatially varying superfluid density. The penetration depth (λ), the coherence length (ξ) and the critical fields are 'natural' parameters in the GL theory and they can be derived with suitable boundary conditions. For details of the GL theory see [2, 11–13] and references therein.

Superconductors can be distinguished based on their value of κ, a parameter defined by GL as:

$$\kappa = \frac{\lambda}{\xi}, \tag{2.1}$$

If κ of a superconducting material is lower than $1/\sqrt{2}$, it is a type I superconductor, if $\kappa > 1/\sqrt{2}$, it is a type II superconductor. An interesting behaviour was predicted for materials with κ close to the boundary value, an attractive interaction between vortices can appear in so called *type 1.5* superconductors, for details see [14–16].

Below a critical temperature T_c and in the presence of an applied magnetic field, which does not exceed a critical field H_c, a type I superconductor is in the Meissner state. The behaviour of a superconducting material in an applied magnetic field depends on the shape and orientation of the sample, so demagnetization effects always need to be considered. When the magnetic field approaches H_c, the material, to minimize its free energy, enters an intermediate state. To maintain the value of the average internal magnetic field below the H_c value, in the intermediate state, normal and superconducting domains coexist over the surface of a sample [2]. Hence demagnetization effects play an important role when the applied magnetic field is close to H_c.

A type II superconductor is in the Meissner state only when the applied magnetic field is less than the lower critical field H_{c1} value. In magnetic fields higher than H_{c1} (but lower that the upper critical field H_{c2}) the superconductor enters the mixed state, where the normal and superconducting states coexist. A type II superconductor in the mixed state does not completely expel the magnetic field from its interior. When λ is larger than ξ, the magnetic field penetrates the material in the form of

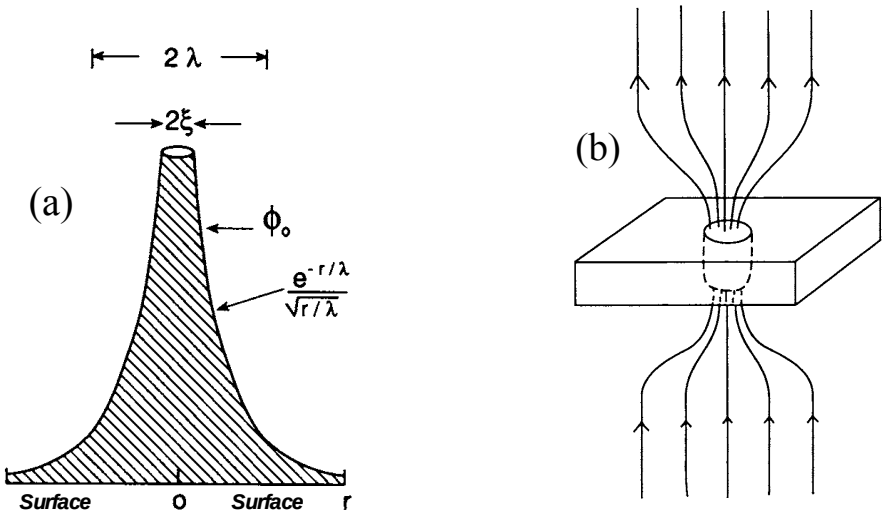

Figure 2.1: (a) An individual vortex of magnetic flux. Fundamental superconducting parameters, ξ and λ are marked and the exponential decay of the magnetic field is indicated. (b) Lines of magnetic field passing through a single vortex. Taken from [2].

magnetic flux vortices surrounded by a shielding electric current [17]. Abrikosov showed using the GL theory that each vortex contains a quantized unit of a magnetic flux, a flux quantum Φ. The highest magnetic field is in the vortex core, which has a radius, $r = \xi$. The value of the effective radius of a vortex is given by λ. When $\xi < r > \lambda$, a magnetic field and a shielding current coexist, and at distances larger than λ the magnetic field exponentially decreases towards zero (see Fig. 2.1) [2].

The shielding current is circulating in the same direction for each vortex so the interactions between the vortices are repulsive. A periodic, hexagonal flux line lattice (FLL) is the configuration with the lowest free energy so it is the most favourable vortex arrangement [12]. In a hexagonal FLL the distance between nearest neighbours is the largest so the free energy is minimized. But the free energy for the formation of a square lattice is only 2 % higher [18], so in some superconductors a square FLL is present. A square symmetry of the FLL was directly observed using small angle neutron scattering (SANS), for example in: Sr_2RuO_4 [19], $Nd_{1.85}Ce_{0.15}CuO_4$ [20], borocarbides: $ErNi_2B_2C$ [21], $TmNi_2B_2C$ [22], YNi_2B_2C [23].

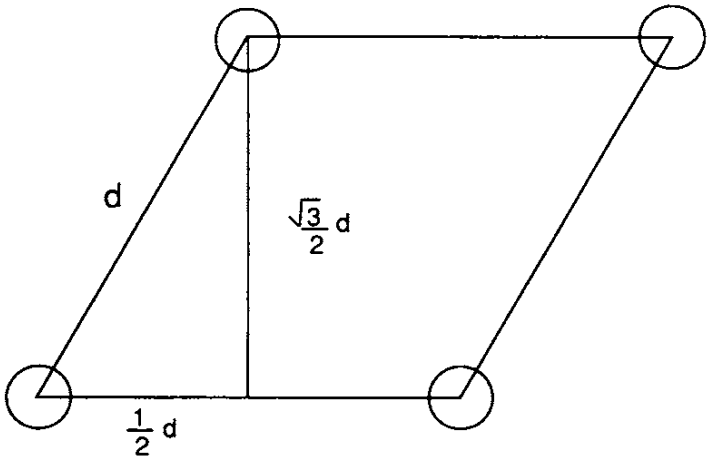

Figure 2.2: Unit cell for a hexagonal FLL. The separation between the vortices in a hexagonal lattice (d) is marked in the text with the symbol: $d_{\triangle}$. Taken from [2].

One unit cell contains one flux quantum ($\phi_0 = 2.068 * 10^{-15}$ Wb) so the separation between vortices in a hexagonal lattice ($d_{\triangle}$) is related to the average field inside the superconductor (B_{in}) as [2]:

$$B_{\text{in}} = \frac{2\Phi}{\sqrt{3}d_{\triangle}^2} \tag{2.2}$$

and $1/2\sqrt{3}d_{\triangle}^2$ is the area of the FLL cell (shown on Fig. 2.2). The distance between vortices in the square lattice ($d_{\square}$) can be described as:

$$d_{\square} = \sqrt{\frac{\Phi}{B_{\text{in}}}} \tag{2.3}$$

In a low magnetic field, isolated vortices can exist and with an increase of the applied magnetic field additional vortices form. If the concentration of the vortices further increase, they begin to overlap with each other (see Fig. 2.3) and eventually the magnetic field fully penetrates the material, when the applied magnetic field exceeds the upper critical field H_{c2} [2, 17].

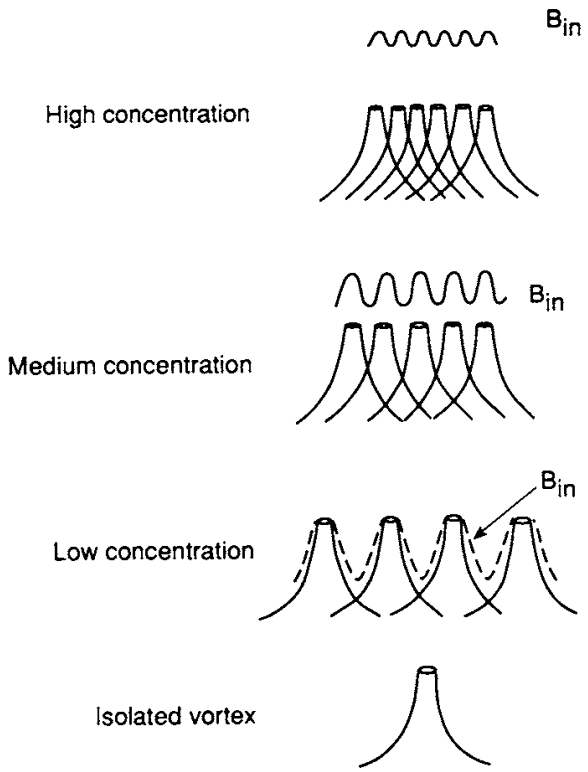

Figure 2.3: Schematic illustration of the distribution of the vortices in a superconductor. With increasing magnetic field, more vortices exist and the vortices become to overlap. Taken from [2].

2.2 Unconventional superconductors

Several years after Kamerlingh-Onnes's discovery and long after the BCS and GL theories had been established, in 1986 Bednorz and Müller observed superconductivity in cuprate compounds [2]. Bednorz and Müller's studies led to the discovery of so called *high temperature superconductors* – materials with T_c higher than 77 K, the boiling point of liquid nitrogen [4]. Few years earlier, in 1979, Steglich *et al.* investigated $CeCu_2Si_2$ and identified the first material where the coexistence of superconductivity and magnetism occurs [24]. Also in 1979, the presence of superconductivity in organic compounds was reported [25]. Superconductivity in these new superconductors could not be explained by the BCS theory and a new era of superconducting research had begun.

To talk about unconventional superconductivity one needs to define the terms - *conventional* and *unconventional* superconductor. Conventional superconductors, are well described by the BCS theory, and are isotropic, s-wave superconductors, where Cooper pairs are formed due to electron-phonon interaction (see Section 2.2.1). A conventional superconductor breaks only gauge symmetry due to electrons pairing, while an unconventional superconductor may break other symmetries as well, i.e. time reversal symmetry, spin rotation symmetry or translational symmetry of a crystal lattice might be broken. Symmetry breaking may cause an appearance of the nodes in the superconducting gap function [26, 27]. Unconventional superconductors displays phenomena not anticipated in the framework of the BCS theory [1].

2.2.1 BCS theory

The formation of the electron pairs, so called Cooper pairs is a fundamental concept of the BCS theory [3]. Below T_{c}, an attractive interaction appears between two electrons with opposite spins and Cooper pairs are created due to this, electron - phonon mediated interaction. The waveforms of the Cooper pairs are phase coherent, so one wavefunction can represent all Cooper pairs [28]. The BCS theory shows that the transition to the superconducting state is energetically favourable for materials because the energy of a paired state is lower than the normal ground state energy. There are many Cooper pairs in the ground state of a superconductor, but a full Hamiltonian can be constructed so the behaviour of a material in the superconducting state can be evaluated.

An energy gap Δ is a minimum energy needed to bring a superconductor to an excited state, i.e. the breaking of Cooper pairs results in an excited state. Δ can be derived [29] (see Eq. 2.4) and calculated numerically, the temperature dependence of the BCS gap can be obtained (see Fig. 2.4).

$$1 = \mathrm{N}(0)\mathrm{V} \int_0^{\hbar\omega_{\mathrm{D}}} \frac{\mathrm{d}\epsilon}{(\epsilon^2 + |\Delta|^2)^{\frac{1}{2}}} \tanh\left(\frac{(\epsilon^2 + |\Delta|^2)^{\frac{1}{2}}}{k_{\mathrm{B}}T}\right), \tag{2.4}$$

Figure 2.4: Temperature dependence of the BCS energy gap, Δ. Taken from [12].

where N(0) is the density of states at the Fermi surface, V is an attractive interaction between electrons, which represents the strength of the electron-phonon coupling, ϵ is the energy of electrons, k_{B} is the Boltzmann constant, $\hbar\omega_{\mathrm{D}}$ is the Debye energy of phonons in the lattice.

The energy gap near T_{c} is $|\Delta| = 0$. If the strength of the electron-phonon interaction is assumed to be in the weak-coupling limit [12], then from Eq. 2.4, the relation between T_{c} and $|\Delta|$ can be written as:

$$\frac{\Delta(0)}{k_{\mathrm{B}}T_c} \;=\; \frac{2}{1.13} \;=\; 1.764\,, \tag{2.5}$$

Eq. 2.4 and Fig. 2.4 assume the presence of a weak-coupling and a spherical Fermi surface, but it is a good approximation for many superconductors [12, 29].

The BCS theory was later considered and expanded by several scientists: Gor'kov, Bogoliubov, de Gennes, Eliashberg to name a few, and all those works constitute a comprehensive theory of conventional superconductivity [29]. This section only briefly introduces the most important concepts of the BSC theory, its implications and an extended formalism can be found in, for example: [2, 12, 29] and references therein.

2.2.2 Superconductors with broken time-reversal symmetry

Symmetry has inspired people for centuries [30, 31]. Time reversal symmetry (TRS) breaking in superconductors is a fascinating phenomena, which so far was experimentally observed only in a few compounds. In superconductor with broken TRS, either the spin or orbital moments of the Cooper pairs are non-zero [26, 32, 33]. Hence a superconductor with broken TRS has a multicomponent order parameter with additional degrees of freedom, which represent spin or orbital degeneracy of the Cooper pairs. The appearance of a small spontaneous magnetic field, for a superconductor in zero field is evidence that TRS is broken [34]. A few possible sources cause the presence of this spontaneous magnetic field. Supercurrents induced around magnetic impurities and domain walls causes a small spatial variation of the order parameter, which manifests in a non-zero spin or orbital momentum of Cooper pair and hence TRS is broken [32]. The non-unitary ground state of a superconductor, which might be enhanced by a finite hyperfine field also breaks TRS in a superconductor [35]. Muon spin relaxation in zero field is a powerful probe of TRS breaking [10]. Unlike many other techniques, μSR does not require an applied magnetic field to carry out measurements and muons are an extremely sensitive probe of a magnetic field (down to 0.1 G) [8], so the very small spontaneous magnetic field, due to broken TRS, can be detected. TRS breaking has been directly observed using μSR only in a few compounds: Sr_2RuO_4 [34], skutterudites: $PrOs_4Sb_{12}$ [32] also when doped with La on Pr site and Ru on Os site (for certain concentrations) [36], $PrPt_4Ge_{12}$ [35], heavy fermions: B phase of UPt_3 [37], $(U_{1-x}Th_x)Be_{13}$ [38] a couple of non-centrosymmetric compounds Re_6Zr [39] and $LaNiC_2$ [10] and also in centrosymmetric $LaNiGa_2$ [40]. The Anderson theory predicts that when inversion symmetry is broken, spin-singlet pairing is present, but if TRS breaking appears, a spin-triplet ground state will be favoured. So in the NCS superconductors with broken TRS, a mixture of a spin-singlet and spin-triplet states may be present [41]. In the muon spin relaxation experiments, muons implanted in the material interact with the local magnetic

field and shortly after they decay to a positron and two neutrinos. The positron is emitted preferentially in the directions of the muon spin at the time of decay. For a superconductor with broken TRS, the time evolution of a muon spin polarization in the superconducting and normal states are shown in Fig. 2.5(a). The time evolution of the muon spin polarization for a superconductor measured using the muon spin relaxation in zero field (ZF-μSR) is described well by the function (Eq. 2.6) with Kubo - Toyabe depolarisation.

$$G_z(t) = A_0 G_z^{KT}(t) \exp(-\Lambda t) + A_{bcg} \tag{2.6}$$

where A_0 is an initial asymmetry of the muon polarisation, Λ is an electronic relaxation rate, A_{bcg} is a background contribution and the function G_z^{KT} is the Kubo - Toyabe (KT) function [42]:

$$G_z^{KT}(t) = \left[\frac{1}{3} + \frac{2}{3}(1 - \Delta_{KT}^2 t^2) \exp\left(-\frac{{\Delta_{KT}}^2 t^2}{2}\right)\right] \tag{2.7}$$

where Δ_{KT}/γ_μ is the width of an internal field distribution and the muon gyromagnetic ratio is $\gamma_\mu/2\pi = 135.5$ MHz/T. The KT function represents a static field distribution. The static, randomly orientated local field of the nuclear moments of constituent elements are the main origin of the static magnetic field in a superconductor and an additional contribution to the static magnetic field can appear in a superconductor with broken TRS [35]. The depolarisation due to the nuclear moments usually has a Gaussian character. In Eq. 2.6, an exponential term $\exp(-\Lambda t)$ describes an additional relaxation caused probably by some other spin-lattice relaxation process [32, 35]. The exponential form of the signal represents a broad distribution of fields so it can represent magnetic fields due to supercurrents induced around magnetic impurities and domain walls [34]. Relaxation due to the presence of a spontaneous magnetic field developed at T_c can be represented with an increase of either Δ_{KT} or Λ (see Eq. 2.6) with decreasing temperature and the onset of this

behaviour is at the T_c. Temperature-dependent Δ_{KT} have been so far observed in the superconducting states of $LaNiGa_2$ [40], $PrPt_4Ge_{12}$ [35], $PrOs_4Sb_{12}$ (also with doping) [32, 36] and Re_6Zr [39]. Evidence of temperature-dependent Λ was observed in the superconducting states of Sr_2RuO_4 [34] and $LaNiC_2$ [10]. To try to understand the TRS breaking in superconductors, it is beneficial to summarize the known properties of compounds where this behaviour occurs. Information about the crystal structures and critical temperatures of compounds, which break the TRS in their superconducting state, are shown in a Table 2.1.

Compound	Space Group	Crystal Structure	Structure Type	T_c	References
$LaNiC_2$	*Amm2* (NCS)	orthorombic	$CeNiC_2$	2.7 K	[10, 43]
$LaNiGa_2$	*Cmmm*	orthorhombic	$NdNiGa_2$	2.1 K	[40]
$PrPt_4Ge_{12}$	$Im\bar{3}$	cubic	Fe_4LaPt_{12}	7.9 K	[35, 44]
$PrOs_4Sb_{12}$	$Im\bar{3}$	cubic	Fe_4LaPt_{12}	1.85 K	[32, 45]
Sr_2RuO_4	*I4/mmm*	tetragonal	K_2NiF_4	1.5 K	[34, 46]
B phase UPt_3	*P63/mmc*	hexagonal	Ni_3Sn	≈0.5 K	[37, 47]
$(U_{1-x}Th_x)Be_{13}$	$Fm\bar{3}c$	cubic	$NaZn_{13}$	see text	[48, 49]
Re_6Zr	$I\bar{4}3m$ (NCS)	cubic	α-Mn	6.75 K	[39, 50]

Table 2.1: Superconductors with broken time-reversal symmetry.

$LaNiC_2$ crystallizes in a non-centrosymmetric $CeNiC_2$-structure and it becomes superconducting below T_c =2.7 K. No magnetic order was observed in $LaNiC_2$. Hillier *et al.* measured $LaNiC_2$ using μSR and reported the observation of broken TRS in the superconducting state of $LaNiC_2$ [10]. The μSR spectra measured for $LaNiC_2$ is shown on Fig. 2.5(a). A point group analysis for $LaNiC_2$ identified 12 potential gap functions but only 4 of them allows for broken TRS. Those 4 possible representations describe only a nonunitary superconductor with a weak spin-orbit coupling (SOC), which would suggest such characteristics apply to $LaNiC_2$ [10,51]. A conventional superconductor would show an exponential behaviour of the specific heat

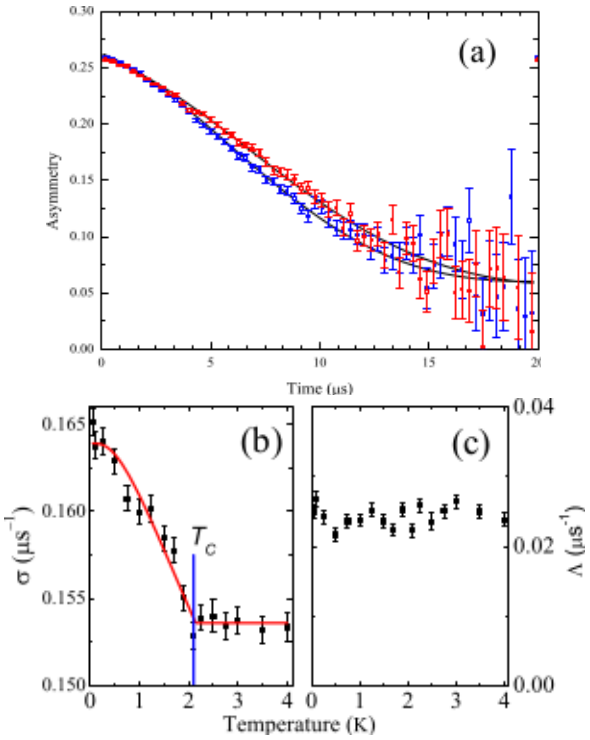

Figure 2.5: (a) Time dependence of a muon asymmetry for $LaNiC_2$, measured in zero applied magnetic field using μSR. A visible difference between the spectra in the superconducting (blue symbols) and normal states (red symbols) gives evidence that a spontaneous magnetic field is present, when $LaNiC_2$ in the superconducting state. Taken from [10]. (b) Temperature dependence of the depolarisation rate σ for $LaNiGa_2$. The T_c of $LaNiGa_2$ is 2.1 K and a transition in σ(T) occurs at the same temperature so a spontaneous magnetic field develops at the superconducting transition. Taken from [40]. (c) Temperature dependence of Δ for $LaNiGa_2$. Δ is an additional electronic relaxation rate. Taken from [40]. See details in text.

temperature dependence, yet for $LaNiC_2$ a power-law behaviour was observed [52]. The appearance of nodes in the superconducting gap function also indicates the unconventional nature of the superconductivity in $LaNiC_2$ [53].

$LaNiGa_2$ is superconducting below $T_c = 2.1$ K. It has a similar chemical composition to $LaNiC_2$ but crystallises in the centrosymmetric $NdNiGa_2$-structure. The ZF-μSR experiments show that a small spontaneous magnetic field appears at the superconducting transition, so the superconducting $LaNiGa_2$ breaks TRS. [40] The ZF-spectra are described well with Eq. 2.7 so the temperature dependence of Δ_{KT} and Λ can be obtained and for $LaNiGa_2$ these are shown in Fig 2.5(b) and (c). A change

of Δ_{KT} was observed at T_c and Δ_{KT} increases with decreasing temperature and the additional depolarisation rate, Λ is temperature independent. For a superconductor with a broken TRS, which belongs to the D_{2h}-point group, the theoretical point group analysis indicates only 4 possible representations and all of them have a weak SOC and are non-unitary, which is similar to the conclusions made for $LaNiC_2$.

In NCS Re_6Zr the enhanced electron-phonon coupling was found using heat capacity measurements. Also evidences of broken TRS were observed and group representation analysis suggests an unconventional pairing mechanism [39].

Sr_2RuO_4 crystallizes in the perovskite-structure and is superconducting below 1.5 K. Luke *et al.* studied Sr_2RuO_4 using μSR technique and reported that a small spontaneous magnetic field appears in zero field and its electronic depolarisation Λ increases with decreasing temperature with an onset at T_c [34]. This indicates that TRS is broken for superconducting state of Sr_2RuO_4. Hence the presence of spin-triplet superconductivity, as well as p-wave symmetry of a superconducting gap function were suggested [34] and experimental evidence for these behaviours was found [54].

TRS breaking was also observed using the ZF-μSR in a heavy fermion filled skutterudite $PrOs_4Sb_{12}$ [32], also when it was doped with Ru: $Pr(Os_{1-x}Ru_x)_4Sb_{12}$ and La: $Pr_{1-y}La_yOs_4Sb_{12}$ [36]. Additionally, an unusual behaviour of the temperature dependence of the upper critical field of $PrOs_4Sb_{12}$ was reported [55] (see Fig. 2.6(a)). The Werthamer-Helfand-Hohenberg (WHH) model [56, 57] usually describes well H_{c2} behaviour of many superconductors but the H_{c2} of $PrOs_4Sb_{12}$ does not agree with WHH model. The H_{c2} of $PrOs_4Sb_{12}$ was found to be described well by a two-fluid model [55, 58]. A similar temperature dependence of H_{c2} was observed in some borocarbides (i.e. see Fig. 2.6(b)) [58] and MgB_2 [59].

In another skutterudite $PrPt_4Ge_{12}$, below its T_c, an increase in Δ_{KT} with decreasing temperature has been observed using μSR, which suggests that TRS is broken in this compound and the order parameter of $PrPt_4Ge_{12}$ has a complex

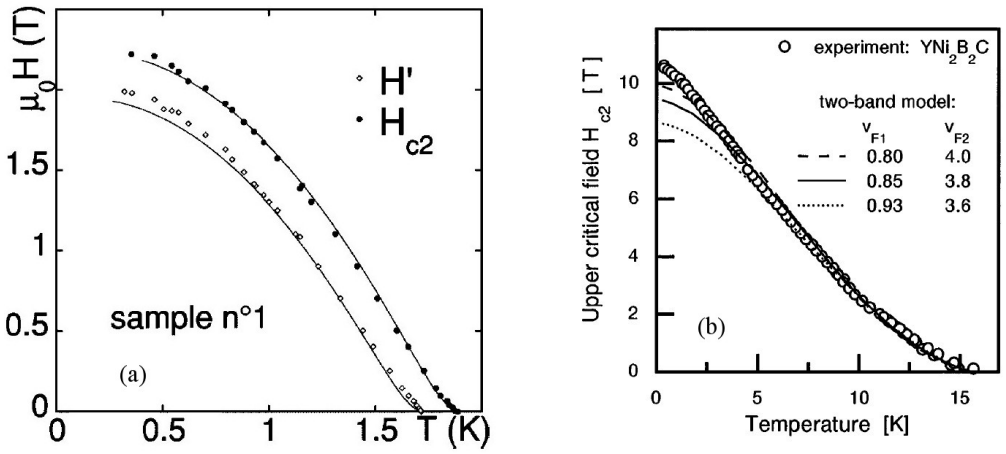

Figure 2.6: (a) Temperature dependence of the upper critical field for $PrOs_4Sb_{12}$ (filled symbols). Data were obtained from a specific heat measurements. The lines represent fits by a two-band model. Taken from [55]. (b) Temperature dependence of H_{c2} for YNi_2B_2C. Data points were determined by resistivity measurements. Fitted curves come from fitting with two-bands model for different Fermi velocities (marked on graph), for details of the fit see [58]. Taken from [58].

waveform. This depolarisation field arises mainly due to the nuclear moments of Pr and Maisuradze *et al.* suggested also that it is additionally hyperfine-enhanced [35]. The presence of the p-wave gap function and spin-triplet pairing was suggested for $PrPt_4Ge_{12}$, but a spin-singlet ground state can exist in $PrPt_4Ge_{12}$ if the Cooper pairs have non-zero orbital moment [35]. Additionally, evidence of point nodes in the superconducting energy gap were found for $PrPt_4Ge_{12}$ [35].

TRS is broken in the skutterudites $PrPt_4Ge_{12}$ and $PrOs_4Sb_{12}$, while a few other skutterudites have been reported to preserve TRS. For $PrRu_4Sb_{12}$ [60] or $ThPt_4Ge_{12}$ [61], no spontaneous field was observed using the ZF-μSR technique. Also no spontaneous field was measured using the ZF-μSR in the NCS $LaRhSi_3$ [62].

Amongst the heavy fermion compounds, the skutterudite $PrOs_4Sb_{12}$, the B phase of UPt_3 and $(U_{1-x}Th_x)Be_{13}$ break TRS. The heavy fermion compound UPt_3 is antiferromagnetically ordered below $T_N = 5$ K and becomes superconducting below $T_c \approx 0.5$ K. In the superconducting state, UPt_3 has a rich H-T diagram, and at least 3 different superconducting phases were identified (see the H-T diagram, for

example: Fig. 8 in [1]). The ZF-μSR spectra give evidence that TRS is broken in the superconducting B phase of UPt_3 [37].

Th-doped UBe_{13} for a low concentrations of Th is superconducting. With increasing concentration of Th, non-monotonic changes in T_c are observed, for details see the phase diagram, e.g. Fig. 11 in [26]. When the Th concentration (x) is approximately in the range from 0.018 to 0.045, the ZF-μSR studies give evidence that a spontaneous magnetic field appears at zero field, hence TRS is broken in the superconducting state of this compounds. $(U_{1-x}Th_x)Be_{13}$ first enters the superconducting state at a temperature T_{c1}, and then the spontaneous field appears at a temperature T_{c2}, well below T_{c1} [26]. For example, for $(U_{1-x}Th_x)Be_{13}$, where x = 0.0355, $T_{c1} = 0.55$ K and $T_{c2} = 0.39$ K [26, 48].

2.2.3 Non-centrosymmetric superconductors

The non-centrosymmetric superconductors (NCS) break not only the gauge symmetry due to electrons pairing, but also the inversion symmetry, so they are potential candidates for unconventional superconductors. So far TRS breaking was observed only in NCS $LaNiC_2$ [10,51] and Re_6Zr [39] but other exotic properties were reported in NCS superconductors. In some NCS compounds, nodes in the superconducting energy gap appear. An s-wave order parameter has rotational symmetry and a gap in the low energy excitation spectra, which causes exponential temperature dependence of the relaxation rate. Non s-wave order parameters have point and line nodes and this will influence various physical properties [26]. Evidence of line nodes in the superconducting energy gap were found in Mo_3Al_2C [63], Y_2C_3 [64] and $Li_2Pd_{3-x}Pt_xB$ [65]. In some cases, multiple superconducting gaps are present, i.e. in Y_2C_3 [66], $Mg_{10}Ir_{19}B_{16}$ [67, 68], La_2C_3 [69].

The $Li_2Pd_{3-x}Pt_xB$ NCS superconductors are also interesting due to a contrast between properties of Pd- and Pt- end members: Li_2PdB is a conventional superconductor and Li_2PtB is a spin-triplet superconductor. Various nodal types

are expected to occur when doping $Li_2Pd_{3-x}Pt_xB$ [65]. Due to a lack of inversion symmetry and the antisymmetric spin-orbit coupling, a mixture of spin-singlet and spin-triplet states can exist in NCS superconductors [41, 65]. In the strongly correlated NCS $CePt_3Si$, a superposition of a spin-singlet and spin-triplet states was suggested [41, 70–72]. In some NCS heavy fermions, the upper critical field exceeds the Pauli limiting field, which is defined as a field which destroys superconductivity due to the Zeeman energy of electrons [2]. The H_{c2} well above the Pauli limit was observed for example in the NCS $CeRhSi_3$ [73] and $CeIrSi_3$ [74]. Non-centrosymmetric UIr shows interesting behaviour under applied pressure. In ambient pressure, it is an itinerant ferromagnet. But under pressure of approximately 2.6 GPa, it becomes superconducting below $T_c = 0.14$ K in a very narrow range of its phase diagram [75].

2.2.4 Other unconventional superconductors

Sections 2.2.3 and 2.2.2 contain detail description of superconducting compounds with NCS structure and with broken TRS in the superconducting state, because these compounds are directly relevant to the work presented in this thesis. Other families of unconventional superconductors are out of the scope of this thesis, so in this section, their behaviour is only briefly outlined. More information about unconventional superconductivity can be found in several review articles and books, for example [1, 26, 76] and review articles given in following sections.

2.2.4.1 Cuprates

Shortly after Bednorz and Müller announced the observation of superconductivity in perovskites, Wu *et al.* reported $YBa_2Cu_3O_{7-y}$ (YBCO) as the first superconductor with T_c above 90 K [4]. This was an important milestone, because this material requires only cooling with liquid nitrogen to be in the superconducting state, rather than liquid helium. To date, the highest T_c among cuprates for a bulk sample was reported in $HgBa_2Ca_2Cu_3O_{8+\delta}$ with $T_c = 135$ K at ambient pressure and $T_c = 164$ K

under a pressure of 30 GPa [77]. Among cuprates, La-(Ba,Sr,Ca)-Cu-O, Br-Sr-Ca-Cu-O and Tl-Ba-Ca-Cu-O are the main families which show superconducting behaviour [77]. Values of the critical temperature and critical fields of cuprates can be changed by elemental substitution, varying the crystal structure, pressure or stoichiometry. Cuprates adopted the perovskite layered-structure with CuO_2 planes, where metallic conductivity appears. This layered structure causes a significant anisotropy of the superconducting properties [77, 78].

The coherence length of cuprates is relatively short but the penetration depth is large so cuprates are high-κ superconductors. The presence of nodes in the superconducting order parameter was reported, which is evidence for a non-s-wave character and a presence of the d-wave order parameter was suggested (see [78] and references therein). New pairing mechanisms in cuprates were considered, but no conclusion can be made with current stage of experimental knowledge [77].

The cuprates behaviour in the normal state is unusual as well. A non-Fermi liquid behaviour was observed for cuprates in the normal state. Also, a pseudogap exists in cuprates above T_c, but its nature is unclear. Some evidence suggests that the pseudogap is a precoursor of the superconducting gap, but they are also indications that a pseudogap might be a state with a long range order [78]. There are more than 100,000 publications concerning theoretical and experimental aspects of superconductivity in the cuprates [77] so only a brief summary has been given here.

2.2.4.2 Molecular superconductors

Theoretically predicted in the late sixties, superconductivity in organic compounds was not experimentally observed till 1979 [78]. In 1979, Jerome *et al.* reported that one of the Bechgard salts $(TMTSF)_2PF_6$ is superconducting under a pressure of 0.5-0.6 GPa, below $T_c = 1$ K [28, 79]. So far the highest T_c of 18 K was discovered in a potassium intercalated picene (K_3*picene*) [79].

The presence of point-nodes was suggested in organic superconductors, although there is also some evidence that their gap is nodeless with s-wave pairing symmetry. A phonon-mediated pairing mechanism might be present in organic superconductors, but it was also proposed that spin or charge fluctuations take part in the formation of the Cooper pairs [79]. The characteristic parameters of organic superconductors (i.e. coherence length, critical fields) are often anisotropic [2,81], additionally H_{c2} of organic superconductors often exceeds the Pauli-limiting field. Evidence of other exotic behaviour was also reported, i.e. existence of the Fulde-Ferrell-Larkin-Ovchinnikov (FFLO) phase was suggested for a few organic superconductors [79].

Doped fullerenes are another fascinating class of molecular superconductors. Figure 2.7 presents a crystal structure of superconducting fullerene. Those spherical carbon materials have a T_c as high as 40-45 K in $Rb_{2.7}Tu_{2.2}C_{60}$ [82] and nearly 50 K in Cs_3C_{60} (T_c = 47.4 K) [2]. Amongst the fullerenes, superconductivity has also been reported in K_3C_{60} with T_c = 16.3 K and Rb_3C_{60} below 30.5 K [2, 28]. Fullerenes are weak to medium coupled superconductors with an electron-phonon coupling constant, $\lambda_{el-ph} = 0.51$ for K_3C_{60}, 0.61 for Rb_3C_{60} and 0.72 for Cs_3C_{60} [2]. More informations about superconductivity in organic compounds can be found for example in books [28, 81] or a recent review paper [79], and references therein. In

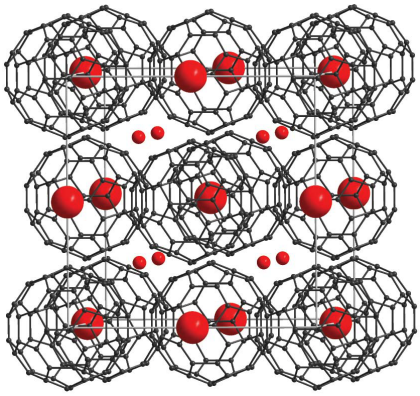

Figure 2.7: A crystal structure of a superconducting fcc (face-centred cubic) Cs_3C_60. Other superconducting intercalated fullerens,A_3C_{60} (where A is an alkali metal) also adopts a similar fcc structure. Taken from [80].

particular, for details about superconductivity in fullerenes see the review article [83].

2.2.4.3 Heavy fermion superconductors

Heavy fermion (HF) compounds contain $4f$ and $5f$ electrons and have a density of states at the Fermi level, 1000 times larger than in copper, so electrons in HF compounds have a high effective mass - a few orders of magnitude larger than in ordinary metals [84, 85]. HF superconductors have a complex electronic structure caused by the presence of multiple f orbitals from $4f$ and $5f$ electrons with localized moments. HF superconductors show strong spin-orbit coupling and a complex Fermi surface, so it is difficult to identify the pairing symmetry for HF superconductors [5]. The presence of point or line nodes was suggested, for example line nodes, a characteristic of an f-wave order parameter, were observed in UPt_3 (see Fig. 2.8) [1]. An extremely high density of states in HF superconductors and a complex Fermi surface cause power law behaviour in its physical properties [86]. Additionally, the Sommerfeld constant for the linear part of the specific heat and the Pauli spin susceptibility $\chi(0)$ are 100 - 1000 times larger compared to the ordinary metal values [26]. In the HF compounds, magnetism and superconductivity can coexist. Quantum critical points (QCP) are often present in the HF systems. Hence it

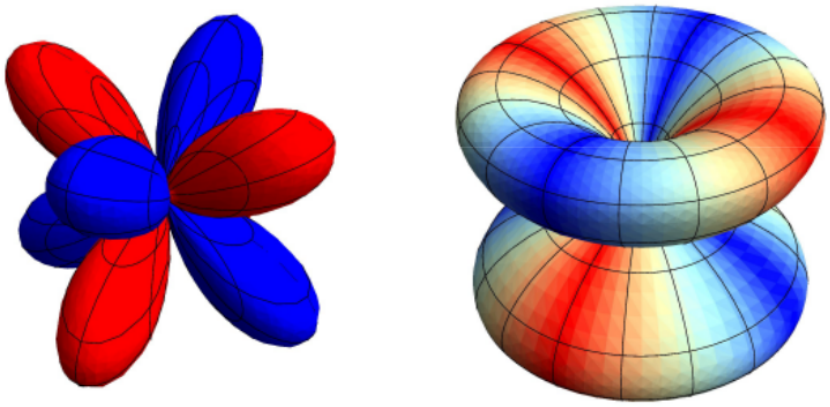

Figure 2.8: An f-wave order parameter from an E_{2u} group representation, suggested for a heavy fermion UPt_3. Taken from [1].

was suggested that magnetic fluctuations participate in the electron pairing (see [84] and references therein). Also other non-primarily BCS, pairing mechanisms were suggested. For example it was proposed that the electron pairing might be mediated by the critical fluctuations due to QCP. More information about the heavy fermion superconductors can be found, for example in a review paper by G.R. Stewart [85], M. Sigrist and K. Ueda [26] or P. Coleman [84] and references therein.

2.2.4.4 Iron-based superconductors

Iron pnictides (iron-based compounds with As or P) and iron chalcogenides (iron-based compounds with S, Sn or Te) are thought to be promising materials for high-temperature superconductors [87]. Other superconductors with Fe were already known before Kamihara *et al.* [88] reported that LaFeAsO is superconducting below 26 K. However, previously known iron-based superconductors had T_cs close to absolute zero and Fe *3d* electrons are not at the Fermi energy in those compounds, unlike in iron pnictides and chalcogenides where Fe *3d* electrons takes part in superconductivity of those compounds [89]. It was proposed that, the magnetic fluctuations have an effect on the pairing mechanism in iron-based superconductors and several electron pairing mechanisms, alternative to BCS coupling, were suggested [90]. The relatively high T_c of LaFeAsO increases under a pressure of 4 GPa to 43 K. Also elemental substitutions may cause an increase of T_c up to 55 K for $SmFeAsO_{0.85}F_{0.15}$ or $SmFeAsO_{0.85}$. Belonging to 6 different families, all iron-based superconductors have a quasi-2D structure with Fe(As,P) or Fe(S,Sn,Te) planes and share other common properties [89]. Iron pnictides and chalcogenides are metals, so have good mechanical properties [87, 89]. For more informations see the recent review papers by Degatto E. [87], Steward G.R. [89] and Johnston D.C. [90] and references therein.

2.3 Summary

The chapter outlines a current stage of the knowledge about superconductors, especially unconventional ones. Both theoretical and experimental milestones were presented. A brief overview of the BCS theory was given and the GL theory was introduced. This thesis reports studies of unconventional superconductors, the chapter focus on the studies undertaken in the area of unconventional superconductivity. Superconductors with broken TRS and NCS superconductors are directly relevant to this study so those 'classes' were presented in detail. State of art in other families of unconventional superconductors, i.e. cuprates, molecular and iron-based superconductors, as well as heavy fermions superconductors, was shown. The background chapter, together with the next chapter, which introduces experimental methods used in this thesis, set the scene of the presented studies.

Chapter 3

Experimental methods

Studies of the flux line lattice in superconductors provide valuable knowledge about the complex phenomena of superconductivity. So far, various experimental techniques have been used to study the flux line lattice (FLL) of superconductors. Spatially varying magnetic fields from the FLL can be investigated by Bitter decorations, nuclear magnetic resonance, small angle neutron diffraction and muon spectroscopy [91].

My research involves two of these techniques: muon spectroscopy (μSR) experiments and small angle neutron scattering (SANS). The μSR technique is a very sensitive probe of the magnetic field so is an excellent probe of the FLL. Additionally, unlike many other experimental techniques, μSR experiments can be carried out without an applied magnetic field. SANS is a direct way to determine the symmetry of the FLL and also provides information about the fundamental parameters of the superconductor. Magnetic and transport measurements were also carried out to acquire additional information about the investigated superconductors. These techniques were applied to polycrystalline materials, which I prepared using the arc furnace, as well as to single crystals.

3.1 Sample preparation and structural characterization

3.1.1 Arc furnace melting

Polycrystalline samples were prepared using the tri-arc furnace (Fig. 3.1). The creation of an electric arc (a plasma of ionized gas) is the principle underlying the arc melting technique. The electric current flows through a tungsten electrode and an electric arc is created between the electrode and a copper hearth (those elements of the furnace are marked in Fig. 3.1).

To prepare a polycrystalline sample, a stoichiometric amount of the constituent elements was placed on a water cooled copper hearth. The melting chamber was evacuated and filled with argon. Melting was performed under an argon atmosphere to ensure there was no air to react with. An electric arc was established and positioned in proximity to the constituent elements. The ionized column of gas applied to the metals heats and melts them. The sample was flipped over and re-melted few times to form a homogeneous sample.

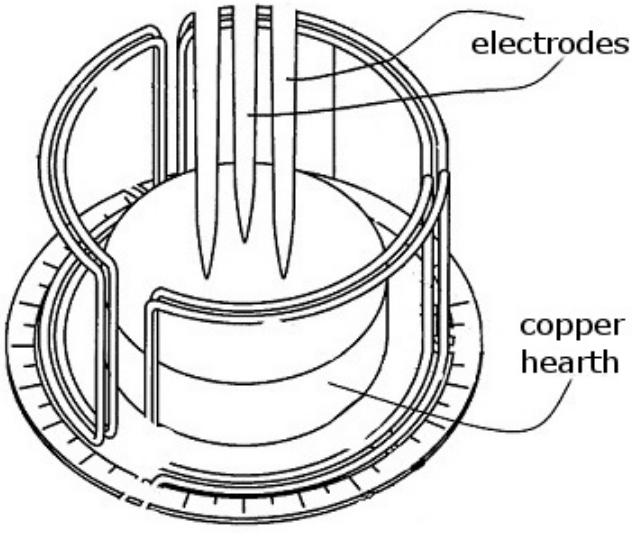

Figure 3.1: Schematic illustration of the tri-arc furnace. Adapted from [92]
.

3.1.2 X-ray diffraction techniques

The periodic arrangement of atoms in solids can be studied using x-ray diffraction. William Bragg presented a mathematical description of diffraction which is nowadays known as Bragg law (Eq. 3.1) [93]. Diffraction from materials occur only when the angle of the incident beam and angle of reflection from the crystal plane θ are related with the wavelength of the incident beam λ by:

$$n\lambda = 2d\sin\theta \tag{3.1}$$

where d is the distance between scattering planes and n is an integer, which indicates the order of reflection [94].

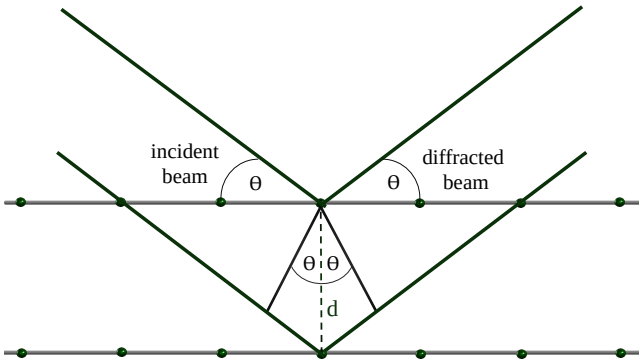

Figure 3.2: Schematic representation of diffraction by parallel crystal planes, as described by Bragg law.

X-ray diffraction experiments provide information about the structure of a material, its defects and phase composition. The diffraction experiments for polycrystalline samples were carried out using high resolution powder diffraction with a Panalytical X-Pert Pro MPD diffractometer. Single crystals were studied using single crystal CCD x-ray diffraction with a Gemini R diffractometer, Oxford Diffraction [95]. For more detail about x-ray diffraction techniques see [94, 96, 97].

3.1.3 Laue diffraction

Real-time Laue imaging system was used to align the single crystal along the desired crystallographic direction before experiments. Our Laue system uses the back-reflection Laue method. A crystal was placed on a triple-axes goniometer on a moveable stage, so precise rotational and translational movements of the crystal were possible. The sample was illuminated with X-ray (W) radiation and backscattered X-rays were detected by a charged-coupled device (CCD) sensor. Laue diffraction patterns were collected and the desired crystal orientation was identified with the assistance of the OrientExpress software [98]. For more details about Laue diffraction technique, see [94].

3.2 Magnetic measurements

The magnetic measurements were carried out using the Quantum Design's Magnetic Property Measurement System (MPMS) with SQUID (Superconducting Quantum Interference Device). MPMS is a very sensitive probe of magnetic moment. The MPMS has a resolution of $5 * 10^{-8}$ emu [99, 100]. In the MPMS a sample moves through the pick-up coils of a second order gradientmeter and a magnetic field is applied perpendicular to the plane of the coils. The gradientmeter rejects any uniform magnetic field and the change of the flux is measured by the SQUID (Fig. 3.3) [101]. SQUID is a superconducting coil with two Josephson junctions. Tunnelling of Cooper pairs through the insulating layer of a Josephson junction is possible, so a small current passes thorough the superconducting loop and when the magnetic field changes, a phase difference between the junctions biases appears.

Magnetic properties can be examined using DC or AC measurements. DC measurements provide information about the temperature dependence of the magnetic moment (magnetization (M) versus temperature (T) measurements in a constant magnetic field (H)), or can be used to investigate the sample response for various

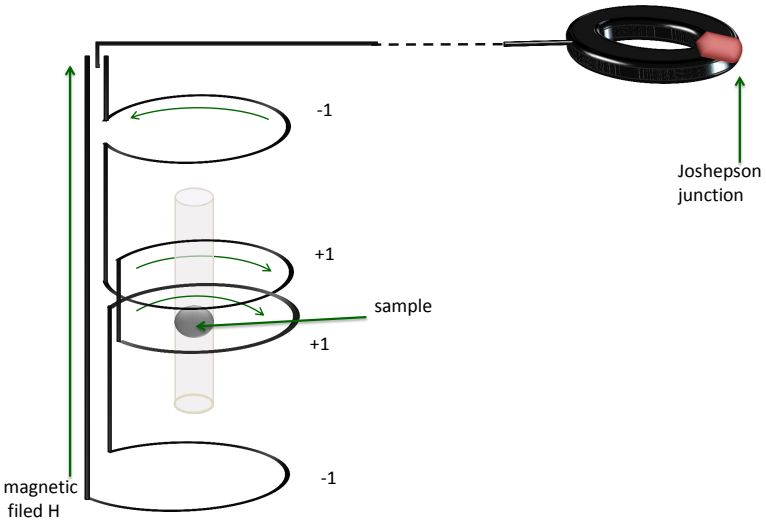

Figure 3.3: Schematic illustration of MPMS. Second-order gradiometer with SQUID is shown.

magnetic fields (M versus H measurements, when temperature is kept constant). Using AC measurements, the magnetization dynamics of the sample can be studied [102]. Magnetic measurements were carried out using DC measurements, in either a zero field cooled (ZFC) conditions or field cooled (FC) conditions . In the ZFC conditions, the sample was cooled to the base temperature in zero field. Afterwards a magnetic field was applied and measurements were carried out during warming. In the FC conditions, the sample response was measured during cooling in an applied magnetic field. In MPMS, the magnetic moment (m) is measured in absolute units emu. Afterwards, (volume) magnetic susceptibility (χ) can be calculated:

$$\chi = \frac{m}{VH} \tag{3.2}$$

where H is the applied magnetic field and V is the volume of a sample.

Magnetic response of the sample in an applied magnetic field depends on the shape of the sample because of the demagnetization effects. A demagnetization

correction has to be included to find the absolute value of measured susceptibility (χ) [2]:

$$\chi = \chi_{exp}(1 - N) \tag{3.3}$$

where χ_{exp} is the measured value of magnetic susceptibility and N is the demagnetization factor (for example N = 1/3 for a sphere [2]). The formulas describing demagnetization factors for various shapes of the sample can be found in literature, e.g. [2].

With our MPMS system, measurements in magnetic fields up to 7 T can be performed. In a standard MPMS chamber measurements can be carried out in the temperature range from 1.8 K to 400 K. Additionally, with Quantum Design's *iHelium3* system, measurements can be performed down to 0.5 K [103].

3.3 Transport measurements

The transport measurements were carried out by the four probe technique using a Quantum Design's Physical Property Measurement System (PPMS). Using this PPMS, measurements can be carried out in the temperature range from 1.8 to 300 K and in magnetic fields up to 9 T. For the measurements using the four probe technique, four thin, silver wires were attached with silver paint to a rectangular bar-shape sample, schematically shown in Fig. 3.4. The two outer wires pass current through the sample and the other two wires measure a voltage drop across the sample. The values of the applied current and the voltage drop are used to find a resistance (R) using Ohm's law. A further calculation gives resistivity (ρ) of measured material (Eq. 3.4):

$$R = \rho \frac{l}{A} \tag{3.4}$$

where l is the distance between voltage leads and A is the cross - section area.

The advantage of the four probe technique is that it enhances the accuracy

of the measurements. Separate current and voltage leads eliminate error due to the resistance of contact, because the voltage leads draw barely any current [104]. Measurements of resistance can be carried out in DC or AC transport modes. DC transport measurement mode supplies a maximum current of 5 mA. AC transport measurements use an AC bias current from 1 Hz to 1 kHz and a maximum current of 110 mA. In AC mode, signal filtering can be implemented so that the sample signal can be isolated. Hence measurements carried out using AC transport have greater sensitivity than DC transport measurements [104].

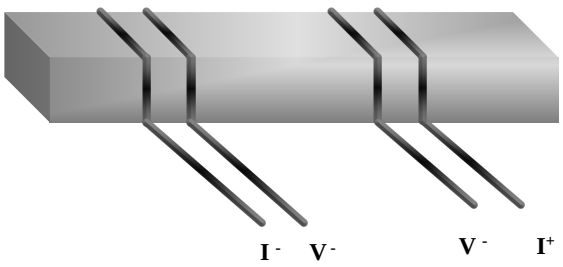

Figure 3.4: Schematic illustration of a sample with the wires for the four - wire resistivity measurements. Concept adapted from [104].

3.4 Muon spectroscopy

Muon spectroscopy (μSR) is a powerful technique in the field of condensed matter physics [8]. Muons carry a magnetic moment, so they are a very sensitive probe of the local magnetic field [105–109]. Muons are charged particles (μ^+ or μ^-) with spin $\frac{1}{2}$ and magnetic moment. Muon lifetime τ_μ is only 2.2 μs and μ^+ decays to a positron (e^+) and neutrino–antineutrino pair:

$$\mu^+ \quad \longrightarrow \quad e^+ + \nu_e + \overline{\nu_\mu} \tag{3.5}$$

Muon spin rotation and relaxation experiments were carried out using the MuSR instrument in ISIS facility, Rutherford Appleton Laboratory, United Kingdom. In the ISIS pulse source, accelerated protons (p) are fired into a carbon target and pions (π^+) are produced (Eq. 3.6). The pions shortly decay (Eq. 3.7), and a bunch of 100 % spin-polarised surface muons (μ^+) is produced every 20 ms, with a 40 ms break every 5^{th} pulse (one pulse in 5 goes to the ISIS second target station). Those muons have relatively low energies, hence they stop in the material.

$$p + p \longrightarrow \pi^+ + p + n \tag{3.6}$$

$$\pi^+ \longrightarrow \mu^+ + \nu_\mu \tag{3.7}$$

Muons implanted in the material interact with the local magnetic field, then they decay and positrons are emitted preferentially in the directions of the muons spin at the time of their decay. To explore how muon spin polarization changes with time, the positrons from muon decay are counted.

The μSR measurements were carried out either in the field-cooled (FC) conditions or in zero-field (ZF). In the FC condition the sample was cooled in an applied magnetic field from the normal state to mK temperatures, and then the measurements were carried out during warming. For measurements in ZF, the sample was cooled in zero field to the base temperature and then measurements were performed in zero field. Measurements were performed in two geometries: transverse field (TF) and longitudinal field (LF). Description of each mode can be found below. For the μSR experiment, the sample was mounted with GE varnish on a silver plate and covered with a silver foil. Silver gives a time independent signal in longitudinal field geometry and has a negligible nuclear moment which is important when measurements are carried out in TF mode. The sample was inserted into a dilution fridge, which cools the sample down to 40 mK [110]. Figure 3.5 shows different samples used for μSR experiments.

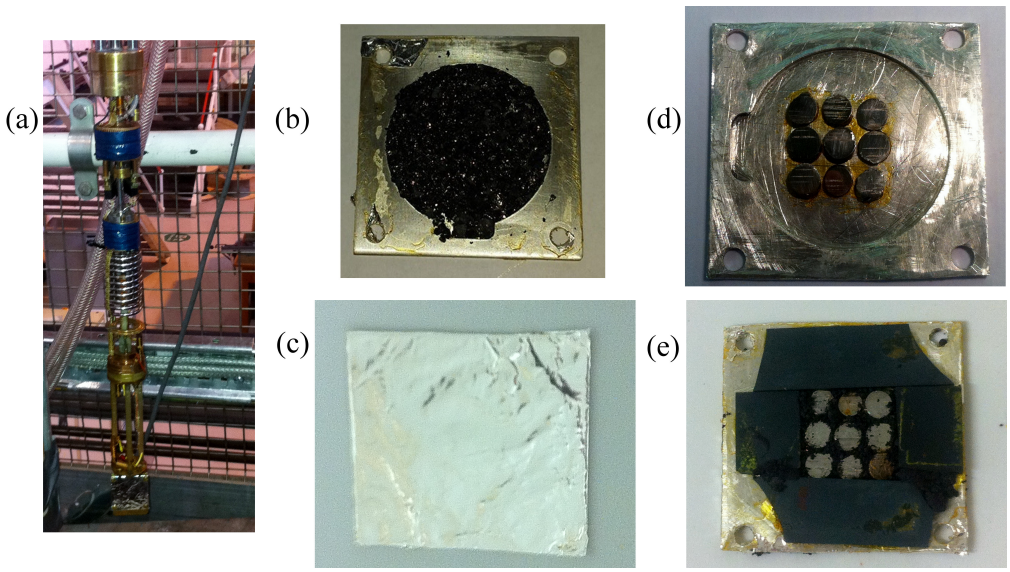

Figure 3.5: Samples for μSR measurements: (a) Sample mounted on the stick, ready to be loaded into the dilution fridge; (b) Polycrystalline sample with GE varnish on a silver holder; (c) Sample on holder, covered with silver foil; (d) Slices of a single crystal mounted on a silver holder, each slice has the same crystallographic orientation; (e) Slices of single crystal surrounded by hematite to reduce the background contribution in TF measurements.

3.4.1 Longitudinal Field Mode

Muon spin relaxation experiments were performed in longitudinal field geometry, so the magnetic field was applied along the original muon beam polarization (see Fig. 3.6). Implanted muons interacted with the local magnetic field and the time evolution of the muon decay was examined using the positrons from muon decay. The positrons were detected by two sets of positron detectors (Fig. 3.6), and represented by an asymmetry function ($A(t)$). The asymmetry $A(t)$ between signals measured by backward and forward detectors corresponds to the time evolution of muon spin polarization (Eq. 3.8). The function A(t) contains information about the spatial distribution, and dynamic fluctuations of the magnetic field in the muon's neighbourhood.

$$A(t) = \frac{N_A(t) - \alpha N_B(t)}{N_A(t) + \alpha N_B(t)} \tag{3.8}$$

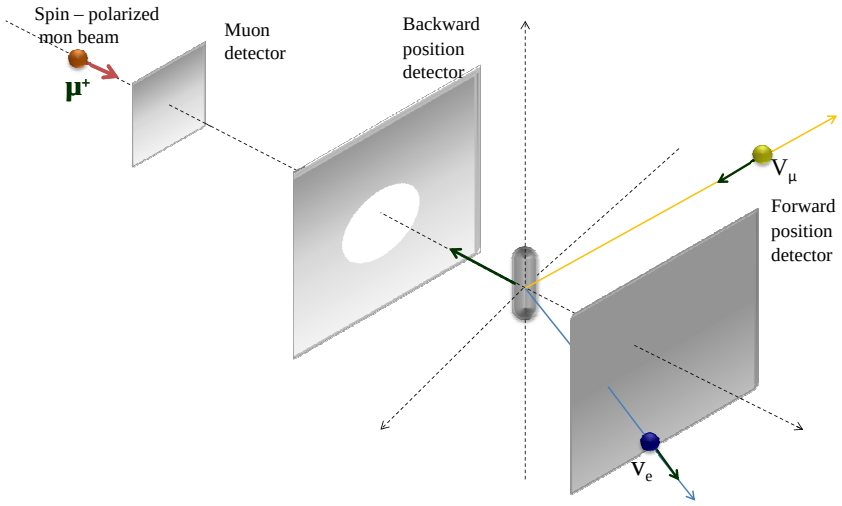

Figure 3.6: Schematic illustration of muon spin relaxation experiment. The muon beam passes through the sample and positrons are detected by a set of detectors, grouped as two virtual detectors: backward and forward detectors. The magnetic field is applied parallel to the direction of the muon beam.

where $N_A(t)$ and $N_B(t)$ represent positrons detected at time t in the forward and backward detector, respectively and:

$$N_{A,B}(t) = N_0 \exp\frac{-t}{\tau_\mu}[1 \pm a_0 P_z(t)] \tag{3.9}$$

and P_z - positron counts. Parameter α introduces a correction for the sample position and the detector efficiency, so α is different for each experiment. α is determined using spectra measured for the sample in a small transverse magnetic field (H = 20 0e) [111].

LF-μSR spectra are described well using the function (Eq. 3.10) with Kubo–Toyabe depolarisation [8]:

$$G_z(t) = A_0 G_z^{KT}(t) \exp(-\Lambda t) + A_{bcg} \tag{3.10}$$

where A_0 is the initial asymmetry of the muon polarisation, Λ is the electronic relaxation rate, A_{bcg} is the background contribution and a function G_z^{KT} is the Kubo-Toyabe function [42]:

$$G_z^{KT}(t) = \left[\frac{1}{3} + \frac{2}{3}(1 - \Delta_{KT}^2 t^2)\exp\left(-\frac{\Delta_{KT}^2 t^2}{2}\right)\right] \tag{3.11}$$

where Δ_{KT}/γ_μ is the width of the internal field distribution and the muon gyromagnetic ratio $\gamma_\mu/2\pi = 135.5$ MHz/T.

3.4.1.1 Zero Field Mode

Unlike many experimental techniques, μSR do not require a magnetic field to be applied to perform the measurements, so experiments can be performed in zero field. The zero field μSR experiment is a special case of LF-μSR, where the sample is measured in zero field. An active field compensation system was implemented to ensure that no magnetic field is present in the ZF-μSR mode.

3.4.2 Transverse Field Mode

Muon spin rotation experiments were carried out in the transverse field geometry, so with the magnetic field applied perpendicular to the muon beam polarization (Fig. 3.7). Implanted muons precess in the magnetic field and then decay to positrons which are detected by 64 scintillator detectors. The detectors are then grouped using software and spectra for two orthogonal, virtual detectors are obtained.

Muons implanted into a superconductor in the mixed state interact with a range of magnetic fields because the magnetic field from the FLL is not homogeneous, and is stronger close to the vortex core. Muons precess in the spatially-varying magnetic field and that causes continuous dephasing of the detected asymmetry signal [8]. Time evolution of the asymmetry of the muon polarisation for FLL is described well by a function consisting of a sinusoidal oscillation with a Gaussian

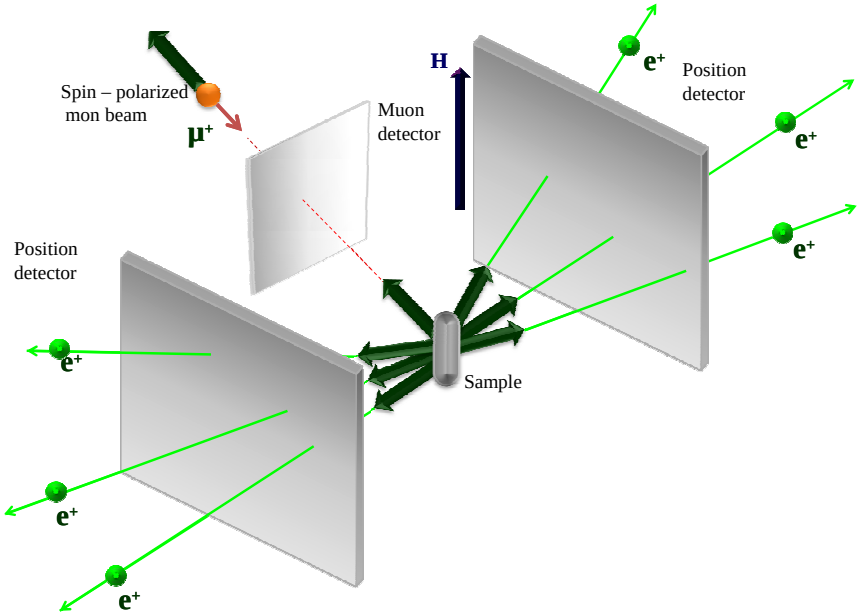

Figure 3.7: Schematic illustration of muon spin rotation experiment. The muons stop in the sample and decay to positrons, which are detected by a set of detectors. A magnetic field is applied perpendicular to the direction of the muon beam.

relaxation (Eq. 3.12):

$$G_x(t) = \sum_{i=1}^{2} A_i \exp\left(-\frac{\sigma_i^2 t^2}{2}\right) \cos\left(\omega_i t + \varphi\right) \tag{3.12}$$

where A is the initial asymmetry, σ is the muon depolarisation rate, φ is the phase offset of the two virtual detectors, ω is the frequency of the muon spin precession, which is related to the induced magnetic field B and $\omega = \gamma_\mu B$. Equation 3.12 includes two terms (marked with index i), a contribution from the superconducting state and the background term. The silver plate contributes most to the background signal. No relaxation in the background term of Eq. 3.12 is expected because silver has a low nuclear moment, so in Eq. 3.12, the value of σ_2 is usually fixed as 0.

The muon depolarisation rate σ includes a superconducting σ_{sc} and nuclear

contribution σ_n and

$$\sigma^2 = \sigma_{sc}^2 + \sigma_n^2 \tag{3.13}$$

σ_n represents the contribution from nuclear moments, so was constant for our measurements and was determined from measurements above T_c. The superconducting part of muon depolarisation rate σ_{sc} is proportional to the magnetic penetration depth λ and hence to the superfluid density so σ_{sc} provides information about the fundamental parameters of a superconductor.

For superconductors with a hexagonal FLL, described well by the London model, the relation between σ_{sc} and λ can be written as [112]:

$$\frac{2\sigma_{sc}^2(T)}{\gamma_\mu^2} = 0.00371\frac{\phi_0^2}{\lambda^4(T)} \tag{3.14}$$

where $\phi_0 = 2.068 * 10^{-15}$ Wb is the magnetic flux quantum and $\gamma_\mu/2\pi = 135.5$ MHz/T.

.

To determine λ for superconductors with relatively low H_{c2}, the effect of overlapping of vortices by their cores needs to be included [113]. Hence the relation between muon depolarisation rate, σ_{sc} (in μs) and penetration depth, λ (in nm) is [114]:

$$\sigma_{sc} = A(1-b)(1+1.21(1-\sqrt{b})^3)\lambda^{-2} \tag{3.15}$$

where b is the reduced field (b= B/ B_{c2}). Parameter A depends on a symmetry of the FLL, for a hexagonal FLL is $A = 4.83 * 10^4$ and $A = 5.07 * 10^4$ for a square vortex lattice.

3.4.3 Simulated μSR spectra of the FLL in superconductors

The magnetic field distribution of the FLL in a superconductor exhibits three types of van Hove singularities: the maxima, which are associated with the core

field, the minima, which corresponds to centres of lattice (midpoint between 3 neighbour vortices) and saddle points (midpoint between 2 vortices) (see Fig. 3.8). A measurement of the ideal FLL would give a spectra with well-defined singularities. An FLL in a real superconductor is subjected to various distortions, hence the singularities will be broadened [91, 115].

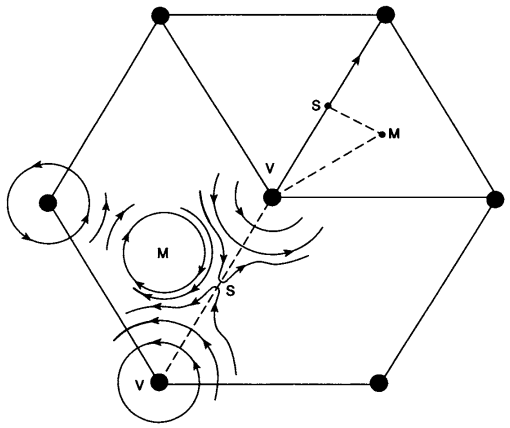

Figure 3.8: Schematic illustration of the FLL in superconductor. Lines of the superconducting current are shown. Vortices (V), minima (M) of internal field and saddle points (S) were marked. Taken from [2].

The theoretical analysis of muon response for spatial varying magnetic field in the mixed state of a superconductor was described by Brandt, e.g. [91, 116] and Sidorenko *et al.* [115, 117]. They simulated the distribution function of a magnetic field n(B). Their calculations take into account how changes of the experimental conditions (i.e. temperature, magnetic field) influence the FLL. Distortions of the FLL were also considered [91]. The polarisation of the muon spin P(t), acquired in the μSR experiment, is related to its Fourier transform P(ω) and the normalized Fourier transform $\widetilde{P}(\omega)$ is proportional to n(B) [91]. The positions of van Hove singularities can be identified in the n(B) distribution and values of the magnetic penetration depth λ can be calculated (See Eq. 3.16,-3.19) [117].

For square FLL:

$$\omega_{min}^{\square} =< \omega > -\frac{\gamma_\mu \Phi_0}{4\pi\lambda^2} \ln 2 \tag{3.16}$$

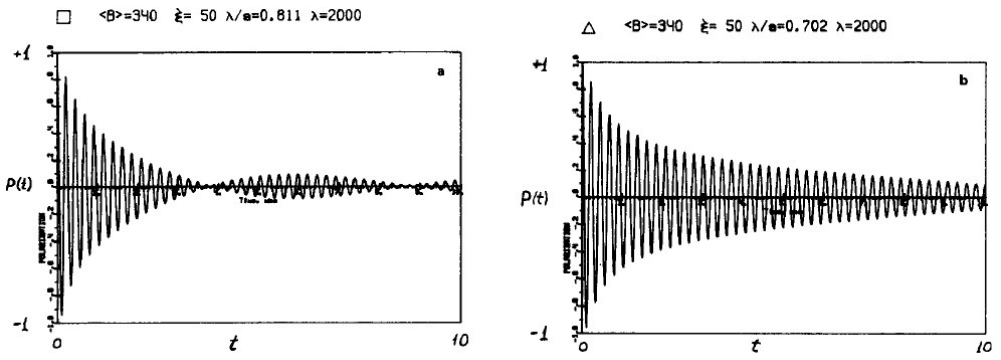

Figure 3.9: Time dependence of muon polarization for a superconductor with (a) square lattice and (b) hexagonal lattice. Taken from [117].

$$\omega_{sad}^{\square} =< \omega > -\frac{1}{2}\frac{\gamma_\mu \Phi_0}{4\pi\lambda^2}\ln 2 \tag{3.17}$$

For hexagonal FLL:

$$\omega_{min}^{\triangle} =< \omega > -0.79\frac{1}{2}\frac{\gamma_\mu \Phi_0}{4\pi\lambda^2}\ln 2 \tag{3.18}$$

$$\omega_{sad}^{\triangle} =< \omega > -\frac{2}{3}\frac{\gamma_\mu \Phi_0}{4\pi\lambda^2}\ln 2 \tag{3.19}$$

Equations have been taken from [117] and $< \omega >= \gamma_\mu B$.

Sidorenko [115] proposed that a beating in the muon asymmetry spectra is characteristic for muons interacting with the magnetic field of a square FLL (see Fig. 3.9 (a)). When a hexagonal lattice is present, such beating will occur at higher times and would be hard to detect with μSR. Additionally, in a hexagonal lattice the ratio of $P_{min} : P_{sad}$ is much lower than the ratio in a square lattice [115] (see Fig. 3.11). For anisotropic superconductors, $P(\omega)$ shows distinct behaviour if the direction of an applied magnetic field deviates from the principal direction of a single crystal. There are two singularities in $P(\omega)$, due to two saddle points in the FLL and the distance between them increases with increas of the deviation from the principal direction of the crystal [117] (see Fig. 3.10). More information about muon study of

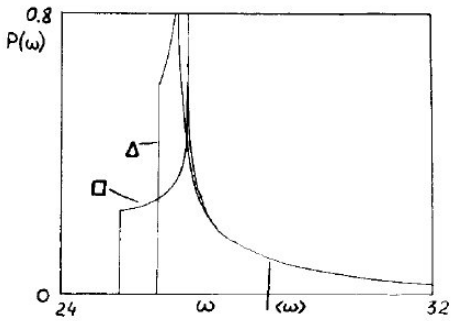

Figure 3.10: Simulated Fourier-transform $\widetilde{P}(\omega)$ of a muon spectra from the FLL of an isotropic superconductor with a $\lambda = 2000$ Å and a magnetic field B = 340 G. The 'square' symbol indicates normalized spectra $\left(\int P(\omega)\mathrm{d}\omega = 1\right)$ for a square FLL and the 'triangle' symbol indicates spectra for a hexagonal FLL. Taken from [117].

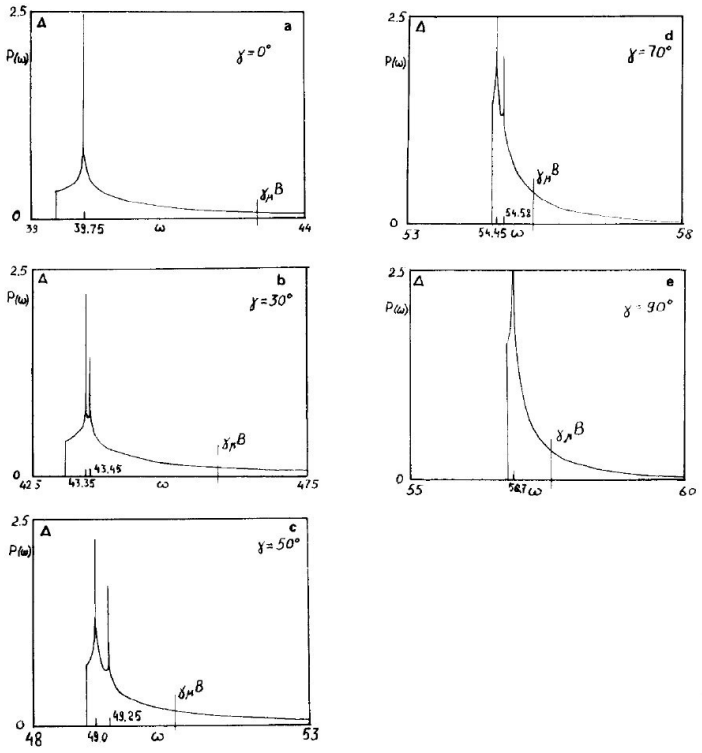

Figure 3.11: Simulated Fourier-transforms $P(\omega)$ for a muon spectra of an anisotropic superconductor with a hexagonal FLL, $\lambda_{ab} = 1450$ Å and $\lambda_c = 7000$ Å. $P(\omega)$ was simulated for magnetic field applied perpendicular to the c-axis of single crystal (Fig.(a)) and for sample rotated away from c axis. The direction of magnetic field remained unchanged (Fig.(b)-(e)). The parameter γ is an angle of rotation away from the principal direction direction of the single crystal. Taken from [115].

the FLL can be found in [91, 115–117] and references therein.

3.5 Small Angle Neutron Scattering

Neutron scattering techniques have found many applications in condensed matter physics [6, 118]. Neutrons interact with nuclei via short range nuclear forces, neutrons also interact by dipole–dipole interactions between the magnetic moments. The later is the fundamental principle behind the FLL measurements. Neutrons very weakly interact with matter so they can penetrate deep in the material and bulk samples can be measured [7].

Small angle neutron scattering (SANS) is a diffraction technique designed to measure relatively large structures. Diffraction of a large structure requires a small scattering angle, and suitable wavelength to satisfy the diffraction condition given by Bragg's law (Eq. 3.1). SANS measurements were carried out using the D22 and D33 instruments in the Institut Laue–Langevin (ILL), Grenoble, France. In the ILL, a high-flux nuclear reactor produces a continuous neutron flux with intensity of $1.5 * 10^{15}$ neutrons per second per cm^2 and a thermal power of 58.3 MW [119].

A schematic illustration of the D22 instrument is shown in Fig. 3.12. The nuclear reactor produces a nearly-continuous neutron spectrum and a velocity selector selects a monochromatic neutron beam, in D22 a wavelength in the range 4.5 Å to 40 Å is used. Divergence, intensity and the size of the beam are adjusted by choosing appropriate collimation settings. In D22, various apertures are available and a collimation length up to 17.6 m can be set. The neutron beam is diffracted by the sample and the signal is detected using a position-sensitive area detector. D22 has a large dynamic Q-range. A momentum transfer Q, can be described as [121]:

$$Q = \frac{4\pi}{\lambda} \sin\theta \tag{3.20}$$

More details about D22 instrument can be found in the D22 manual [121].

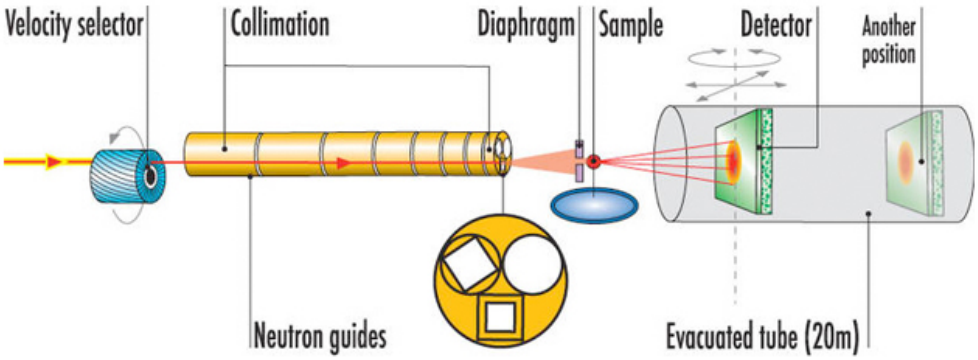

Figure 3.12: Schematic illustration of the D22 instrument, ILL. Taken from [120].

Recently developed D33 instrument (Fig. 3.13) belongs to the next generation of small-angle instruments in ILL. Measurements in a monochromatic mode, as well as experiments in a time of flight mode, can be carried out using D33. More details about D33 instrument can be found in [122].

The magnetic field penetrates type II superconductors in a mixed state in form of vortices and due to the nature of interactions between them, they form a periodic FLL (see Section 2.1). To study the FLL in a superconductor, the sample in the cryostat was placed between the pole pieces of a magnet and experiments can be performed in a temperature range of 1.5 K – 300 K and in a magnetic field (range of available magnetic fields depends on type of magnet, which was used for a particular experiment). The sample and magnet together are placed on the platform and this platform can be rotated relative to the plane of the neutron beam and detector. The rotation can be performed in two planes about phi (vertical rotation) and san

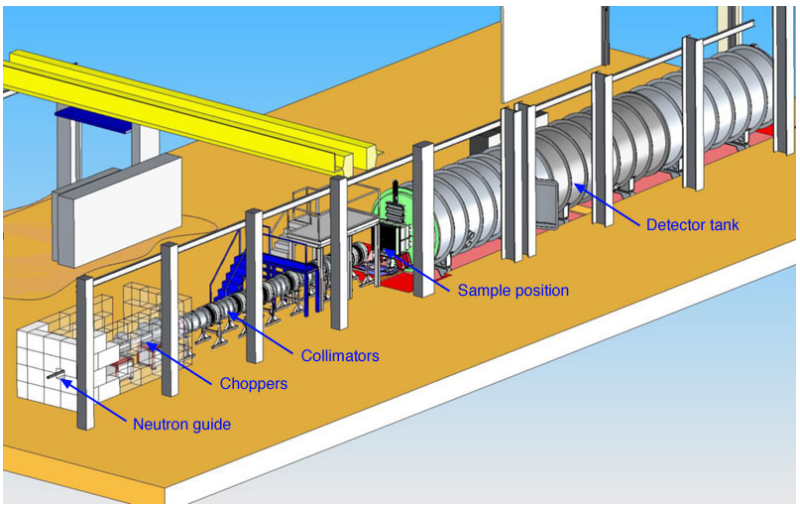

Figure 3.13: Schematic illustration of D33 instrument in ILL. Taken from [123].

angle (horizontal rotation), the angles are marked on Fig. 3.14. In order to perform SANS experiment, the desired orientation of a sample should be placed parallel to the beam direction. Also, the horizontal and the vertical positions of the sample and the magnet need to be adjusted for the centre of the sample to be illuminated by the neutron beam.

To obtain a diffraction pattern from a periodic FLL the Bragg conditions need to be fulfilled. SANS data can be treated as straight-through image when the sample is parallel to the beam, or refinement of the san or phi angles might be necessary to fulfil the Bragg diffraction condition for a particular spot of the FLL pattern.

The main concern when performing a SANS experiment is to fulfil the Bragg's conditions, but also the balance between the desire for high intensity and appropriate q-positions needs to be kept. The neutron flux from the reactor is higher for short wavelengths (Fig. 3.15), and shorter wavelengths also mean a higher energy of neutrons [6]:

$$E = \frac{h^2}{2m_n\lambda_{wvl}} \tag{3.21}$$

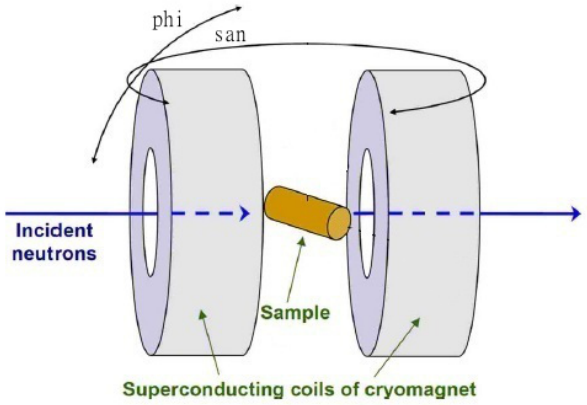

Figure 3.14: Schematic illustration of the geometry of the SANS instrument. Available angles of rotation, san (horizontal rotation angle) and phi (vertical rotation angle) are marked. Adapted from [124].

However, the shorter the wavelength, the higher the q, so θ is higher as well (Eq. 3.20), which might make difficult to detect Bragg spots from the FLL . The available Q-space on the detector also puts some constrains on the detection of the diffracted neutrons. This effect can be reduced by changing the sample – detector distance, so that neutrons from wide-range of scattering angles can be detected. It also needs to be taken into consideration that the non-diffracted, transmitted neutron beam gives strong signal at low-q positions. The wide range of available wavelengths and adjustable collimation and detector length in the SANS diffractometers, D22 and D33, creates a flexible experimental environment, perfect to achieve the main objective of a diffraction experiment, which is to produce a high quality reciprocal image.

SANS is a direct way to study a morphology of the FLL. Symmetry of the FLL can be determined using SANS experiments and values of the fundamental parameters of a superconductor can be acquired. To perform a quantitative evaluation of the SANS data, subtraction of a spectra taken above the superconducting transition is performed to eliminate background contributions, and also correction for the transmission of the direct beam is implemented.

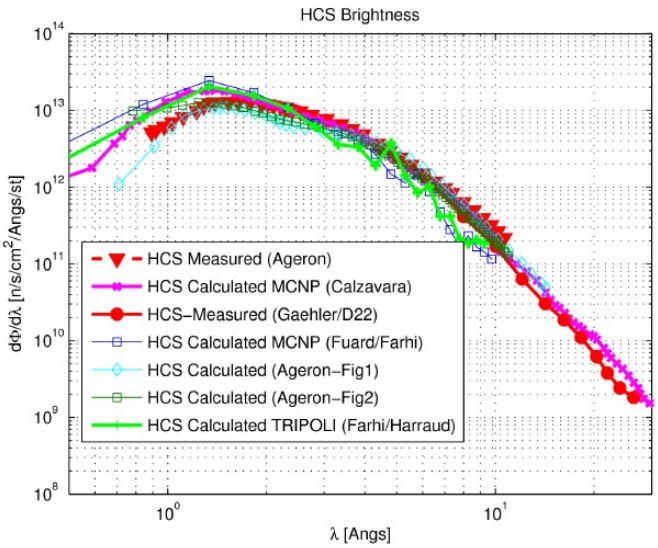

Figure 3.15: Brightness of the neutron guide tube of the ILL reactor, which leading to D22. Taken from [125]. More information about the neutrons produced in ILL can be found in [125].

A software $GRAS_{ans}P$ was used to study data measured using the D22 and D33 instruments. $GRAS_{ans}P$ is a Matlab®-based program designed for the analysis of the data acquired using SANS experiment, which was developed by Charles D. Dewhurst, instrumental scientist in the D33, ILL [126].

3.5.1 The FLL reorientation studied using SANS experiments

Cubitt *et al.* [127] studied MgB_2 using SANS. In MgB_2, in the low magnetic fields a hexagonal FLL exist. In higher magnetic fields, the FLL splits into two hexagonal domains. Further increase of the magnetic field causes a gradual reorientation of the FLL and eventually, a single domain is present again (see Fig. 3.16). It was suggested that the co-existence of σ and π bands at the Fermi surface causes such behaviour [127].

In $CeCoIn_5$, the arrangment of vortices changes with magnetic field and temperature (see superconducting phase diagram in Fig. 3.17) [128]. Two hexagonal

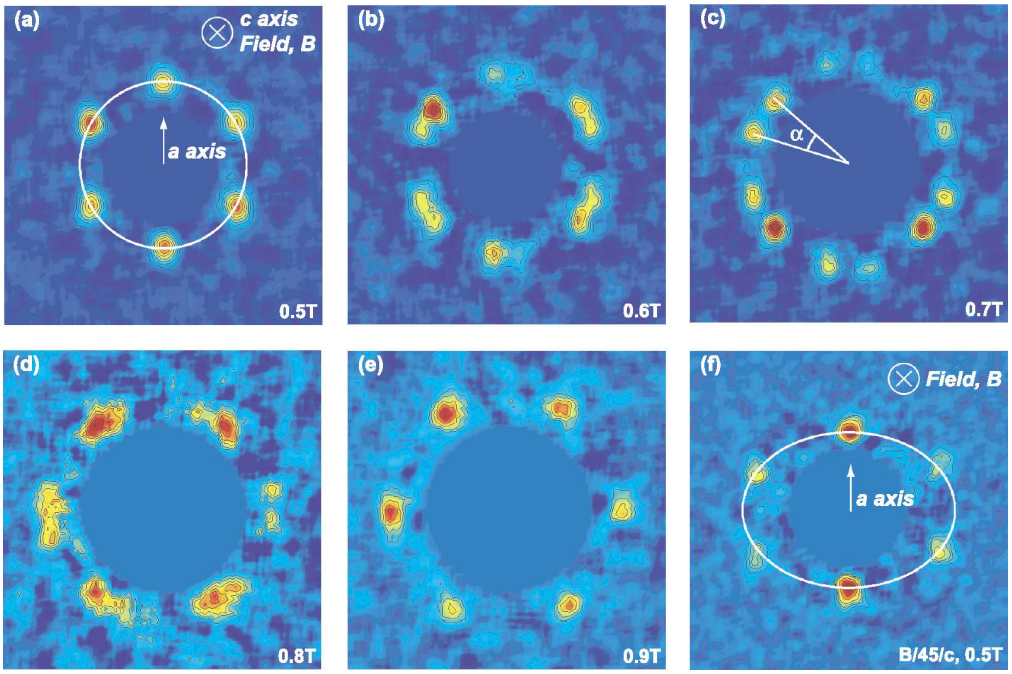

Figure 3.16: SANS diffraction patterns for the FLL of MgB_2 at 2 K. Several frames were summed to satisfy Bragg conditions. Fig. (a) – (e) correspond to the applied magnetic fields of 0.5 T, 0.6 T, 0.7 T, 0.8 T, respectively. The neutron beam and the applied magnetic field were parallel to the c axis of MgB_2 crystal. Fig. (f) presents the FLL of MgB_2 for the sample rotated 45° away from the c axis. The ellipsoidal shape of the pattern is evidence of vortex lattice anisotropy. Taken from [127].

FLL domains exist in low magnetic fields and low temperatures (H = 0.5 T) and with increasing magnetic field the FLL reorientates to either a square or a rhombic lattice. The FLL is again hexagonal in high magnetic fields. In the vicinity of H_{c2}, the Fulde–Ferrell–Larkin–Ovchinnikov (FFLO) state exists in $CeCoIn_5$ (not shown on this phase diagram) [128, 129].

Cooper pairs in the FFLO state have a spatial varying order parameter. It is possible, when the applied magnetic fields are high enough to compete with the internal energy of a material, so the orbital pair breaking effect might be suppressed and Zeeman effect become dominant. Then the electron pairs with non-zero momentum can form, which in real space is realized by the coexistence of normal and superconducting states.

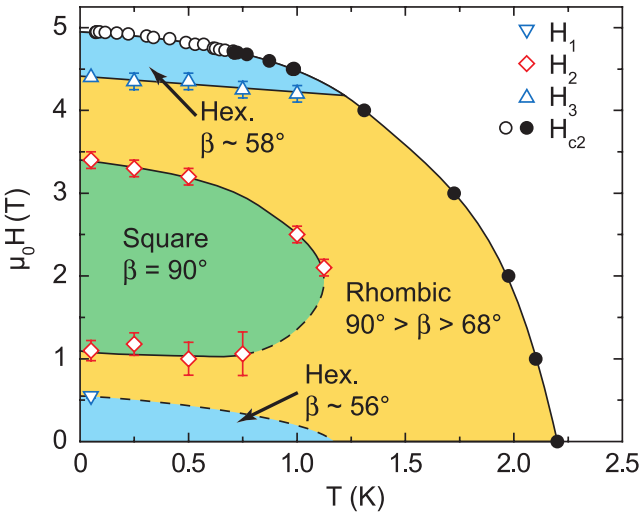

Figure 3.17: Superconducting phase diagram of $CeCoIn_5$ with a magnetic field parallel to the c axis of the single crystal. The experimental data measured using SANS are marked by hollow symbols. Dashed lines indicate the best estimates. The values of H_{c2} were determined by other experimental techniques (marked by circles). Taken from [128]

3.6 Summary

Experimental techniques used in this thesis to study superconductors were presented. Sample preparation with arc melting was outlined. Principles of the x-ray diffraction, magnetic and transport measurements were presented. In this study, μSR and SANS diffraction technique were the main methods used to investigate the FLL in superconductors, hence those are described in more detail. A few examples of studies of the FLL in superconductors using μSR and SANS were also presented.

Chapter 4

Studies of the non-centrosymmetric unconventional superconductor Ru_7B_3

4.1 Chapter outline

Properties of non-centrosymmetric Ru_7B_3 were studied using polycrystalline and single crystal samples. Non-centrosymmetric compounds attract attention as good candidates for unconventional superconductors [41] (see Section 2.2.3). Ru_7B_3 has a Th_7Fe_3-structure (see Section 4.3.1) and binary 7:3 compounds with Th_7Fe_3-structure are well-known for their extraordinary properties (see Section 4.2).

Our muon spectroscopy measurements performed using polycrystalline sample suggest time-reversal symmetry breaking in superconducting Ru_7B_3 (see Section 4.3.3). Additionally, the muon spectra, shows evidence of either square vortex lattice or presence of the anisotropy of the FLL (see Section 4.3.4). To verify these assumptions μSR experiments were performed on a single crystal of Ru_7B_3 (see Sec-

tion 4.4.4.1 and 4.4.4.2). Also, another crystal was grown, using enriched ^{11}B as a starting material to reduce neutron absorption. SANS experiments were carried out because SANS is a more direct way to study the symmetry of the FLL (see Section 4.4.5). Additionally, magnetic and transport measurements were carried out and compared with previously reported observations (see Section 4.4.1).

4.2 Binary 7:3 compounds

Non-centrosymmetric binary compounds with Th_7Fe_3–structure attract attention due to their unusual physical properties. Th_7Fe_3 crystallises in the $P6_3mc$ space group [130] and is superconducting below 1.86 K [131] while its hydrides show ferromagnetic (FM) behaviour [132].

Amongst R_7Rh_3 compounds (where R stands for a rare-earth element), Nd_7Rh_3 has two antiferromagnetic (AFM) phases and a field-induced first-order AFM to FM transition at low temperatures [133,134]. Dy_7Rh_3 displays magnetoresistance (MR) anomalies in the paramagnetic state, which is an uncommon behaviour. Other compounds, which also exhibit unconventional MR behaviour in a similar temperature range (100-200 K), are in a magnetically-ordered state [135]. Tb_7Rh_3 and Gd_7Rh_3 show giant magnetoresistance when in a magnetically-ordered state. In a paramagnetic state, at around room temperature, an anomaly of MR appears in Gd_7Rh_3. Tb_7Rh_3 shows a relatively large MR in its paramagnetic state [136, 137].

The *sd* shell of Ni is filled in the R_7Ni_3 compounds, so it was suggested that Ni does not contribute to their magnetic properties [138]. Single crystals of Pr_7Ni_3 exhibit a large anisotropy of magnetic properties. Pr_7Ni_3 shows ferromagnetic behaviour, when measured along the c-axis and antiferromagnetic properties, when experiments carried out in the c-plane of Pr_7Ni_3 [138]. Ce_7Ni_3 under pressure exhibits non-Fermi liquid behaviour [139]. In Nd_7Ni_3, two antiferromagnetic (AFM) phases and two ferrimagnetic phases exist in different temperature ranges. Additionally,

various metamagnetic transitions have been observed in this material. Recent high pressure experiments show that a low temperature ferrimagnetic phase and a higher temperature AFM phase are more stable than other phases, which are relatively easily suppressed by hydrostatic pressure [140].

Superconductivity was also observed among compounds with Th_7Fe_3–structure. Tran *et al.* reported that superconducting Mo_3Sb_7 is a multigap superconductor [141, 142], on the other hand Khasanov *et al.* show Mo_3Sb_7 is an s-wave, single gap superconductor [113, 143]. Conventional BCS superconductivity have been reported for superconducting Th_7(Fe, Ru, Os, Co, Rh, Ir)$_3$ compounds, despite their NCS structure and localized magnetic moments of f–electrons [144, 145]. Pedrezzini *et al.* studied La_7T_3 (where T is a transition metal) superconducting compounds and found out that La_7(Pd, Rh)$_3$ are BCS superconductors as well [145].

Single crystals of Gd_7X_3 (where X = Pd, Ru) display a strong anisotropy of their magnetic properties. It was suggested that the non-trivial magnetic behaviour of Gd_7X_3 arises due to the exchange interaction between the localized magnetic moments of Gd ions and the frustration effect due to Gd occupying three different crystallographic sites [146, 147]. Presented in this section are examples illustrating several unusual physical properties of non-centrosymmetric A_7B_3 compounds. A member of the 7:3 family, Ru_7B_3 was identified as a good candidate for unconventional superconductivity so the properties of Ru_7B_3 were studied.

4.3 Studies of polycrystalline Ru_7B_3

4.3.1 Superconductivity in polycrystalline Ru_7B_3

NCS Ru_7B_3 crystallises in a hexagonal Th_7Fe_3–structure with a space group $P6_3mc$ [148, 149]. The structure of Ru_7B_3 is shown in Fig. 4.1. There are 20 atoms in its unit cell. Ruthenium atoms form tetrahedra and octahedra, boron atoms sit in other planes. There is no inversion symmetry along the c-axis (see Fig. 4.1(b)) [150].

Matthias *et al.* were the first to report superconductivity in Ru_7B_3 in 1961. Detailed investigations of superconducting properties of Ru_7B_3 were reported nearly 50 years later by Fang *et al.* [150] using a polycrystalline sample and by Kase *et al.* [151] on a single crystal.

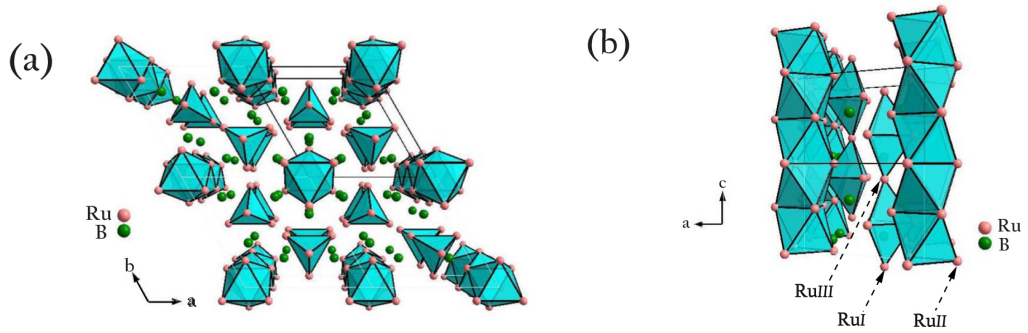

Figure 4.1: The structure of Ru_7B_3: (a) *ab* projection of the Ru_7B_3 structure; (b) *ac* projection of the Ru_7B_3 structure. The Ru atoms at three different coordinations are marked. Taken from [150].

Fang *et al.* [150] studied polycrystalline Ru_7B_3 using magnetic, specific heat and transport measurements. The critical temperature was found to be T_c= 3.3 K, using the resistivity and ac susceptibility measurements. The transitions in zero field were sharp and the residual resistivity ratio (RRR) was 28. The lower critical field was determined to be $H_{c1}(0)$= 110 Oe, using magnetic measurements. The established value of upper critical field, H_{c2} for Ru_7B_3, strongly depends on which experimental technique is used and how the critical temperature is defined (see Fig. 4.2). The H_{c2} determined using magnetic and specific heat measurements gives a value of $H_{c2} \approx 1$ T. This is in agreement with transport measurements only if the critical temperature was defined as the zero-resistance temperature. However if the critical temperature was defined as the temperature of the onset of the superconducting transition in resistivity data, then H_{c2} higher than 5 T was observed.

Fang *et al.* [150] postulated that granular superconductivity and/or large anisotropy might be responsible for such a difference between the observed H_{c2} values. They

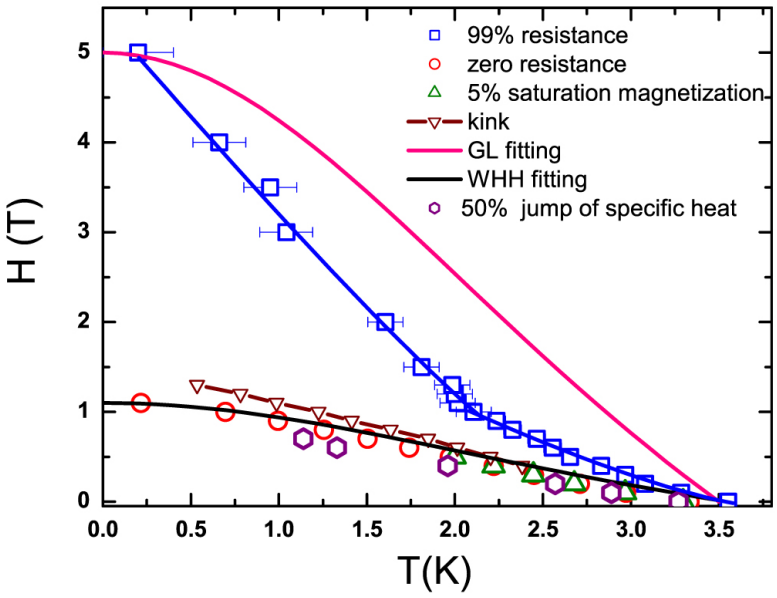

Figure 4.2: The temperature dependence of Ru_7B_3 H_{c2} reported by Fang *et al.* [150]. Fang *et al.* used GL and WHH models to describe their data and these are also shown. Taken from [150].

also suggested that the 'kink' in resistivity data might be evidence of the coexistence of spin singlet and spin triplet pairing in Ru_7B_3.

In the specific heat data, only one anomaly occurs. The Debye temperature was calculated as $\Theta_D = 470.18$ K. The McMillan's electron–phonon coupling constant was $\lambda_{el-ph} = 0.45$, so the authors concluded that Ru_7B_3 is a weak-coupling superconductor. Based on the results of the density of states and band dispersion calculations, Fang *et al.* suggest antisymmetric spin-orbit coupling in Ru_7B_3. They also used specific heat data to analyse the pairing symmetry and deduced that Ru_7B_3 has an isotropic s-wave gap, $\Delta_0 = 0.5$ meV. Additionally, Fang *et al.* derived several superconducting parameters from the measured Hall coefficient and with the assumption that Ru_7B_3 is an s-wave superconductor, it was found that the London penetration depth $\lambda(0)$ is 214 nm and that the coherence length $\xi(0)$, calculated from the BCS expression, is 19.5 nm [150].

4.3.2 Preparation of polycrystalline Ru_7B_3

Polycrystalline Ru_7B_3 was prepared by melting a stoichiometric amounts of constituent elements under an argon atmosphere in an arc furnace with a water cooled copper hearth. The critical temperature of Ru_7B_3 was found to be $T_c = 3.2$ K, from magnetic measurements (see Fig. 4.3), which is in agreement with the literature [150], so the sample quality was assumed to be good.

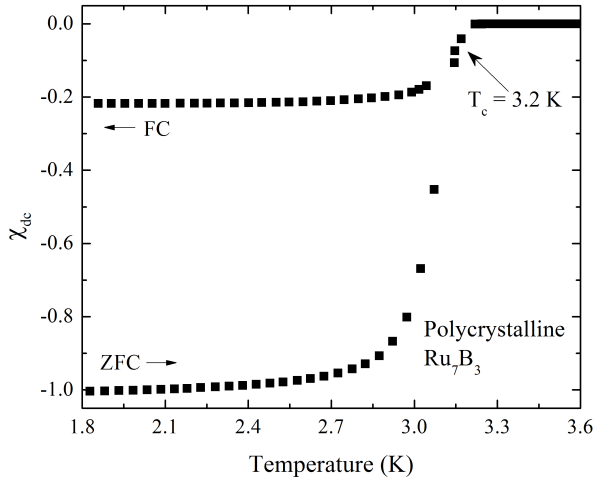

Figure 4.3: Temperature dependence of a magnetic susceptibility, χ_{dc} for the polycrystalline Ru_7B_3. The measurements were carried out using the MPMS, in a low magnetic field of H = 10 Oe.

4.3.3 ZF - μSR Studies of polycrystalline Ru_7B_3

Muon spin relaxation experiments in zero field were carried out using the MuSR instrument in the ISIS facility, Rutherford Appleton Laboratory, United Kingdom. Measurements were performed in zero field on a powdered, polycrystalline sample, which was mounted on a silver plate and inserted into a dilution refrigerator. Measurements were then carried out over a temperature range from 0.055 K to 4 K. For more information about μSR technique, see Sec. 3.4.

Figure 4.4 presents the spectra acquired in both the superconducting and normal states of Ru_7B_3, in zero field. There is a clear difference between the relaxation

rate of Ru_7B_3 in the superconducting and the normal states. No oscillations in the spectra in zero field were observed so there is no long range magnetic order in Ru_7B_3. Only the signal from randomly-orientated nuclear spins is present. The asymmetry of the muon spin polarization relaxes faster for Ru_7B_3 in the superconducting state, than for Ru_7B_3 in the normal state.

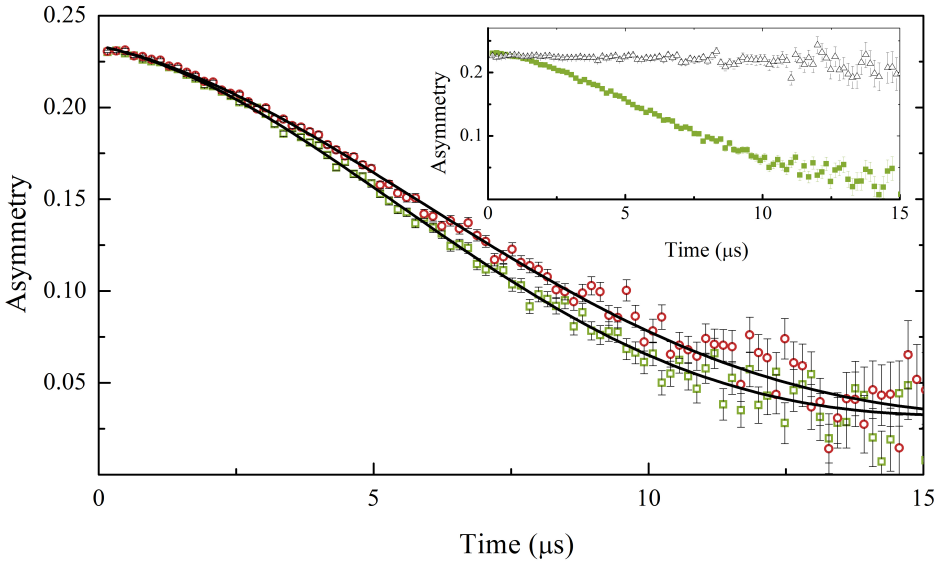

Figure 4.4: The muon spin relaxation spectra for Ru_7B_3 in zero field. Measurements were performed in the superconducting state, at $T = 0.1$ K (green squares) and in the normal state at $T = 3.5$ K (red circles). The curves are a fit to the data with an exponential relaxation with the Kubo–Toyabe function (Eq. 3.10). Inset: The muon spin relaxation spectra at 0.1 K, in zero field (green squares) and in a small longitudinal field, $H = 100$ Oe (black triangles).

T (K)	A_0	Δ_{KT} (μs^{-1})	Λ (μs^{-1})	A_{bcg}
0.1	0.2106 ± 0.0004	0.110 ± 0.001	0.025 ± 0.002	0.0225
3.5	0.2118 ± 0.0004	0.097 ± 0.001	0.029 ± 0.002	0.0225

Table 4.1: Parameters of the fit with Eq. 3.10 to ZF-μSR spectra for the polycrystalline Ru_7B_3 (see Fig. 4.4).

The muon spin relaxation spectra is described well by an exponential relaxation with the Kubo - Toyabe function (Eq. 3.10) and spectra obtained at various temperatures were fitted with this model (see Table 4.1 for the values of the fitted

parameters). Silver has a low nuclear moment, so the background from the silver plate was negligible, and any other contributions to background were not expected to give a temperature dependent signal, so the background term of the fitted equation (Eq. 3.10) was obtained from a measurement at base temperature and then kept constant. The relaxation rate Λ was found to be temperature independent (see Fig. 4.5(b)). The upturn of Δ_{KT}, a parameter associated with the local field distribution width, and its further increase with decreasing temperature is evidence that a spontaneous magnetic field appears in the superconducting state of Ru_7B_3, in zero field. In order to investigate a nature of this field, a small longitudinal field, $H = 100$ Oe, was applied and FC measurements were performed and the spectra at $T = 0.1$ K is shown in inset of Fig. 4.4. It is clear that a small magnetic field is enough to decouple muons from the relaxation channel, which indicates that the spontaneous magnetic field is static or quasi - static on the timescale of muon precession. The appearance of such small spontaneous magnetic field has been also observed in a few other superconducting compounds (see Section 2.2.2). This allows to conclude that time reversal symmetry is broken in superconducting state of Ru_7B_3.

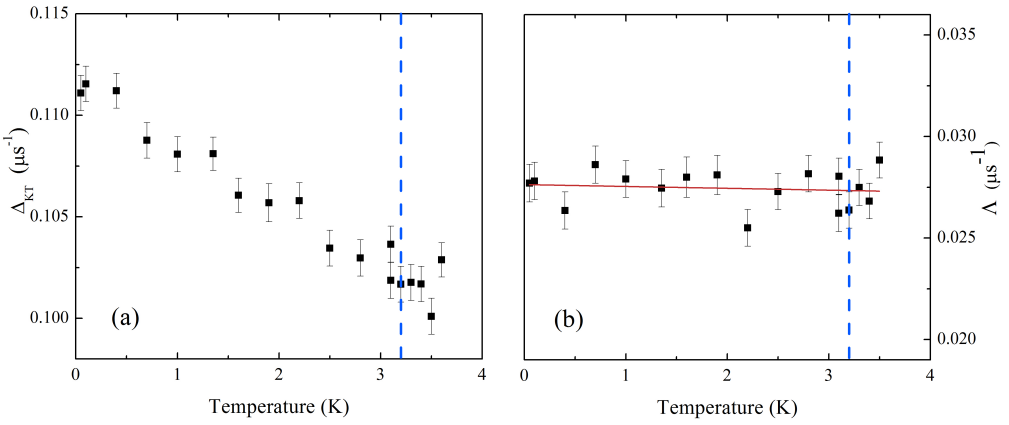

Figure 4.5: Temperature dependence of (a) the width of local field distribution Δ_{KT} of Ru_7B_3 in zero field, (b) the electronic depolarization rate Λ. The values of Δ_{KT} and Λ were obtained from fitting with Eq. 3.10. Dashed, green line indicates T_c.

4.3.4 TF - μSR Studies of polycrystalline Ru_7B_3

TF-μSR studies of Ru_7B_3 were carried out in a range of temperatures and applied magnetic fields. Figure 4.6 presents the time evolution of the asymmetry of muon polarisation for Ru_7B_3. In the superconducting state of Ru_7B_3, below $T_c = 3.2$ K, damped oscillations are present because muons interact with a spatially varying magnetic field of the flux line lattice (Fig. 4.6 (a) and (b)). In the normal state of Ru_7B_3, oscillations with a constant amplitude are present, which suggests that muons experience a uniform, static magnetic field due to the presence of nuclear moments (Fig. 4.6 (c)).

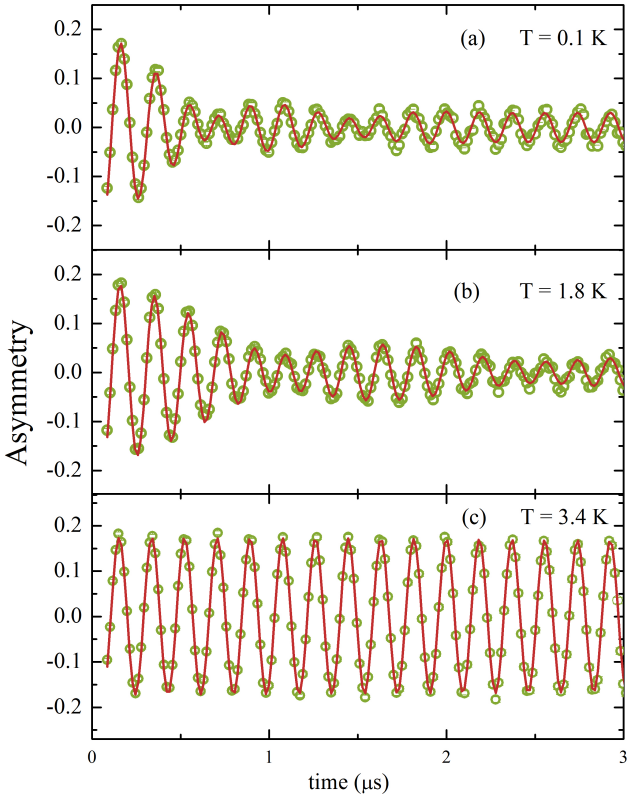

Figure 4.6: Time evolution of the asymmetry of muon polarisation in the superconducting state: (a) T = 0.1 K and (b) T = 1.8 K, and in the normal state (c) at T = 3.4 K, for Ru_7B_3 in a magnetic field of 400 Oe. The curves are fit to data with Eq. 4.1, which includes a sinusoidal oscillations with Gaussian relaxation. Two data sets, from the two virtual, orthogonal detectors were obtained and fitted simultaneously. Only one dataset is shown for clarity.

In the μSR spectra for Ru_7B_3 in the superconducting state, distinct beating was observed. The beating was present at low temperatures (at T = 0.1 K, see Fig. 4.6 (a)), as well as when the temperature increases towards the normal state (see Fig. 4.6 (b), spectra at T = 1.8 K). The presence of the beating in the muon asymmetry spectra suggests that more than one frequency of muon precession could be clearly identified [115]. According to Sidorenko *et al.*, the characteristic beating in P(t) spectra may suggests a presence of a square vortex lattice in a superconductor [115].

The time evolution of the asymmetry of muon polarisation in Ru_7B_3 is well-described by a function which consists of sinusoidal oscillations with Gaussian relaxation (Eq. 4.1).

$$G_x(t) = \sum_{i=1}^{2} A_i \exp(-\frac{\sigma_i^2 t^2}{2}) \cos(\omega_i t + \varphi) + A_3 \cos(\omega_3 t + \varphi) \tag{4.1}$$

where A_1, A_2 and A_3 are the initial asymmetry, σ_1, σ_2 are the muon depolarisation rates, φ is a phase offset of the two virtual detectors, and ω_1, ω_2 and ω_3 are frequencies of muon spin precession and the relation between ω and the magnetic field (B) can be written as $\omega = \gamma_\mu B$. This sum of three components (Eq. 4.1) includes two terms describing the superconducting state (index i = 1,2) and the third term is related to the background contribution (denoted with index i = 3). Silver has a low nuclear moment, so no relaxation due to the background is expected and for the fitting, the value of the initial asymmetry A_3 was fixed to be the same as the low temperature value of A_3. At temperatures close to T_c, the penetration depth is larger, hence the relaxation rate is smaller and damping occurs at longer times so the beating was hard to identify. Hence for spectra measured near T_c, fitting with only two frequencies (Eq. 3.12) was performed. It improved the quality of the fit, lower χ^2_{red} was derived than for fitting with equation which includes three frequencies. Additional frequency was not expected in the normal state, so above T_c also fitting with the equation, which includes only two frequencies (Eq. 3.12), was carried out.

Data acquired from 64 detectors were grouped in two datasets for two virtual, orthogonal detectors and those two datasets were fitted simultaneously with Eq. 4.1. Using described fitting procedure, two different depolarisation rates were found because two distinct frequencies of muon precession are present in the material at the same time. Temperature dependence of muon depolarisation rates for Ru_7B_3 is shown in Fig. 4.7.

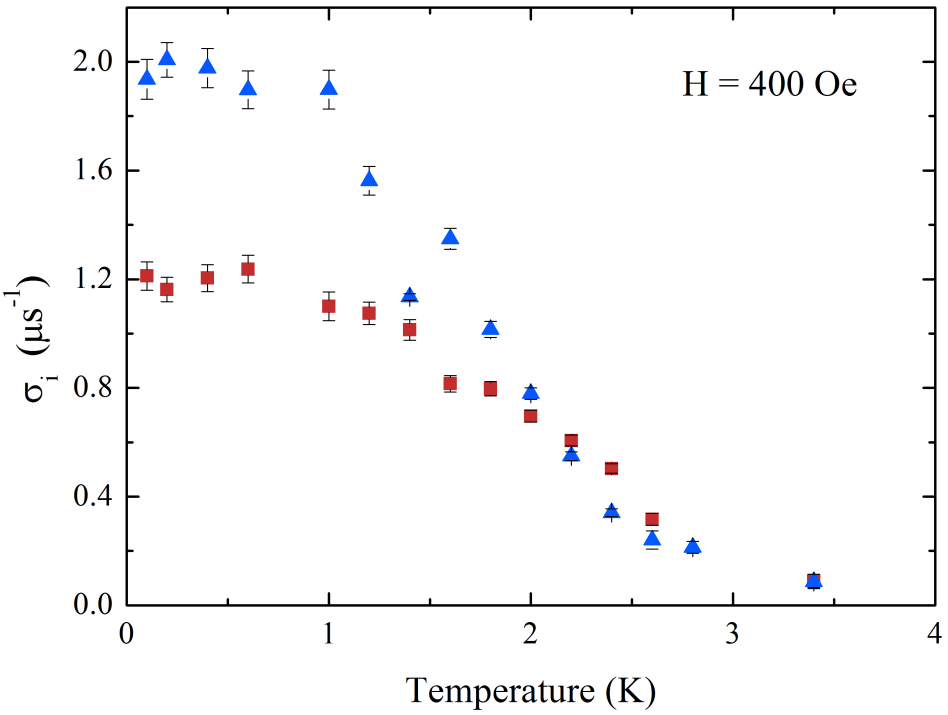

Figure 4.7: Temperature dependence of the muon depolarization rates for Ru_7B_3 in a magnetic field of 400 Oe. The values of the σs shown in the graph were acquired using fitting to TF-μSR spectra with the Eq. 4.1, details of the fitting procedure are given in the text. Two different σs were found because two distinct frequencies of muon precession are present in the material at the same time.

The magnetic field distribution of the FLL can be estimated from the muon asymmetry spectra using the maximum entropy method. The maximum entropy method is a way to avoid numerical approximations or additional assumptions [152]. Tailored for μSR spectra analysis, Maxent algorithm with Fourier-transform [153] was used to study the μSR data and the probability distribution of the magnetic

field from the FLL, p(B) was obtained. The magnetic field from the FLL is not homogeneous. Hence Maxent, which gives the probability distribution of magnetic fields experienced by a muon, is an excellent way to present the distribution of the magnetic field due to the FLL. The series of graphs (see Fig. 4.8) show changes of the field distribution due to the FLL when the temperature increases from base temperature (T = 0.1 K, Fig. 4.8(a)) to above T_c (T = 3.6 K, Fig. 4.8(e)). TF-μSR measurements were carried out in H = 400 Oe and the highest peak in p(B) spectra, at 400 G, comes from muons stopped in a silver plate and the walls of the cryostat. In the Maxent spectra in the normal state of Ru_7B_3 (see Fig. 4.8(e)) only the peak at 400 G is present, which confirms that this peak represents the background. Figures 4.8 (a) to (d) were rescaled in such a way to present a distribution of the magnetic field from the FLL of Ru_7B_3 (whole spectra are shown on the right-hand side of the figures). At T= 0.1 K, near base temperature (Fig. 4.8(a)) two distinct, broad peaks at frequencies lower than the applied magnetic field were observed. As temperature increases towards T_c, the penetration depth becomes larger so vortices overlap and the van Hove singularities became smeared out but still can be identified (see Fig. 4.8(b) and (c), which show the magnetic field distribution from the FLL, measured at T =1.6 and 2 K, respectively). Near T_c (see Fig. 4.8(d) for spectra at T = 2.6 K) a broadening of the 'applied field' peak was observed, which is the only evidence of the presence of the FLL.

The Maxent spectra were fitted with a set of Lorentzian functions and values of the magnetic field, which correspond to the van Hove singularities were identified. The temperature dependence of the obtained values of the magnetic field is shown in Fig. 4.9. For higher temperatures, where the van Hove singularities are hard to identify in the Maxent spectra, the values were obtained from fitting with Eq. 4.1 to time-domain μSR spectra (both datasets shown in Fig. 4.9). Data obtained from the Maxent analysis agree well with the data acquired from fitting to time-domain spectra, as expected.

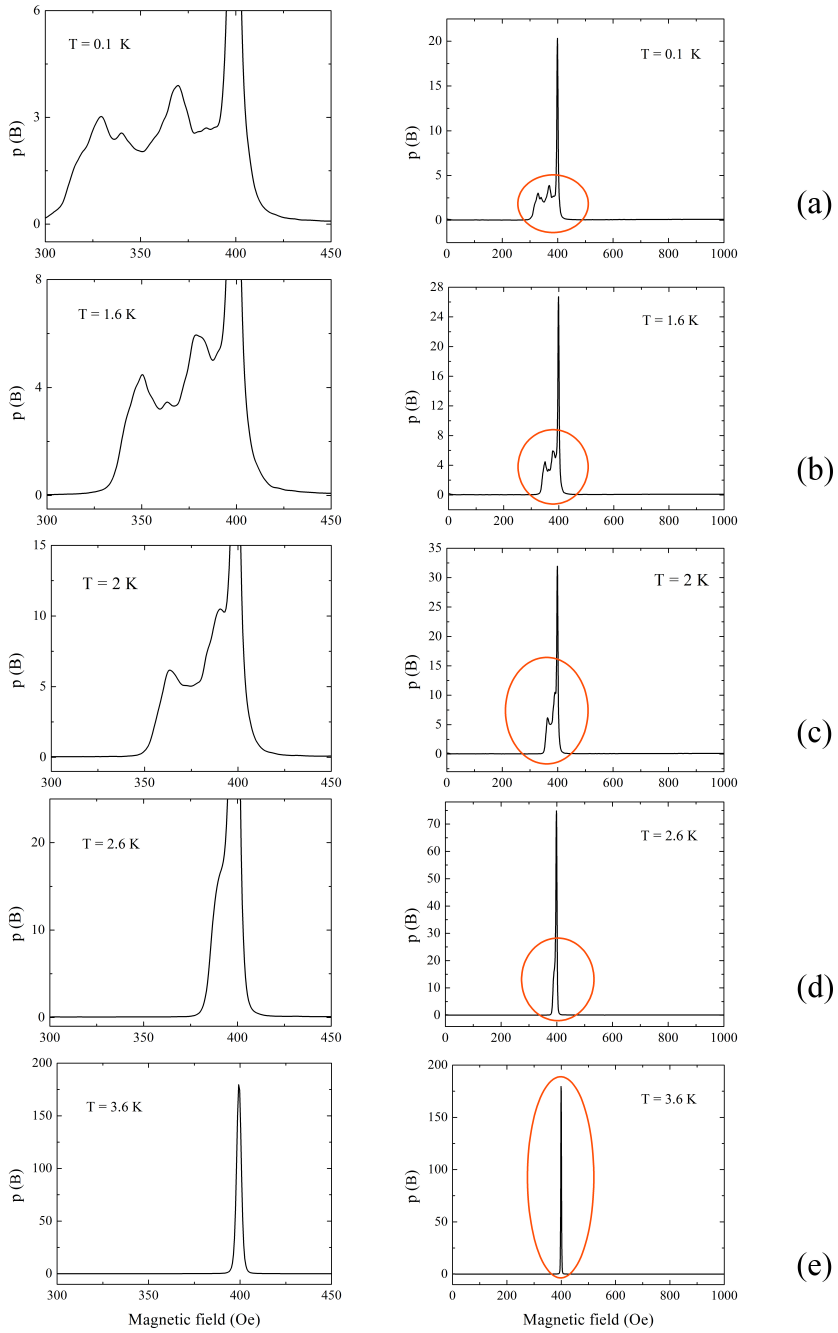

Figure 4.8: Maxent spectra for a polycrystalline Ru_7B_3. The TF-μSR measurements were performed in the applied magnetic field, H = 400 Oe, in the superconducting ((a)–(d)) and normal states (e). Full Maxent spectra are shown on the right-hand side, figures on the left-hand side are zoomed-in on the region where van Hove singularities of the Ru_7B_3 FLL are present (marked by an ellipse on the full Maxent spectra).

In figures 4.8 (a) to (c) two van Hove singularities can be clearly identified. An anisotropic superconductor measured away from a principal axis has two non-equivalent saddle points, so two van Hove singularities are present in its Fourier spectra [115]. The presence of two van Hove singularities can be an evidence for the anisotropy of the FLL in Ru_7B_3. However, two van Hove singularities - from minima and saddle points - can be also observed using a TF-μSR if a square FLL is present in the superconductor [115].

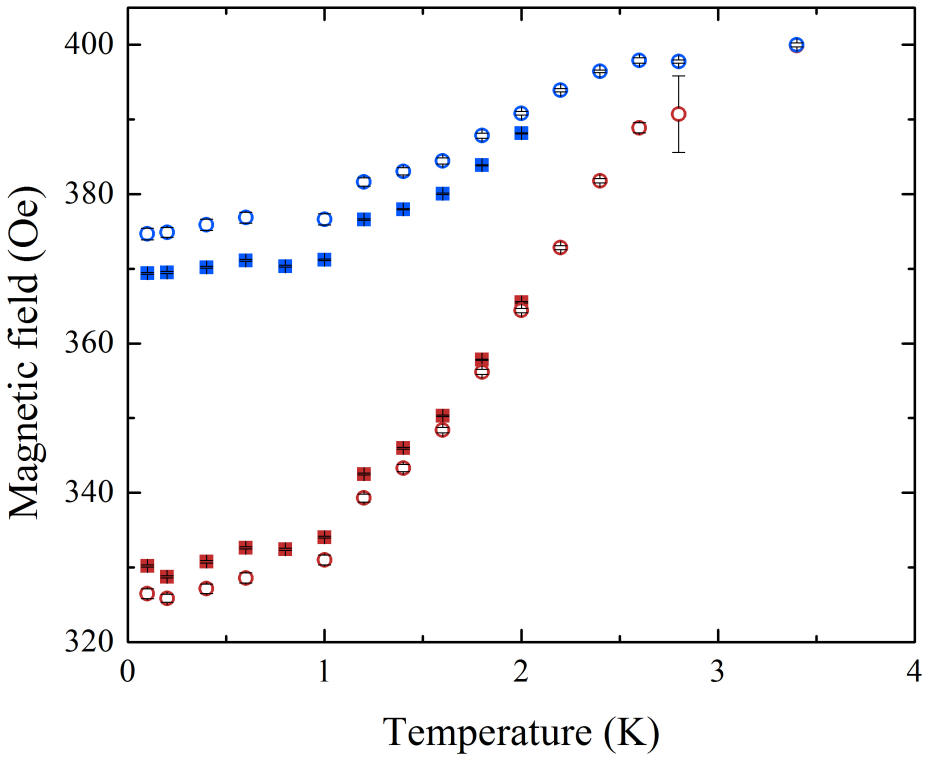

Figure 4.9: Values of the internal magnetic field, which correspond to the van Hove singularities for Ru_7B_3. Data obtained from fitting of the muon asymmetry spectra with Eq. 4.1 (hollow symbols) and data from fitting of p(B) with a set of Lorentzian functions (filled symbols).

If we assume that Ru_7B_3 has a hexagonal vortex lattice (one of the possible scenarios) and it is described well by the London model, then the relation between a muon depolarization rate σ_{sc} (see Eq. 3.13) and the magnetic penetration depth, λ can be written as in Eq. 3.14. The σs with higher values (marked by blue

triangles in Fig. 4.7) corresponds to saddle points (the van Hove singularities) of the Ru_7B_3 FLL and they would be the only singularity observed for a hexagonal lattice (see Section 3.4.3) so these σs were used to derive values of λ^{-2}. Figure 4.10 presents the temperature dependence of λ^{-2} for Ru_7B_3 in an applied magnetic field of 400 Oe. The temperature dependence of the magnetic penetration depth $\lambda(T)$ can be represented by Eq. 4.2 [154, 155]:

$$\frac{\lambda^{-2}(T)}{\lambda^{-2}(0)} = \omega_1 \frac{\lambda^{-2}(T, \Delta_{0,1})}{\lambda^{-2}(0, \Delta_{0,1})} + \omega_2 \frac{\lambda^{-2}(T, \Delta_{0,2})}{\lambda^{-2}(0, \Delta_{0,2})} \tag{4.2}$$

where $\omega_1 + \omega_2 = 1$, show the contribution of each gap to λ and from the London model:

$$\frac{\lambda^{-2}(T, \Delta_{0,i})}{\lambda^{-2}(0, \Delta_{0,i})} = 1 + \frac{1}{\pi} \int_0^{2\pi} \int_{\Delta(T,\varphi)}^{\infty} \left(\frac{\partial f}{\partial E} \right) \frac{E \, \mathrm{d}E \mathrm{d}\Phi}{\sqrt{E^2 - \Delta_i(T, \varphi)^2}} \tag{4.3}$$

where $f = [1 + \exp(E/k_B T)]^{-1}$ is the Fermi function, φ is the angle along the Fermi surface , index $i = 1$ or 2 indicates the respective superconducting gaps and

$$\Delta_i(T, \varphi) = \Delta_{0,i} \, \delta(T/T_c) \, g(\varphi) \ ,$$

where $\delta(T/T_c) = \tanh\{1.82[1.018(T_c/T - 1)]^{0.51}\}$ is the temperature dependence of a superconducting gap given by the BCS theory. The angular dependence of the gap $g(\varphi)$ is 1 for an s-wave or s+s wave gap, for a d-wave gap $g(\varphi)$ is $|cos(2\varphi)|$.

To examine the superconducting energy gap of Ru_7B_3 a fitting with Eq. 5.3 was performed. The presence of one or multiple superconducting gaps was considered, also the presence of different superconducting order parameters (i.e. s-wave and d-wave) was considered. The best fit to the data was obtained with the model for two s-wave gaps (see Fig. 4.10(b)). Residuals for other models suggests that fits significantly deviates from the experimental data (see Fig. 4.10(b)). Hence μSR experiments gives evidence that two s-wave gaps are present in Ru_7B_3 with energies $\Delta_{1,s} = 0.8 \pm 0.3$ meV, $\Delta_{2,s} = 0.32 \pm 0.06$ meV and $\omega_1 = 0.4 \pm 0.2$.

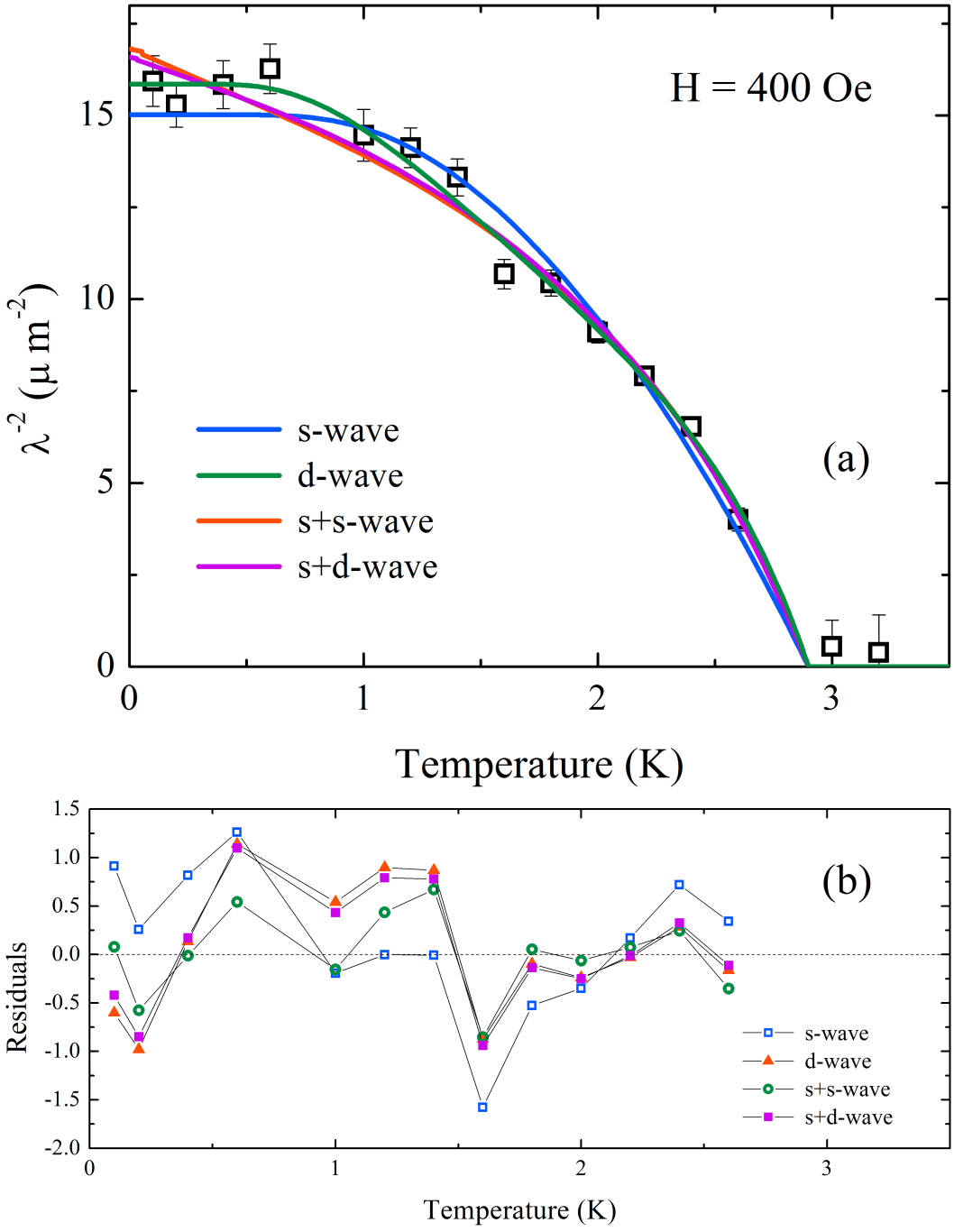

Figure 4.10: (a) Temperature dependence of λ^{-2} for a polycrystalline Ru_7B_3 in the applied magnetic field of 400 Oe. The muon depolarization rates σ_{sc}(T) and Eq. 3.14 were used to calculate λ^{-2}(T). The curves are fit to the data with the model presented in [154, 155]. For fitting of the λ^{-2}(T), Eq. 4.2 was adjusted for the presence of the single s-wave gap (blue curve), d-wave gap (orange curve), two s-wave gaps (green curve) or s-wave and d-wave gaps together (violet curve). See the text for details of the fitting. (b) A plot of the residuals for data points and fitted curves shown on Fig.(a).

4.3.5 μSR Studies of polycrystalline Ru_7B_3 – a summary

Our μSR experiments suggests that Ru_7B_3 is an unconventional superconductor. The measured ZF-μSR spectra gives evidence that TRS is broken in the superconducting NCS Ru_7B_3. Muon spin rotation studies gives evidence that possibly two s-wave superconducting energy gaps are present in Ru_7B_3, and the energies of the gaps are $\Delta_{1,s} = 0.8 \pm 0.3$ meV and $\Delta_{2,s} = 0.32 \pm 0.06$ meV . The presence of multiple superconducting gaps was further studied in single crystal of Ru_7B_3 using TF-μSR (see Section 4.4.4.2).

Additionally, TF-μSR measurements reveals an anomalous behaviour of the FLL. A beating was observed in the asymmetry of the muon polarization for Ru_7B_3 in the superconducting state, which indicates either that an anisotropy of the FLL exists for different crystallographic directions of Ru_7B_3, or a square FLL is present in the superconducting Ru_7B_3 [115]. The polycrystalline sample is a mixture of crystallites with various crystallographic orientations so the degree of potential anisotropy could not be resolved. Experiments using single crystals were necessary to further explore the nature of FLL in Ru_7B_3. Muon spectroscopy and SANS studies of single crystals of Ru_7B_3 were performed. Diffraction pattern of the FLL is measured using SANS, so it is a more direct way to study the symmetry of the FLL.

4.4 Studies of single crystals of Ru_7B_3 and $Ru_7{}^{11}B_3$

4.4.1 Superconductivity in single crystal of Ru_7B_3

The superconducting properties of a single crystal of Ru_7B_3 were recently investigated by Kase *et al.* A single crystal was prepared using the Czochralski method [151] and the crystal also had a hexagonal structure with a $P6_3mc$ space group (C_{6v} point group). The T_c measured using specific heat was in agreement with the onset temperature of superconductivity from magnetic measurements where T_c^{onset}= 2.8 K. The T_cs obtained from the onset of a sharp resistivity transition were $T_c^{onset,res}$= 2.95 K

for J ‖ [100] and 2.8 K for J ‖ [001], respectively and the residual resistivity ratio (RRR) was RRR = 3.7 for J ‖ [100] and RRR = 3.9 for J ‖ [001]. The reported T_c of a single crystal of Ru_7B_3 is significantly lower than the T_c of polycrystalline Ru_7B_3. It is suggested that a loss of boron during crystal growth causes a reduction of T_c. Similar behaviour was observed in single crystals of other compounds with boron [151]. The unit cell of the crystal of Ru_7B_3 was reported to be slightly smaller than unit cell of the polycrystalline sample.

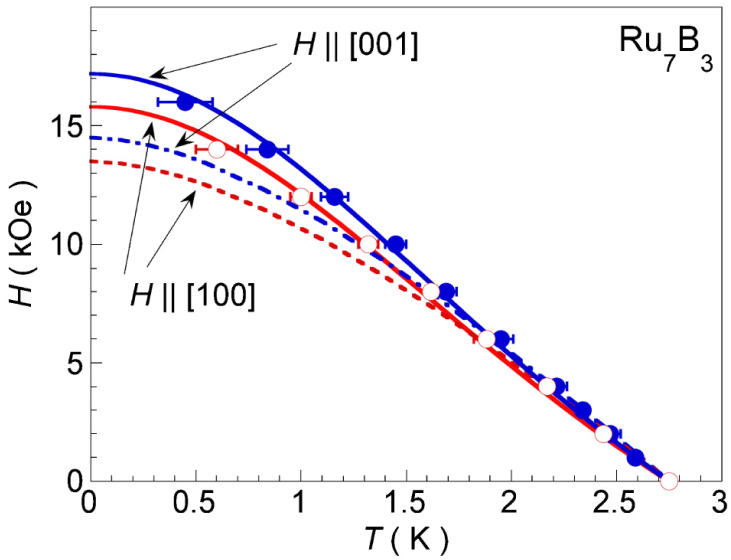

Figure 4.11: Temperature dependence of H_{c2} for single crystal of Ru_7B_3. Curves are fits with the GL theory (solid lines) and the WHH model (dashed lines). Adapted from [151].

The lower critical fields from magnetic measurements were derived to be $H_{c1}(0)$ = 53 Oe for H ‖ [001] and $H_{c1}(0)$ = 68 Oe for H ‖ [100] [151]. Kase *et al.* measured the specific heat in a range of magnetic fields and found a nearly linear field dependence for H_{c2}, which does not follow the WHH model. The values of $H_{c2}(0) \approx 15.8$ kOe for H ‖ [100] and $H_{c2}(0) \approx 17.2$ kOe for H ‖ [001] were found using the fitting with the GL model. Values of H_{c2} estimated from the WHH model were lower, 15.2 kOe for H ‖ [001] and 13.7 kOe for H ‖ [100] [151] (see Figure 4.11).

Using the H_{c1} and H_{c2} values some fundamental superconducting parameters can be calculated. Coherence length of a single crystal of Ru_7B_3 is $\xi_{GL}(0) = 144$ Å, penetration depth is $\lambda_{GL}(0) = 3110$ Å and $\kappa_{GL}(0) = 21.6$ for H ∥ [100]. For H ∥ [001] these parameters were found to be: $\xi_{GL}(0) = 138$ Å, $\lambda_{GL}(0) = 3520$ Å, $\kappa_{GL}(0) = 25.5$ [151]. Calculated using H_{c2} values, the thermodynamic critical field $H_c(0)$ is 520 Oe for H ∥ [100] and 480 Oe for H ∥ [001].

Low temperature specific heat data were fitted with a function derived from the weak-coupling BCS theory and the superconducting energy gap was found to be s-wave, $\Delta(0) = 0.38$ meV [151]. Further confirmation that Ru_7B_3 is a fully gapped superconductor was based on the linear relation between the Sommerfeld parameter, γ(H), and a magnetic field [151].

4.4.2 Single Crystals of Ru_7B_3 and $Ru_7{}^{11}B_3$

The single crystals of the non-centrosymmetric Ru_7B_3 were grown by Prof. G. Balakrishnan and Dr. R.P. Singh using the floating zone technique in a four mirror optical furnace equipped with xenon arc lamps [156]. A single crystal of $Ru_7{}^{11}B_3$ was also prepared. Boron has a high absorption cross section for neutrons, so crystals have also been grown starting with enriched ^{11}B isotope to reduce neutron absorption and hence prepare a single crystals suitable for neutrons experiments. Detail of the crystal growth of both Ru_7B_3 and $Ru_7{}^{11}B_3$ are describe in [156].

4.4.2.1 Laue Difffraction

Back-reflection Laue diffraction was used to align the single crystal of Ru_7B_3 before the experiments, (for more information about the Laue diffraction technique see Section 3.1.3). Figure 4.12 presents the Laue pattern obtained with the x-ray beam direction along the [100] direction of Ru_7B_3 crystal. Figure 4.13 shows simulated patterns for Laue measurements with x-ray beam along [100] and [001] directions of single crystal of Ru_7B_3.

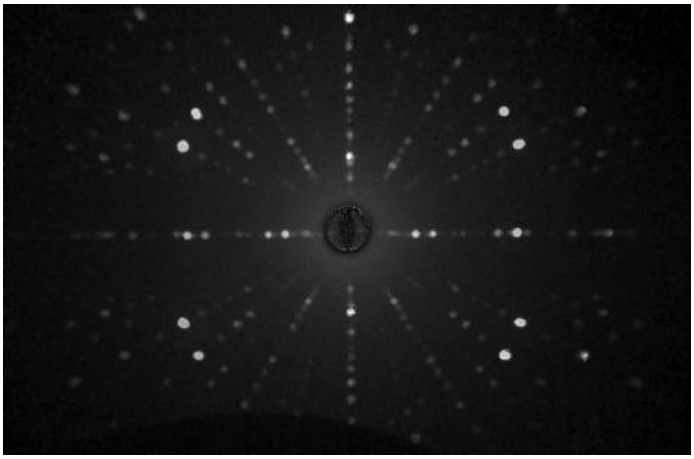

Figure 4.12: X-ray Laue back-reflection pattern of Ru_7B_3. Measurements were performed with the x-ray beam along the [100] direction of the single crystal.

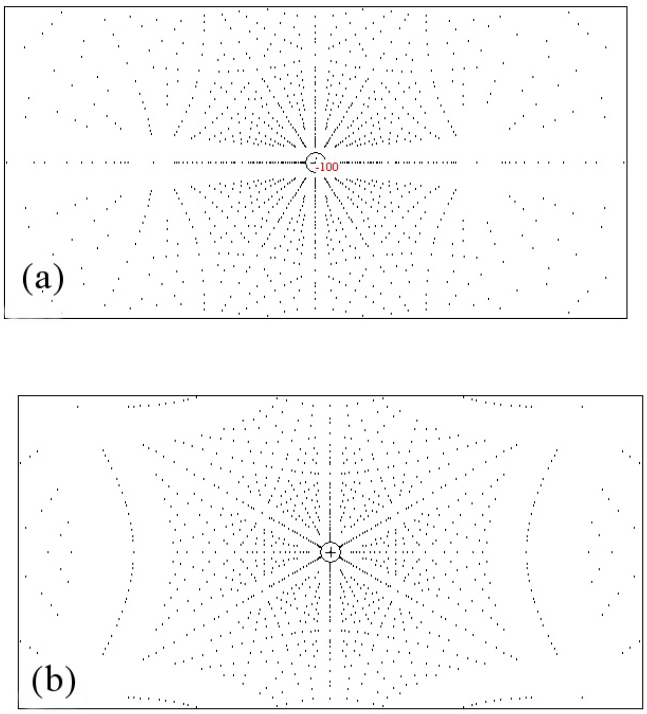

Figure 4.13: Simulated Laue diffraction patterns with x-ray beam along [100] and [001] directions of the Ru_7B_3 single crystal ((a) and (b), respectively). Simulations were made using the *OrientExpress* software [98].

4.4.2.2 Single crystal x-ray diffraction studies of Ru_7B_3 and $Ru_7{}^{11}B_3$

The single crystals of Ru_7B_3 were studied using single crystal CCD X-ray diffraction in the Gemini R diffractometer, Oxford Diffraction. Lattice constants were obtained using the diffraction spectra (see Table 4.2). Our single crystals have a slightly larger unit cell than the crystal described by Kase *et al.* [151], noticeable only to the second decimal place. The unit cell of our Ru_7B_3 crystal is also subtly larger than in our $Ru_7{}^{11}B_3$ crystal. The refinement of B occupancy gives a value of 2.8 ± 1. The large error shows that it was not possible to refine the exact boron occupancy, despite the relatively long count-time. This might be due to boron being much lighter than ruthenium. If the occupancy of B is fixed as 3 the structure is refined well with a $P6_3mc$ space group, which is in agreement with previous reports [151].

	a=b (Å)	c (Å)
Ru_7B_3	7.4783(2)	4.72204(19)
$Ru_7{}^{11}B_3$	7.4697(8)	4.7178(5)
single crystal of Ru_7B_3 [151]	7.441(5)	4.700(4)
polycrystalline Ru_7B_3 [150]	7.4629	4.713

Table 4.2: The lattice constants of Ru_7B_3 and $Ru_7{}^{11}B_3$.

The EDX on SEM measurements of Ru_7B_3 and $Ru_7{}^{11}B_3$ were also carried out. The energies of the main peaks of Ru and B are very similar so it was not possible to find distinct peaks and refine the stoichiometry of the crystals. The peaks of Ru could be identified and possibly some broadening of the observed peak was due to B presence but quantitative results could not be obtained.

4.4.3 Magnetic and transport proprieties of single crystals of Ru_7B_3 and $Ru_7{}^{11}B_3$

Magnetic measurements were performed using the SQUID magnetometer, MPMS (Quantum Design) (for more information about SQUID magnetometry see Section 3.2). Transport measurements were carried out using the four-probe method in ac mode in

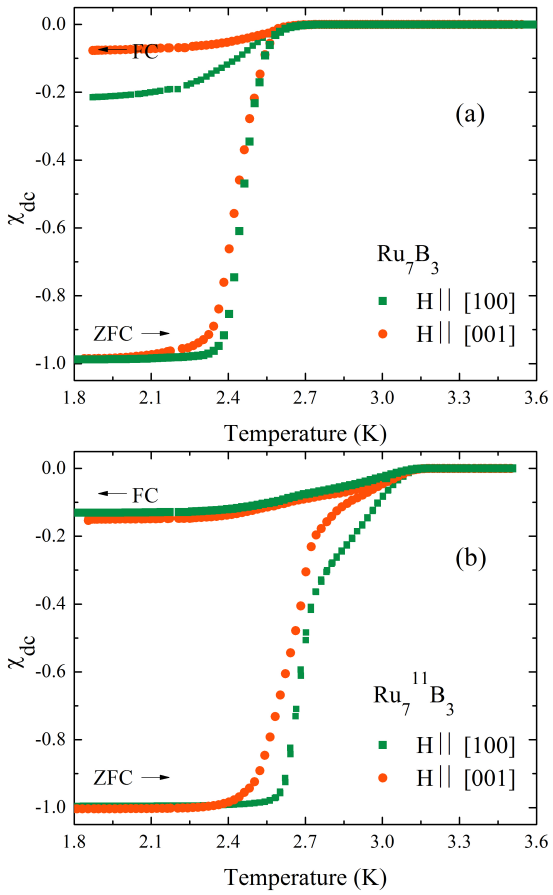

Figure 4.14: Temperature dependence of magnetic susceptibility of (a) Ru_7B_3 and (b) $Ru_7{}^{11}B_3$. The magnetic susceptibility was measured in a low applied magnetic field, H = 10 Oe, parallel to either the [001] direction (red circles) or the [100] direction (green squares) of the single crystal. Measurements were carried out in the ZFC conditions on warming and in the FC conditions on cooling.

a commercial PPMS (Quantum Design). Detail of the transport measurements are given in Section 3.3. Measurements were performed in a range of applied magnetic fields, up to 30 kOe, and the field was applied parallel to either the [100] or [001] directions of the single crystals of Ru_7B_3 and $Ru_7{}^{11}B_3$.

The temperature dependences of magnetic susceptibility of Ru_7B_3 and $Ru_7{}^{11}B_3$ were studied in low applied magnetic field of H = 10 Oe (see Fig. 4.14(a) and (b)). The values of the critical temperatures were found, $T_c^{\text{onset}} = 2.7$ K for Ru_7B_3 and $T_c^{\text{onset}} = 3$ K for $Ru_7{}^{11}B_3$.

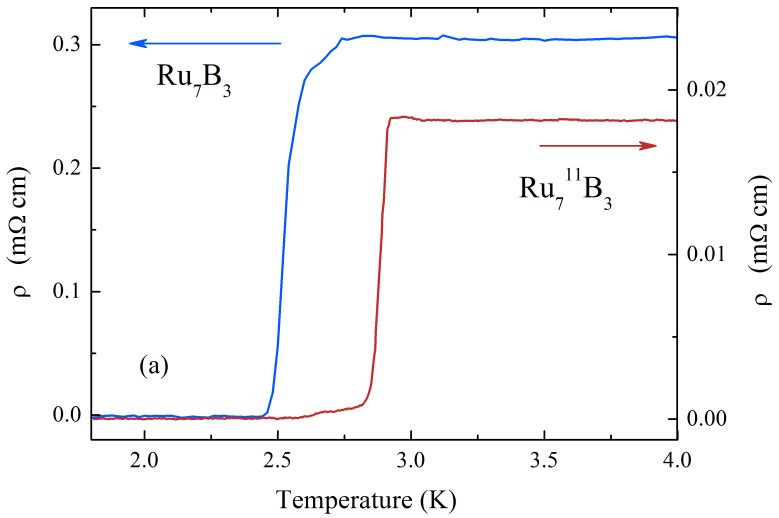

Figure 4.15: Temperature dependence of resistivity of the Ru_7B_3 (blue line) and $Ru_7{}^{11}B_3$ (red line) single crystals in zero field. The critical temperatures are $T_c^{\text{zero}} = 2.5$ K for Ru_7B_3 and $T_c^{\text{zero}} = 2.8$ K for $Ru_7{}^{11}B_3$. Figure is published in [156].

Figure 4.15 shows the temperature dependence of the resistivity of single crystals of Ru_7B_3 and $Ru_7{}^{11}B_3$ measured in zero magnetic field. The Ru_7B_3 single crystal was superconducting at $T_c^{\text{zero}} = 2.5$ K and $Ru_7{}^{11}B_3$ has $T_c^{\text{zero}} = 2.8$ K. Potential origin of the difference between T_cs was discussed in Section 4.4.3.3.

4.4.3.1 Lower critical field

To determine a value of the lower critical fields for Ru_7B_3 single crystal, magnetization was measured as a function of applied magnetic field at various temperatures. The field at which each M(H) curve deviates from linearity was determined. The temperature dependence of the lower critical field, H_{c1} is shown in Fig. 4.16. Measurements were carried out with applied magnetic field along the [100] and [001] direction for Ru_7B_3 (Fig. 4.16 (a)) and $Ru_7{}^{11}B_3$ crystals (Fig. 4.16 (b)). The values of $H_{c1}(0)$ were established from fitting with Equation 4.4:

$$H_{c1}(T) = H_{c1}(0)[1 - (T/T_c)^2] \tag{4.4}$$

Determined values of $H_{c1}(0)$ are 43 ± 2 Oe and 30 ± 1 Oe for Ru_7B_3 and 52 ± 3 Oe and 42 ± 2 Oe for $Ru_7{}^{11}B_3$, with H ∥ [100] and H ∥ [100], respectively. Our values are slightly lower than the values presented by Kase *et al.*, 68 Oe and 53 Oe respectively.

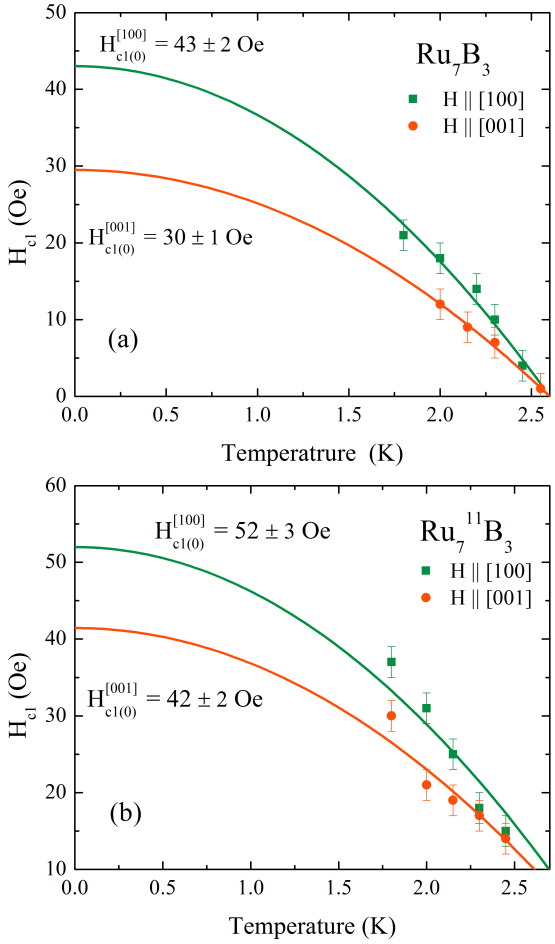

Figure 4.16: Lower critical field (H_{c1}) for (a) Ru_7B_3 and (b) $Ru_7{}^{11}B_3$. The measurements were performed in an applied magnetic field parallel to either the [001] (orange circles) or [100] (green squares) directions of the single crystals. The lines are a fit to the data using Eq. 4.4. Figure (a) is published in [156].

4.4.3.2 Upper critical field

The temperature dependence of resistivity was measured in a range of magnetic fields and the upper critical field H_{c2}(T) of Ru_7B_3 was studied. The T_c onsets from resistivity curves have been used to determine the H_{c2}(T). The H_{c2}(T) (see Fig. 4.17)

do not follow the WHH model [56, 57], which agrees with similar observations made by Kase *et al.* [151] for their data. However, forcing the fit with the WHH model we can obtain values of $H_{c2}(0)$ to be 9.5 and 16 kOe for the applied field parallel to the [100] and the [001] directions of Ru_7B_3 single crystal, respectively (see Figure 4.17). An anisotropy for an initial slope of H_{c2}(T) between the [100] and [001] directions of Ru_7B_3 single crystal was observed.

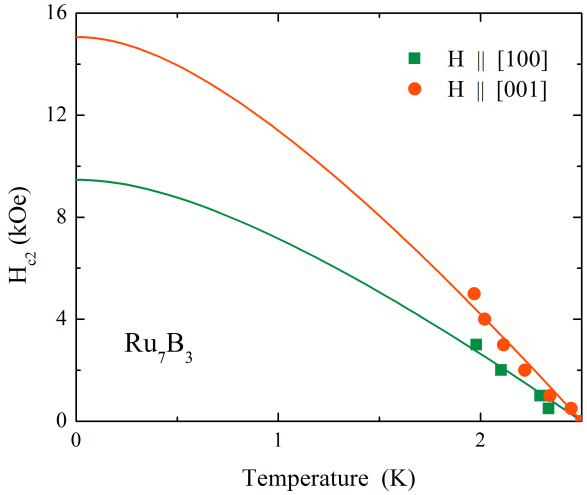

Figure 4.17: Temperature dependence of the upper critical field H_{c2} for the Ru_7B_3. Measurement were carried out with the applied magnetic field parallel to either the [001] (orange circles) or [100] (green squares) directions of the single crystal. The lines are a forced fit to the data with the WHH model. Figure is published in [156].

Also, the H_{c2} for single crystal of $Ru_7{}^{11}B_3$ was examined. The resistivity measurements of $Ru_7{}^{11}B_3$ were performed in the applied magnetic fields up to 26 kOe parallel to either the [100] or [001] directions of the single crystal. Figure 4.18 shows the temperature dependence of H_{c2} of $Ru_7{}^{11}B_3$. The H_{c2}(T) for $Ru_7{}^{11}B_3$ also do not agree with WHH model [56, 57]. A similar trend in the temperature dependence of H_{c2} was reported in a few other unconventional superconductors, for example $PrOs_4Sb_{12}$, see more detail in Section 2.2.2. No significant anisotropy was observed between the [001] and [100] directions of $Ru_7{}^{11}B_3$ crystal. For Ru_7B_3 only very initial slope of H_{c2}(T) was measured, the H_{c2} for $Ru_7{}^{11}B_3$ was observed over a wider range of magnetic fields hence is subject to less uncertainty.

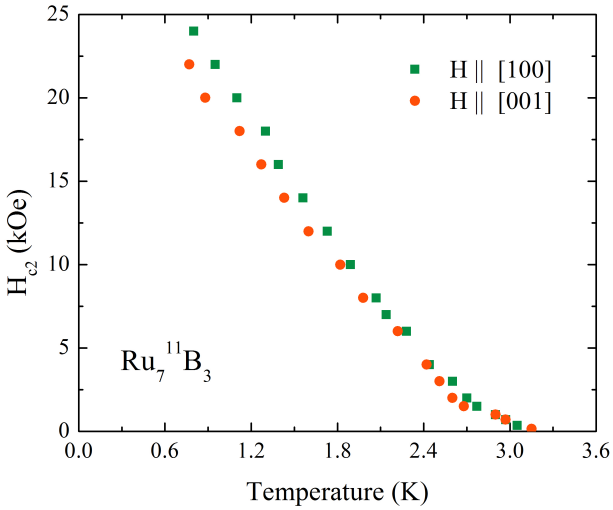

Figure 4.18: Temperature dependence of the upper critical field H_{c2} for the $Ru_7{}^{11}B_3$. Measurements were performed in the applied magnetic field parallel to either the [001] (orange circles) or [100] (green squares) directions of the single crystal.

4.4.3.3 Summary

The superconducting transition measured in single crystals of both Ru_7B_3 and $Ru_7{}^{11}B_3$ is different to that observed in a polycrystalline sample. This is attributed to the slightly different boron losses encountered during the crystal growth process for the crystals, which is common in borides [157]. The T_c values are in agreement with values given in literature [151]. None of readily available laboratory methods could confirm what is exact boron occupancy in our sample. The single crystal x-ray diffraction gives evidence that our single crystals crystallise in the $P6_3mc$ space group, so the same as the polycrystalline sample (see Section 4.4.2.2).

Different stoichiometry may causes slight differences in values of critical fields for our Ru_7B_3 and $Ru_7{}^{11}B_3$ single crystals. The values of the lower critical field were slightly smaller for applied magnetic field parallel to [001] direction of single crystal than for H ∥ [100]. The behaviour of H_{c2}(T) is similar for both crystals and it cannot be described by the WHH model. Investigation of the initial slope of H_{c2}(T) measured for Ru_7B_3 suggests a presence of the anisotropy between the [100] and [001] directions of the crystal. No significant difference was observed between

H_{c2}(T) measured for the [100] and [001] directions of $Ru_7{}^{11}B_3$ crystal and H_{c2}(T) was measure over a wider range of magnetic field.

4.4.4 μSR studies of single crystal of Ru_7B_3

4.4.4.1 ZF - μSR studies of single crystal of Ru_7B_3

ZF-μSR experiments were carried out using the MuSR instrument in ISIS facility, Rutherford Appleton Laboratory, United Kingdom. For μSR measurements, slices of single crystal oriented along the [001] direction were cut out from the as-grown boule. The slices were mounted on a silver plate with the addition of diluted GE varnish (see Fig. 3.5(d)). The sample on the plate was placed in a dilution fridge and measurements were carried out in zero field. The muon beam direction was parallel to the [001] direction of Ru_7B_3 single crystal, so the beam was applied along the direction where the Ru_7B_3 single crystal does not have a centre of inversion. The muon asymmetry was measured in zero field in the superconducting (at T = 0.15 K), as well as in the normal state (at T = 3.5 K) of Ru_7B_3. The acquired data were fitted with a function with Kubo-Toyabe depolarisation (see Eq. 3.10 and the fitted parameters are presented in Table 4.3)). In Figure 4.19, it is clearly visible that muons depolarise faster in the superconducting state than in the normal state. We observed similar behaviour in our polycrystalline sample (see Section 4.3.3). This is evidence that small spontaneous magnetic field was present in Ru_7B_3 in zero field, which indicates that TRS is broken in Ru_7B_3.

T (K)	A_0	Δ_{KT} (μs^{-1})	Λ (μs^{-1})	A_{bcg}
0.1	0.0855 ± 0.0002	0.095 ± 0.001	0.031 ± 0.002	0.1476
3.5	0.0856 ± 0.0002	0.099 ± 0.001	0.035 ± 0.002	0.1476

Table 4.3: Parameters of the fit with Eq. 3.10 to ZF-μSR spectra for the single crystal of Ru_7B_3 (see Fig. 4.19).

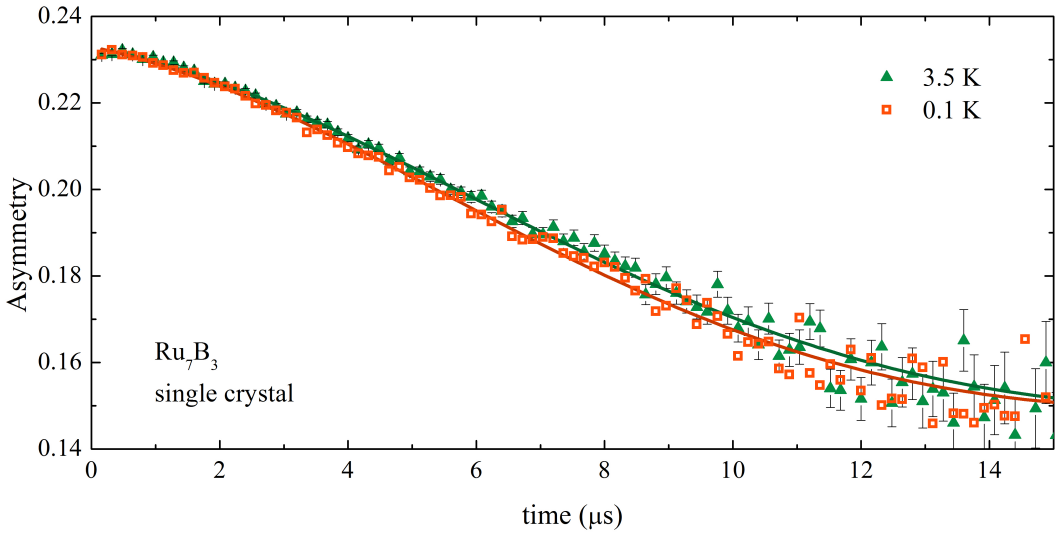

Figure 4.19: Time dependence of the muon asymmetry for the single crystal of Ru_7B_3 at T=0.15 K in the superconducting state of Ru_7B_3 (orange squares), and at T = 3.5 K in the normal state (green triangles). Measurements were performed in zero field. The curves are fits to the data using Eq. 3.10.

4.4.4.2 TF - μSR studies of single crystal of Ru_7B_3

TF-μSR experiments were performed using the same sample of Ru_7B_3 single crystal, which was used in the ZF-μSR experiments (described in Section 4.4.4.1). TF-μSR measurements of Ru_7B_3 single crystal were performed in a magnetic field of 400 Oe, applied parallel to the [100] direction of the Ru_7B_3 single crystal and the muon beam was along the c-axis of the crystal. Figure 4.20 shows the muon asymmetry spectra measured in the superconducting (Fig. 4.20 (a) and (b)) and normal states of Ru_7B_3 (Fig. 4.20 (c)). In the polycrystalline Ru_7B_3, an unusual beating was observed in the TF-μSR spectra for the sample in the superconducting state (see Fig. 4.6(a) and (b)). In the spectra for Ru_7B_3 single crystal in the superconducting state, the beating is harder to recognize due to the low signal to background ratio (see Fig. 4.20(a) and (b)). Two spectra from two virtual, orthogonal detectors were fitted simultaneously with Eq. 4.1 (for more detail about fitting procedure see Section 4.3.4). Beating in the signal was not so pronounce as in the polycrystalline sample, but on average, χ^2 values were around 25 % better if fitted equation assumes a presence of

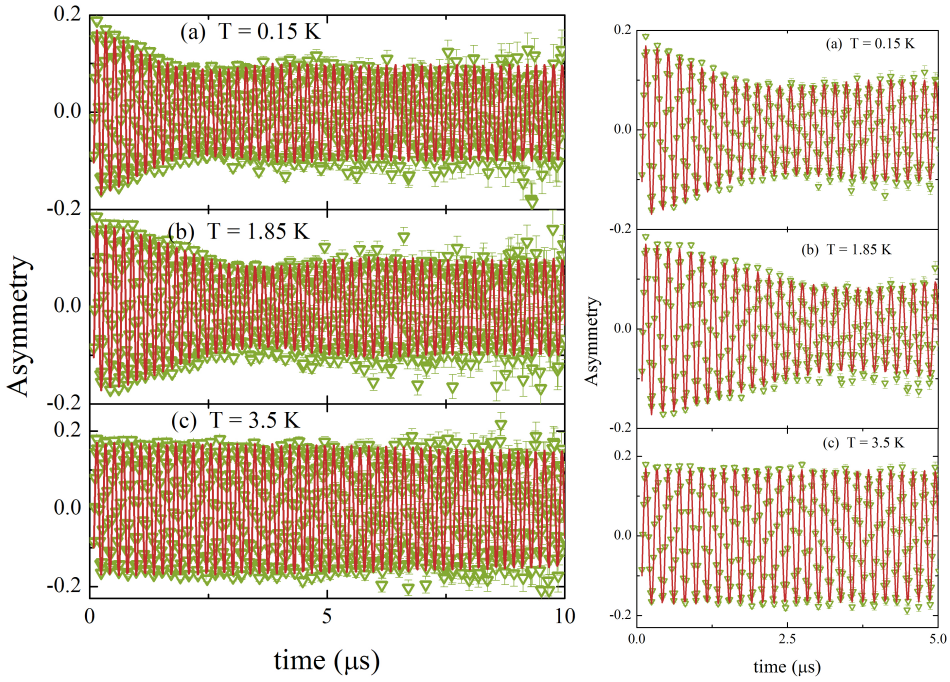

Figure 4.20: Time-dependence of the muon asymmetry spectra for the single crystal of Ru_7B_3 in the superconducting ((a) at T = 0.15 K and (b) at T = 1.85 K) and normal ((c) at T = 3.5 K)) states of Ru_7B_3. Magnetic field, H = 400 Oe was applied parallel to the [100] direction of Ru_7B_3 single crystal. The data were grouped in two virtual orthogonal detectors, only one dataset is shown for clarity of presentation. A function with sinusoidal oscillations and Gaussian relaxation (Eq. 4.1) was fitted to the data (red solid curves). Figures on the right presents the same spectra for short times only.

3 frequencies (Eq. 4.1) rather than only two frequencies (Eq. 3.12) in the spectra. At higher temperatures, beating appears at longer times and becomes too harder to identify, so the uncertainty of identifying/fitting 3 different frequencies became high. Hence for higher temperatures, A_2 in Eq. 4.1 was fixed as 0, so effectively, the fitting was performed with two components.

Figure 4.21(a) presents the muon depolarisation rates which correspond to the penetration depth and the superfluid density, so the behaviour of superconducting gap (gaps) of Ru_7B_3 can be explored. The temperature dependence of the internal magnetic field measured using TF-μSR is shown in Figure 4.21(b). The values below T $\approx$ 2.45 K are lower than the applied magnetic field, H = 400 Oe, so they represents

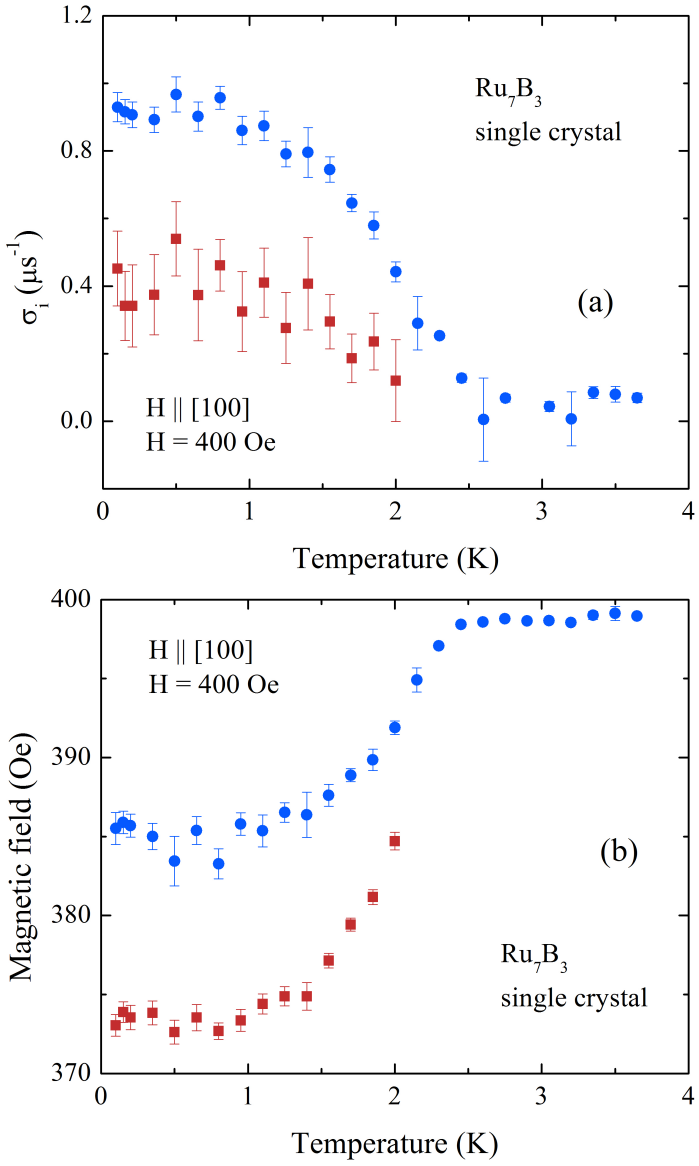

Figure 4.21: (a) Temperature dependence of the muon depolarisation rates, σ_i for Ru_7B_3 in a magnetic field, H = 400 Oe, applied parallel to the [001] direction of Ru_7B_3 crystal. (b) The temperature dependence of magnetic field inside Ru_7B_3 measured using TF-μSR. Two different precession frequencies, which correlate to the van Hove singularities were observed. Data shown on both graphs were obtained using fitting to the muon asymmetry spectra with Eq. 4.1, see text for details of the fitting procedure.

Ru_7B_3 in the superconducting state, where the measured internal magnetic field is reduced due to the nature of the FLL. The two values correspond to two van Hove singularities (see Section 4.3.4 for more details). For Ru_7B_3 in the superconducting state, at low temperatures, the magnetic field from the FLL is nearly constant, until above half-T_c, then gradually increases with temperature. At higher temperatures, a magnetic field saturates around a value of ≈ 400 Oe, so Ru_7B_3 was in the normal state.

The relation between the muon depolarisation rate, σ and the magnetic penetration depth λ can be described by Eq. 3.14. The temperature dependence of λ^{-2} is shown in Fig. 4.22. To study the superconducting gap of Ru_7B_3, λ^{-2}(T) was fitted with Eq. 4.2 and the fitted curves are shown in Fig. 4.22. Eq. 3.14 can be tailored for the presence of multiple gaps with various energies and superconducting order parameters so the fitting was repeated few times to consider different possibilities. Plot of the residuals (see Fig. 4.22(b)) shows that the model which assumes presence of a d-wave gap strongly deviates from the experimental data. This allows to rule out the presence of a single d-wave gap in the superconducting Ru_7B_3. Fitting to the λ^{-2}(T) with the Eq. 4.2 for single s-wave gap or with the Eq. 4.2 for two gaps gives relatively small residuals so those represents good fits to data. Therefore, the simpler model, i.e. a presence of the single isotropic s-wave gap was then assumed to be correct and $T_c = 2.57$ K was estimated, the energy of the gap was found to be $\Delta = 0.44 \pm 0.01$ meV, which is in good agreement with the BCS value [12]. An attempt to fit the data with Eq. 4.2 for two s-wave gaps gives similar values of energy for both gaps ($\Delta_1 = \Delta_2 \approx 0.44$). Studies of the temperature dependence of λ^{-2} with Eq. 3.14 (see Section 4.3.4) for polycrystalline Ru_7B_3 leads to the conclusion that Ru_7B_3 has two s-wave gaps, which is different from the conclusion made for a single crystal. Our estimation using a single crystal data should give more accurate results due to more data points acquired, but the μSR spectra have a relatively large contribution from background, which introduces some uncertainty.

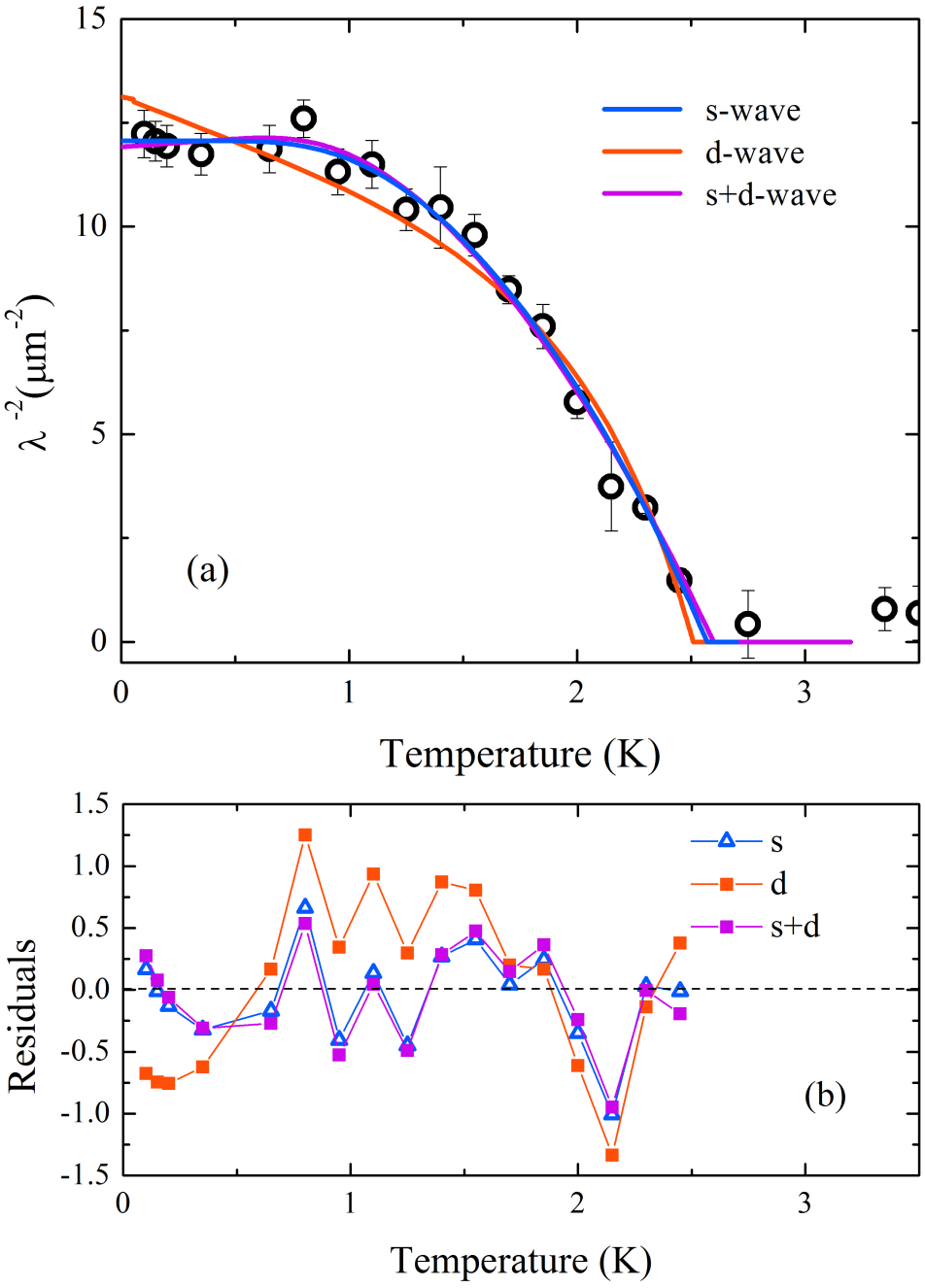

Figure 4.22: (a) Temperature dependence of λ^{-2} in a magnetic field of 400 Oe, applied parallel to [100] direction of Ru_7B_3 single crystal. The curves are fit to the data with Eq. 5.3. The equation was adapted to represent a superconductor with: a single s-wave gap (blue curve), a single d-wave gap (orange curve) and two s- and d-wave gaps (green curve). See the text for details. (b) A plot of the residuals for data points and fitted curves shown on Fig.(a).

4.4.5 Small Angle Neutron Scattering Studies of $Ru_7{}^{11}B_3$

SANS experiments were performed using the D22 and D33 instruments in ILL, France. Neutrons diffracted on the $Ru_7{}^{11}B_3$ FLL were detected by the position-sensitive area detector. Boron has a large absorption cross-section for neutrons so a single crystal of $Ru_7{}^{11}B_3$ with isotopically enriched boron was used, because ^{11}B has a much lower absorption cross section for neutrons than normal B. For the D22 experiment, a cylindrical sample was inserted into the cryostat and the [100] direction of $Ru_7{}^{11}B_3$ single crystal was parallel to the neutron beam and magnetic field directions. Our previous μSR experiments shown possible evidences of anisotropy in the FLL of Ru_7B_3 so studies of different crystallographic orientations were required. For the D33 experiment, a cylindrical sample was inserted into the cryostat and the [001] direction of $Ru_7{}^{11}B_3$ single crystal was parallel to the neutron beam direction. The sample was measured in a range of magnetic fields and temperatures. Prior to SANS measurements in a particular magnetic field, the sample was cooled in the applied magnetic field from normal state to the base temperature ($T \approx 1.55$ K) and the measurements were carried out on warming.

Figure 4.23 presents the SANS diffraction pattern of the FLL from the [100] direction of $Ru_7{}^{11}B_3$ single crystal in an applied magnetic field $H = 2000$ Oe and $T = 1.7$ K. The FLL with a distorted hexagonal symmetry was observed. The measurements were carried out with a wavelength $\lambda_{wv} = 8$ Å and the sample-detector distance was 17.6 m. The pattern in Fig. 4.23 was generated by summing frames for a range of small rotations (by 2°, maximum) about a horizontal and vertical axes (the geometry of SANS experiment is shown on Figure 3.14). A similar series of measurements was performed in the normal state and acquired frames were used for the background subtraction. Spectra measured near the centre of the detector are dominated by a very intense contribution from the direct beam, so the area in the centre of the pattern was masked to ensure a clear presentation of the Bragg spots from the FLL. Additionally, for clarity, a smoothing function was applied. The

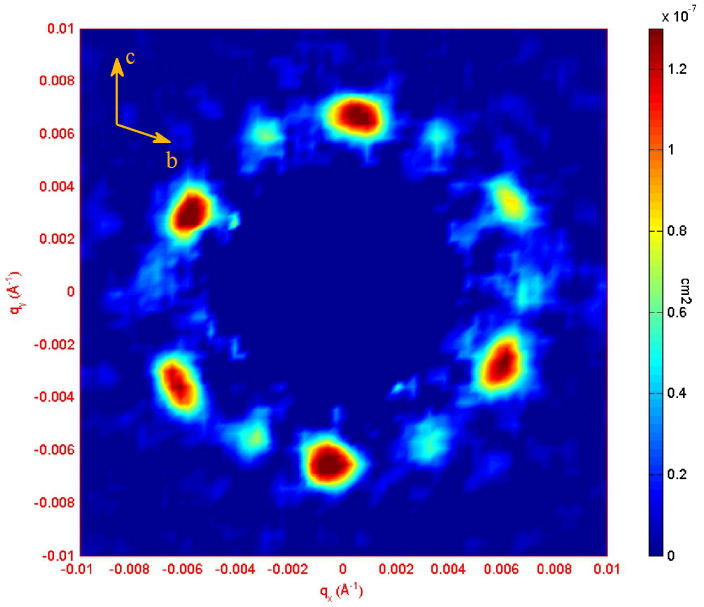

Figure 4.23: SANS diffraction pattern of $Ru_7{}^{11}B_3$ FLL at $T = 1.7$ K in the magnetic field $H = 2000$ Oe applied along the [100] direction of $Ru_7{}^{11}B_3$ single crystal. Measurements were performed using the D22 instrument in ILL. The diffraction pattern was generated by summing frames for a range of small rotations about the horizontal and vertical axis. The background was subtracted, see the text for details.

observed Bragg spots form a distorted hexagonal pattern. The angles between the spots were measured to be in the range of 50 to 70 degrees. A second domain of six, much weaker, additional spots, was also observed, in between the spots of the first pattern, approximately 30 degree apart (see Fig. 4.23).

The magnitude of the scattering vector q is related to the magnetic field B [158]:

$$q_0 = 2\pi(B/\phi_0 \sin\beta)^{\frac{1}{2}} \tag{4.5}$$

where β is an opening angle, $\beta = 60°$ (or $120°$) for a hexagonal FLL and $\beta = 90°$ for a square FLL. Figure 4.24 shows a radial q-average of intensity for the whole detector area. The peak in the data presented in Fig. 4.24 corresponds to the mean field of the FLL. Gaussian function was fitted to the data and a value of

q = (0.00672±0.00003) Å^{-1} was obtained. The magnitude of the scattering vector q is related to B as in Eq. 4.5, so q = (0.00672±0.00003) Å^{-1}, which corresponds to the mean field from the FLL, $B = (2.1 \pm 0.1)$ kG, when β was taken as an average of the angles from the FLL, so $\beta = 60 \pm 3°$.

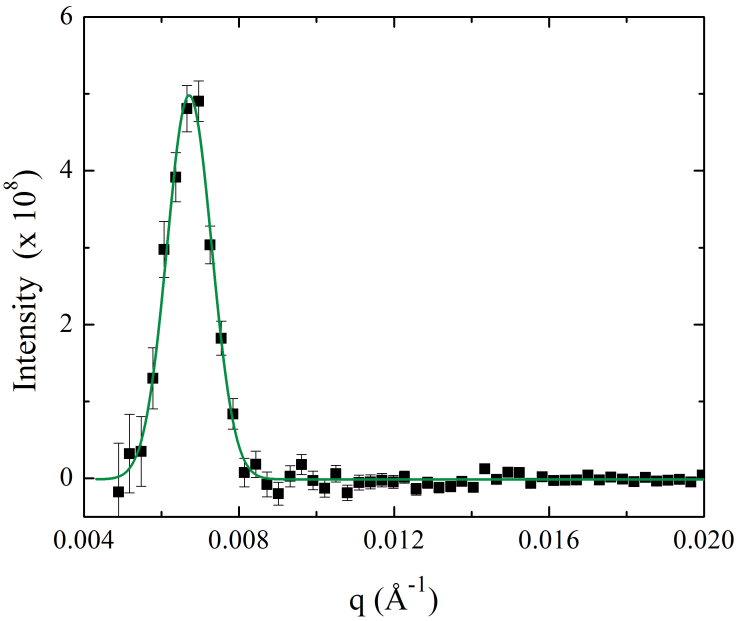

Figure 4.24: Radial q-average of the intensity for the detector area. $Ru_7{}^{11}B_3$ was measured in an applied field, $H = 2000$ Oe. The curve is Gaussian fit to the data. See the text for details.

Unusual time evolution of TF-μSR spectra for superconducting Ru_7B_3 (see Sections 4.3.4 and 4.4.4.2) suggested that FLL of Ru_7B_3 has possibly either a square symmetry or anisotropy of the FLL exists between different crystallographic directions. A square vortex lattice was not observed, so a potential presence of anisotropy was investigated. For observed hexagonal lattice, pattern of Bragg spots forms an ellipse and the ratio of the axis of an ellipse (ϵ) is 1 for an ideal FLL. For a superconductor with anisotropic FLL, ϵ changes for SANS measurements performed with the principal axis of the crystal rotated away from the direction of the neutron beam (and the direction of the magnetic field) [127, 159]. The anisotropy can be calculated using

Eq. 4.6 [159, 160] based on the model presented by Campbell *et al.* [160]:

$$\epsilon^2 = \frac{\gamma_A^2}{sin^2\psi + \gamma_A^2 \cos^2\psi} \tag{4.6}$$

where ψ is the angle between the direction of the applied magnetic field and the principal axis of a single crystal; ϵ is the ratio of the major to minor axes of ellipse, which is formed by the Bragg peaks, and γ_A is the penetration depth anisotropy.

In order to investigate the presence of the FLL anisotropy, the [100] direction of the single crystal was rotated away from the magnetic field and beam directions. Figure 4.25(a) shows the diffraction pattern for the FLL along the [100] direction of $Ru_7{}^{11}B_3$ crystal. Reciprocal images of the $Ru_7{}^{11}B_3$ FLL, when the sample was rotated away by 20° and 40° are presented in Fig. 4.25(b) and Fig. 4.25(c), respectively.

Several frames for a range of rotations (by small angles, maximum of 1° or 2°) about a horizontal and vertical axis were summed together to form the patterns shown on Fig. 4.25. Appropriate measurements, usually a few frames, taken above T_c, were used to represent the background and those frames were subtracted. Also, a short measurement of the direct beam transmission was subtracted from the data to obtain the absolute values of the intensity. A smoothing function was applied fora clarity of presented in Fig. 4.25 patterns, but all calculations were performed using the data without any smoothing function.

To find ϵ, the coordinates of the centres of the Bragg spots were found for each spot to calculate the distances between pairs of opposite spots. Then the ratios of major to minor axes of ellipse were derived. Figure 4.26 presents the ellipse ratio, ϵ, as a function of the angle of rotation away from a axis of the $Ru_7{}^{11}B_3$ single crystal. Only slight deviation from the value of $\epsilon = 1$ was observed, so it can be concluded that only a very weak, if any, anisotropy was observed along the FLL from the [100] direction of the crystal. The lack of anisotropy observed may be due to the fact that the sample was not rotated far enough to detect any anisotropy or there

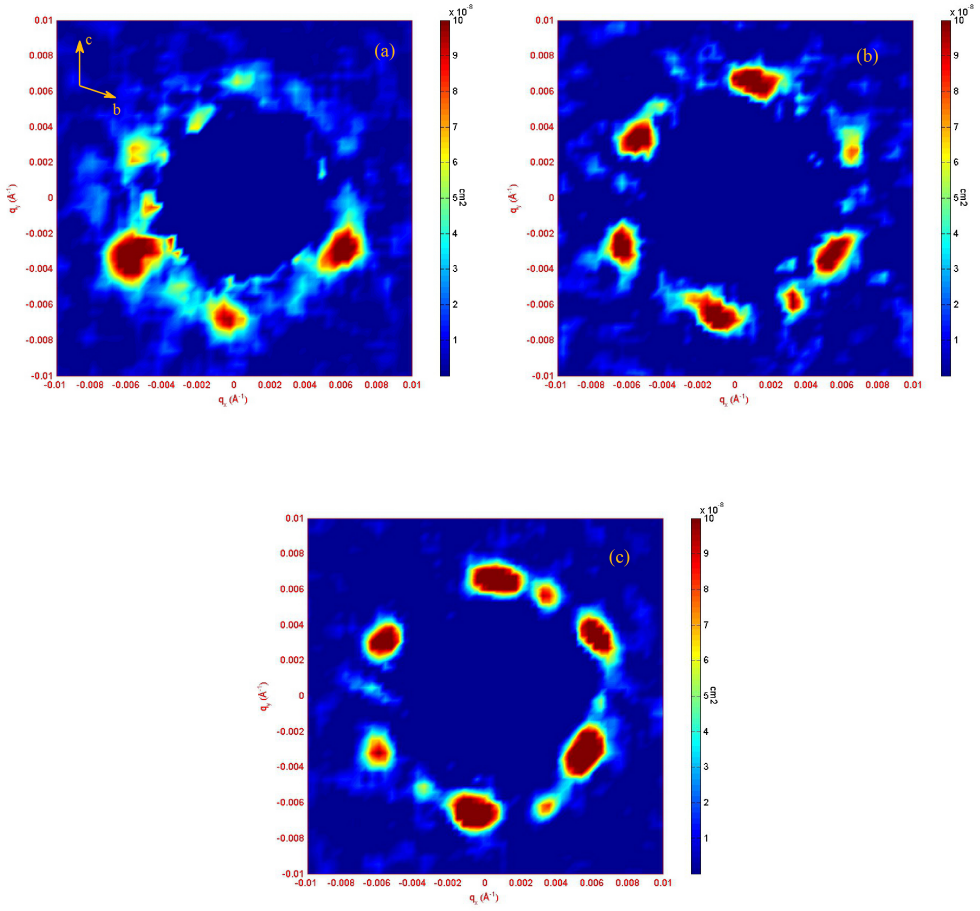

Figure 4.25: SANS diffraction pattern for $Ru_7{}^{11}B_3$ FLL in the applied magnetic field, $H = 2000$ Oe and at $T = 1.7$ K. Measurements were carried out using the D22 instrument in ILL, using the neutron beam with a wavelength $\lambda_{wv} = 8$ Å. The [100] direction of Ru_7B_3 single crystal was rotated: (a) 0°, (b) 20° and (c) 40° away from the neutron beam and magnetic field directions. The pattern was generated by summing frames for a range of rotations (by a 1° or 2°, maximum) about horizontal and vertical axis. A background was subtracted. See the text for more information.

was no anisotropy between the a axis and the direction towards, which the crystal was rotated. Hence, measurement were also performed with the [001] direction of $Ru_7{}^{11}B_3$ single crystal rotated, by 30 - 75 °, away from the neutron beam and the magnetic field directions.

The [001] direction of $Ru_7{}^{11}B_3$ single crystal was positioned parallel to the

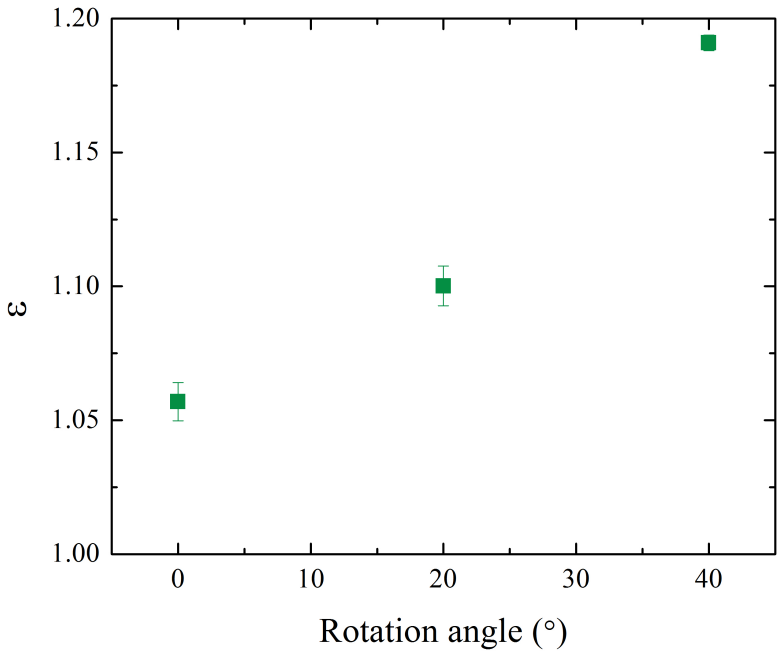

Figure 4.26: Ellipse ratio (ϵ) as a function of the angle of rotation the sample away from the neutron beam direction. SANS diffraction patterns were measured at $T = 1.7$ K and in $H = 2000$ Oe for the [100] axis of the Ru_7B_3 single crystal rotated away from the neutron beam and magnetic field directions. Two pairs of orthogonal spots were used to find ϵ.

neutron beam and the measurements were performed using the D33 instrument in ILL with $\lambda_{wv} = 14$ Å and the sample-detector distance was 12.5 m. The measurements were performed in a magnetic field of 400 Oe at $T = 1.7$ K, for the c axis of the crystal rotated away from the neutron beam and magnetic field directions by 0° (Fig. 4.27(a)), 30° (Fig. 4.27(b)), 45° (Fig. 4.27(c)) and 75° (Fig. 4.27(d)). The background and the direct beam contributions were subtracted and the absolute values of the intensity were obtained. For clarity, different intensity scales are used in Fig. 4.27. Several frames acquired when the sample was rotated about the horizontal and vertical axis (by a couple of degrees, maximum) were summed together to obtain the Bragg-scattered patterns shown on Fig. 4.27. If the measured rocking curve is quite sharp, the angle of incidence needed to be adjusted to fulfil the Bragg diffraction condition and observe a particular Bragg-spot. Some spots in the observed pattern (Fig. 4.28)

are weaker than others, due to them not being measured at the exact angle given by Bragg diffraction condition (not *rocked on*). This is due to a lack of experimental time. The neutron beam time is limited and one needs to balance which information are necessary and which can be omitted.

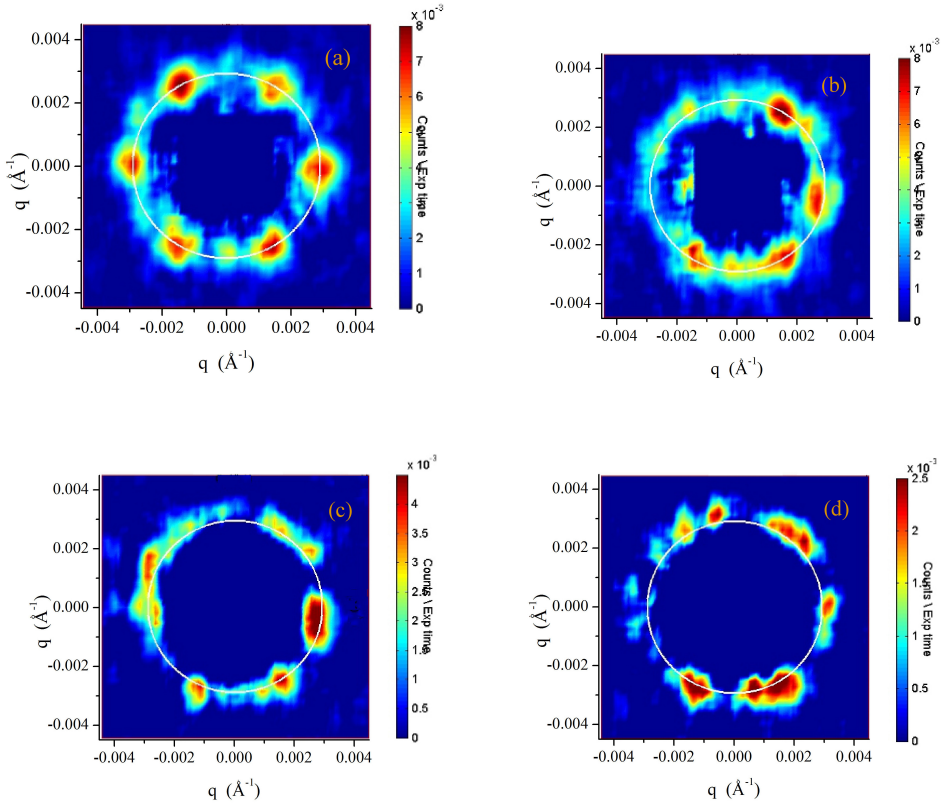

Figure 4.27: (a) Bragg-scattered pattern of the FLL for the [001] direction of $Ru_7{}^{11}B_3$ single crystal. Measurements were carried out in a magnetic field of 400 Oe and at $T = 1.7$ K. Figures (b), (c) and (d) show reciprocal patterns of $Ru_7{}^{11}B_3$ FLL for the c axis of the crystal rotated, respectively, 30, 45, 75 degrees away from the neutron beam direction. The patterns are a result of summing several frames together. Background and direct beam contributions were subtracted. White circle indicates the q-position for the Bragg spots from a hexagonal FLL with $B = 400$ Oe (q was calculated from Eq. 4.5). See the text for details.

For experiments carried out with the [001] direction of the $Ru_7{}^{11}B_3$ crystal parallel to the neutron beam, a distorted hexagonal lattice was observed and a second domain of much weaker spots was also visible (see Fig. 4.28). The maximum of

intensity for the radial-q average of the detector area was found at q = 0.00293 ± 0.00001 Å^{-1}, which leads to $B = 390 \pm 3$ G (from Eq. 4.5). For experiments carried out with the [001] direction of the $Ru_7{}^{11}B_3$ crystal parallel to the neutron beam, a distorted hexagonal lattice was observed and a second domain of much weaker spots was also visible (see Fig. 4.28). The maximum of intensity for the radial-q average of the detector area was found at q = 0.00293 ± 0.00001 Å^{-1}, which leads to $B = 390 \pm 3$ G (from Eq. 4.5). The data were analysed in a similar way to analysis performed for the data obtained for Ru_7B_3 measured along the [100] direction of the crystal and values of ϵ were derived. Figure 4.28 shows the ellipse ratio (ϵ) as a function of the angle of rotation away from the neutron beam and magnetic field directions for c axis of $Ru_7{}^{11}B_3$ single crystal. The values of ϵ for all measured rotation angles were very close to 1, which is similar to the ϵ obtained for the FLL formed along the [100] direction of $Ru_7{}^{11}B_3$ crystal. So no evidence of anisotropy was observed.

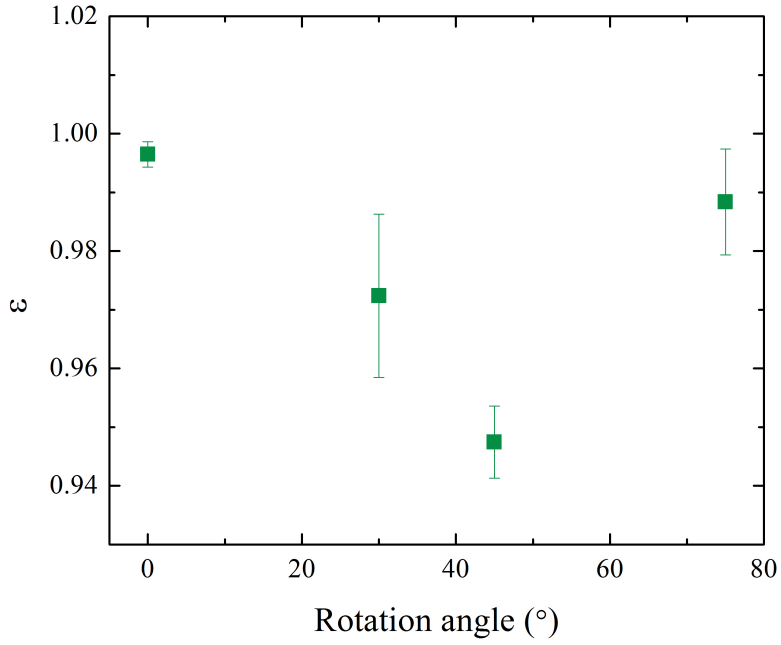

Figure 4.28: Ellipse ratio (ϵ) as a function of the angle of rotation away from the neutron beam and magnetic field directions for the [001] direction of $Ru_7{}^{11}B_3$ single crystal. SANS measurement were carried out at $T = 1.7$ K in $H = 400$ Oe.

Our previous μSR experiments which suggested the presence of either a square vortex lattice or anisotropy of the FLL in Ru_7B_3, but neither of them was observed using SANS, so origin of the unusual beating in TF-μSR spectra was not determined. Then presence of other phenomena was considered. An interesting feature was observed in the SANS diffraction pattern of the for Ru_7B_3. Six additional spots, the second domain, were observed for both measured principal directions of the crystal and also with the a and c axes of the crystal rotated away from the beam and magnetic field directions (see Fig. 4.25 and Fig. 4.27). The presence of additional domain might be evidence that measured sample includes two pieces of a crystal with different orientation, but the single crystals for the experiments were carefully examined using Laue diffraction and additional precautions were taken during preparing of the subsequent sample for the second experiment (in D33). The Bragg-spots, which form the second domain were 30 degrees apart, for the [100] and [001] directions of $Ru_7{}^{11}B_3$ single crystal (see Fig. 4.25(a) and Fig. 4.27(a)). When the principal axis of Ru_7B_3 single crystal were rotated away from the beam direction, the spots of the second domain slightly reorientate (cf. Fig. 4.27) and get closer to the spots of main brighter domain. The lattice reorientation might be further evidence of a multiband FLL in Ru_7B_3 (similar scenario was suggested for MgB_2 by Cubitt *et al.* [127], see Sec. 3.5.1). MgB_2 also experiences an unusual temperature dependence of H_{c2} [59], similar to the behaviour of H_{c2} in Ru_7B_3 (also observed in $PrOs_4Sb_{12}$ see Section 2.2.2). It has been suggested that the Pauli-limiting field (which if dominant leads to unusual H_{c2} behaviour) plays an important role for the potential formation of exotic FLL states in the vicinity of the upper critical field [128,129] (see Sec. 3.5.1). Further studies of the FLL behaviour in high magnetic fields might be necessary to arrive at any conclusions about the nature of the second domain.

The relation between measured neutron reflectivity (R) and the form factor

(F_{hk}) can be written as [158, 161]:

$$R = \frac{2\pi\gamma_n^2\lambda_{wvl}^2 t}{16\Phi_0^2 q} F_{hk}^2 \tag{4.7}$$

where λ_{wvl} is the wavelength of neutrons, $\gamma_n = 1.91$ is the neutron gyromagnetic ratio , $\Phi_0 = hc/2e$ is the flux quantum and t is the thickness of the sample.

The magnetic field dependence of the form factor carries information about the penetration depth and hence about the superfluid density of studied superconductor. For the BCS-superconductors with a single, isotropic gap, F_{hk} is well described using Eq. 4.8. London approximation was used to find Eq. 4.8, so is only appropriate for a high-κ superconductor [19]:

$$F_{hk} = \frac{B}{1 + q_{hk}^2\lambda^2(T)} \tag{4.8}$$

where q_{hk} are wavevectors of a first order reciprocal lattice due to the FLL.

The form factors for the FLL along the [100] direction of $Ru_7{}^{11}B_3$ single crystal were calculated using Eq. 4.7 for the Bragg spots forming the main brighter domain. Due to the limited experimental time, we could not acquire full rocking curves for several patterns measured in different fields and temperatures, so one SANS pattern may contain spots with different intensities. The values of neutron reflectivity (R) taken from the peak intensity in the radial q-average of the whole detector area are a good approximation and those values of R were used to calculate the form factors with Eq. 4.7. The magnetic field dependence of the F_{hk} for SANS measurements of the FLL along the [100] direction of $Ru_7{}^{11}B_3$ crystal is shown in Fig. 4.29. For a conventional superconductor, the field dependence of F_{hk} plotted on a logarithmic scale should be linear (see Eq. 4.8). Lack of sufficient data does not allow to draw any conclusions if this or other models describe the data. A linear fit was performed for F_{hk}(H) to allow to compare the trend with the model given by Eq. 4.8 and the fit is shown in Fig. 4.29.

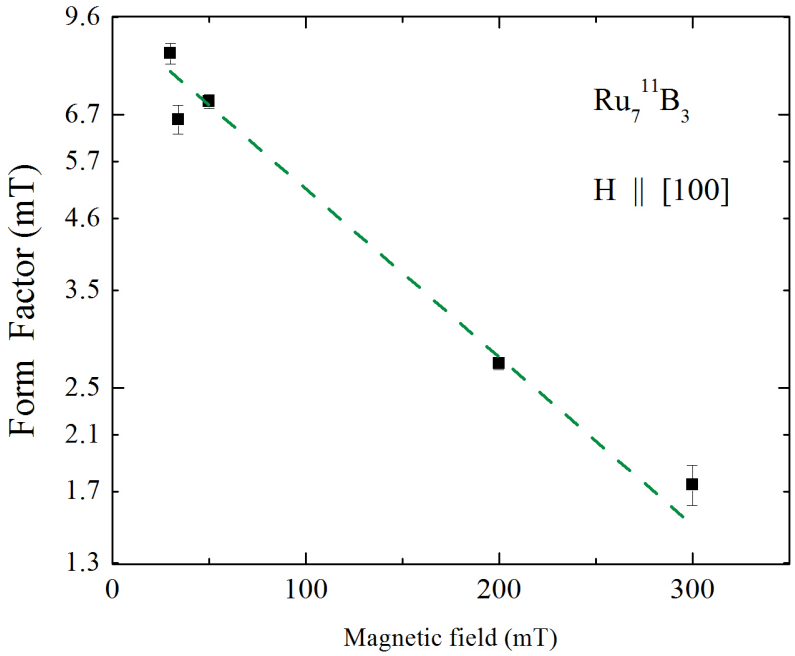

Figure 4.29: Magnetic field dependence of the form factor (F_{hk}) derived using the neutron reflectivity at $T = 1.6$ K and Eq. 4.7. SANS experiments were carried out with the [100] direction of $Ru_7{}^{11}B_3$ crystal parallel to the neutron beam and magnetic field directions. The dashed line is a linear fit to the data. See the text for details.

4.5 Conclusions

Muon spectroscopy and small-angle neutron scattering studies were performed to study the non-centrosymmetric superconductor Ru_7B_3, a member of 7:3 family of compounds with Th_7Fe_3-structure.

μSR experiments, carried out in the absence of a magnetic field on a polycrystalline sample, as well as single crystal, give evidence that time-reversal symmetry is broken in superconducting Ru_7B_3, so Ru_7B_3 is an unconventional superconductor. Muon spin rotation measurements on polycrystalline Ru_7B_3 gives evidence that multigaps exists in Ru_7B_3, but no further evidence of this was found for single crystal. Also the unusual time evolution of muon asymmetry spectra observed using transverse field muon spectroscopy suggests a non-hexagonal or anisotropic flux line lattice in

Ru_7B_3. Further small angle neutron scattering experiments, which are a direct probe of the FLL revealed a distorted hexagonal lattice for the [001] and [100] directions of $Ru_7{}^{11}B_3$ single crystal. But only extremely weak anisotropy, if any, was observed for a SANS pattern measured for [100] direction of the crystal rotated away from neutron beam directions and no evidence of anisotropy was observed for [001] direction of the crystal rotated away from the neutron beam direction. An origin of unusual behaviour of μSR spectra was not resolved.

The presence of a second domain and its reorientation may be further evidence of the existence of two different bands at the Fermi surface or existence of even more exotic states in superconducting Ru_7B_3. Further studies of Ru_7B_3 flux line lattice in higher magnetic fields, and in the vicinity of H_{c2}, would be required to further understand the FLL behaviour in unconventional superconductor Ru_7B_3.

Chapter 5

Studies of the non-centrosymmetric unconventional superconductor α-BiPd

5.1 Chapter outline

The previous chapter describes studies of the NCS superconductor Ru_7B_3 and presents evidence for unconventional superconductivity in Ru_7B_3. Another superconductor with non-centrosymmetric structure, α-BiPd was investigated. TF-μSR experiments were performed to examine the FLL of α-BiPd. The superfluid density of α-BiPd was studied and evidence of the presence of two superconducting gaps was found. ZF-μSR measurements were carried out to investigate TRS for the superconducting state of α-BiPd. Additionally, magnetic measurements were performed to study the upper critical field of the superconducting α-BiPd.

5.2 Superconductivity in α-BiPd

α-BiPd crystallises in a non-centrosymmetric, monoclinic structure with a space group $P2_1$ [162, 163] (see Fig. 5.1). Superconductivity in α-BiPd was first reported by Zhuravlev in his work on Bi-Pd systems [164], and subsequently, a more detailed description of this material was given by Joshi *et al.* [165]. According to their report,

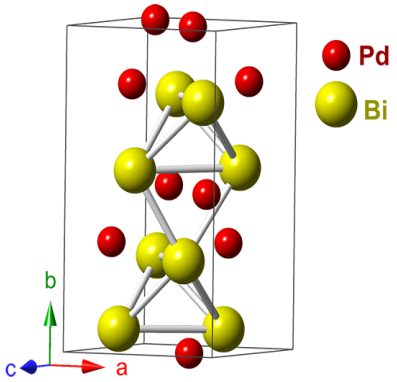

Figure 5.1: The structure of α-BiPd. Taken from [166].

T_c of the material is 3.87 K. H_{c2} was deduced from resistance measurements using the Helfand and Werthamer theory for a clean type II superconductor. The reported H_{c2} of 0.69 T, gives $\xi_{GL}(0) = 218$ Å and $\lambda_{GL} = 523$ Å. The thermodynamic critical field $H_c = 2.05$ T was found and H_{c1} of 0.0516 T was calculated [165].

Mondal *et al.* [167] carried out point contact Andreev reflection measurements and suggested that α-BiPd has an unconventional order parameter. They carried out the measurements by injecting a current (I) either along b for the [010] or perpendicular to b for the [001] directions of α-BiPd single crystal. For I $\parallel$ b, they observed two superconducting gaps with energies $\Delta_1 \sim 0.4 \pm 0.1$ meV and $\Delta_2 \sim 0.1 \pm 0.05$ meV and the fraction of the smaller gap was $w \sim 0.2$-0.6. For I $\perp$ b they observed the same Δ_1 and a different gap Δ_3 $\sim 0.8 \pm 0.15$ meV, with $w \sim 0.1$-0.35 meV. They suggested that two bands, Δ_- and anisotropic Δ_+ exists at the Fermi surface. The gap Δ_1 observed for both measured directions corresponds to Δ_- and the gaps Δ_2 and Δ_3 correspond

to Δ_+. Mondal *et al.* also reported a presence of Andreev bound states for both measured directions, which they concluded is evidence for mixing of spin-singlet and spin-triplet states in α-BiPd.

Recently, Jiao *et al.* studied α-BiPd using tunnel diode oscillator technique [166]. Anisotropy was suggested for in-plane (λ_{ac}) and interplane (λ_b) London penetration depths and evidence for two-bands was presented. In a convention used by Jiao *et al.*, the crystal is NCS along b direction. Jiao *et al.* suggested a presence of a mixture of spin-singlet and spin-triplet pairing in α-BiPd. λ_{ac}(T) agrees well with the BCS model, but the temperature dependence of λ_b suggest the presence of the mulitband superconductivity and the analysis of the superfluid density behaviour leads Jiao *et al.* to the conclusion that two BCS bands with anisotropic gaps are present in α-BiPd [166].

5.3 Preparation of Polycrystalline α-BiPd

Polycrystaline α-BiPd was prepared by Dr. Ravi P. Singh. α-BiPd sample was prepared by heating of Bi, 99.999 % , and Pd, 99.99 % in a boron nitride crucible with a pointed bottom, which was sealed under a vacuum in a quartz tube. The sealed tube was initially heated slowly ($\sim$ 35°C/h) to 650°C. At 650°C it was kept for 12 h and afterwards, it was slow cooled to 595°C at a rate of 1°C/h. Afterwards, it was kept for 20 h in a furnace (in 595°C) and finally the furnace was switched off. A high-quality polycrystalline samples along with few mm size single crystals was obtained.

5.4 Magnetic and transport measurements

The polycrystalline sample was characterized by magnetic, transport and specific heat measurements and afterwards μSR experiments were performed. The magnetic properties of α-BiPd were examined using the MPMS magnetometer with SQUID

(Quantum Design). An approximately spherical sample was used, hence well defined demagnetization corrections could be applied. Measurements were carried out in the ZFC conditions on warming and the FC conditions on cooling in a range of the applied magnetic fields. Transport properties were investigated using the four probe technique in commercial PPMS (Quantum Design) and measurements were performed with and without the applied magnetic field using a rectangular bar sample with silver wires attached with silver paint. A relaxation method was used for the specific heat measurement carried out using the PPMS (Quantum Design).

The measurements of dc magnetic susceptibility were carried out in the ZFC condition and in a low applied magnetic field, $H = 20$ Oe (see Fig. 5.2(a)) and show a superconducting transition at $T_{c_{mag}} = 3.7$ K with a transition width $\Delta T \sim 0.1$ K. The transport measurements in zero magnetic field (see Fig. 5.2(b)) show a sharp drop of the resistivity, at a well defined critical temperature, $T_{c_{res}} = 3.8$ K. A peak in the specific heat measurements in zero magnetic field (see Fig. 5.2(c)) is present at $T_{c_{hc}} = 3.75$ K with $\Delta_T = 0.05$ K, which agrees with the T_c already established using the magnetic and transport measurements and is in good agreement with the previously published results [164, 165].

To determine a value of the lower critical field $H_{c1}(0)$ for α-BiPd, magnetization was measured as a function of magnetic field at various temperatures. $H_{c1}(T)$ was determined for each temperature (see Fig. 5.3(a)) as the magnetic field, at which $M(H)$ curves deviates from linearity. The lower critical field of α-BiPd $H_{c1}(0) = (122 \pm 3)$ Oe, was established from fitting with:

$$H_{c1}(T) = H_{c1}(0)[1 - (T/T_c)^2] \tag{5.1}$$

Our lower critical field value is lower than the value measured by Joshi *et al.* but it agrees with the value of H_{c1} calculated by them [165].

The magnetic and transport measurements were performed to determine the

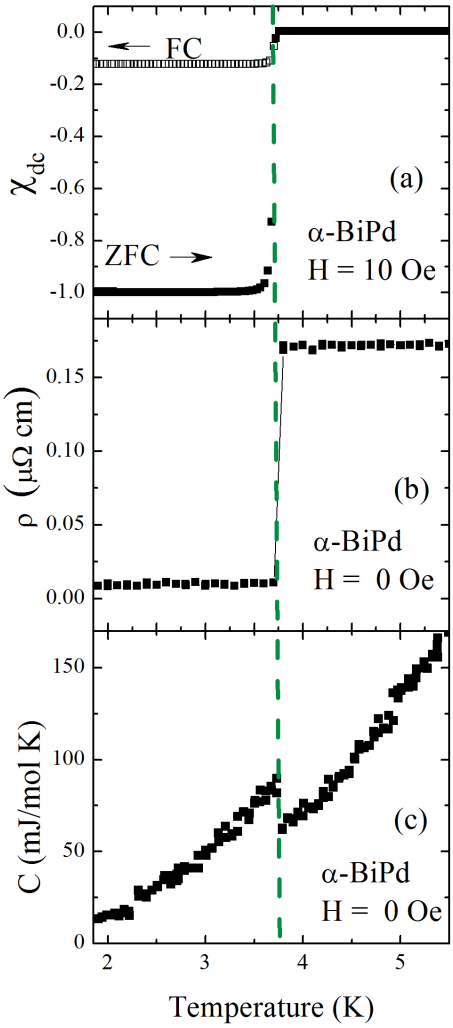

Figure 5.2: (a) Temperature dependence of the magnetic susceptibility (χ_{dc}) of α-BiPd in a low magnetic field, $H = 20$ Oe. was measured in the ZFC conditions on warming and the FC conditions on cooling. (b) Temperature dependence of the resistivity (ρ) of α-BiPd measured without the applied magnetic field. The line is a guide to the eye. (c) Temperature dependence of the specific heat (C) of α-BiPd measured in zero magnetic field. The critical temperatures established by the presented techniques are in good agreement and they are marked by the green, dashed line.

upper critical field H_{c2} for α-BiPd (see Fig. 5.3(b)). The value of H_{c2} was found to depend strongly on the measurement technique and the way of interpreting the data. From the magnetic measurements, T_c was defined as the temperature below which the sample became superconducting (see Fig. 5.3(b), marked by hollowed

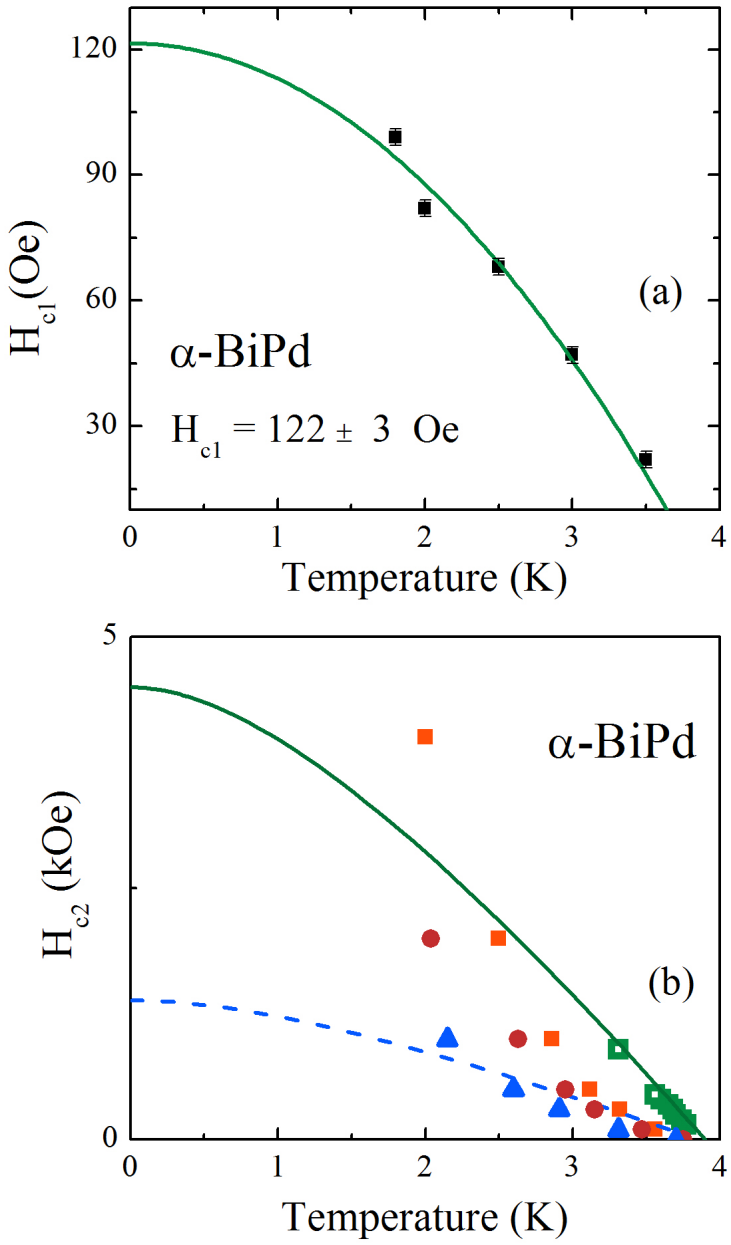

Figure 5.3: (a) Temperature dependence of the lower critical field, H_{c1} for α-BiPd. (b) Temperature dependence of the upper critical field, H_{c2} for α-BiPd. The line are a fit to the data with the WHH model. Presented values were obtained using the resistivity (filled symbols) and magnetic susceptibility measurements (hollow symbols). From the transport measurements, T_c was defined as the temperature of onset of superconductivity (orange squares), mid-point of resistivity (red circles) and zero-resistance (blue triangles). See the text for details.

green squares). The obtained data were fitted using the WHH model [56, 57], giving a H_{c2} value of 4497 Oe (marked by the solid, green line in Fig. 5.3(b)). From the transport measurements, 3 different estimations of T_c were made: T_c was defined as the temperature of onset of superconductivity, mid-point of resistivity and zero-resistance (see Fig. 5.3(b), marked by orange squares, red circles and blue triangles, respectively). The three datasets do not follow the WHH model. Forcing the WHH fit to the zero-resistance data (see dashed, blue line on Fig. 5.3) the value of $H_{c2} = 1387$ Oe was obtained. However the datasets from the mid-point and onset of superconductivity would suggest much higher value of H_{c2} than the value established from the magnetic measurements (see inset of Fig. 5.3(b)).

5.5 μSR studies of α-BiPd

The muon spin rotation and relaxation experiments were performed using the MuSR instrument in ISIS facility, Rutherford Appleton Laboratory, United Kingdom. The powder sample was mounted with GE varnish on a silver plate and covered by a thin silver foil. The sample was cooled in a dilution refrigerator, allowing for temperatures as low as 55 mK. For the ZF-μSR experiments the sample was cooled in zero field to the base temperature and then measurements were performed in zero field.

5.5.1 Muon Spin Relaxation

The muon spin relaxation experiment was performed in order to investigate whether α-BiPd exhibited TRS breaking. TRS is broken in a superconductor if in zero magnetic field, a small spontaneous magnetic field appears. The ZF-μSR measurements were performed in the superconducting (see spectra at $T = 0.1$ K in Fig. 5.4) and normal (see spectra at $T = 0.1$ K in Fig. 5.4) states of α-BiPd. The spectra shown in the Fig. 5.4 are described well using the function with Kubo - Toyabe depolarisation (see Eq. 3.10 and the fitted parameters in Table 5.1).

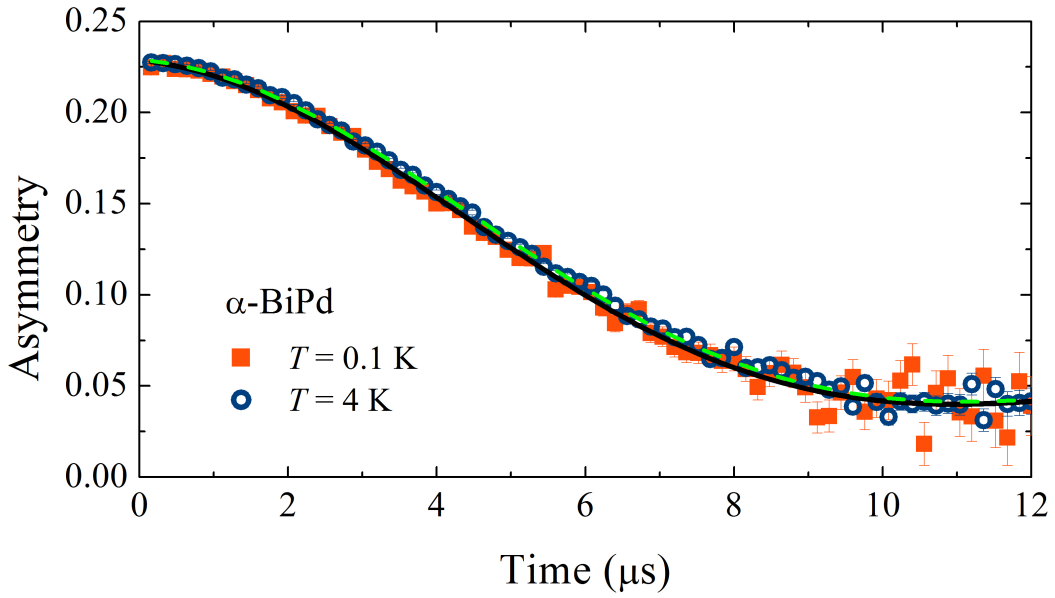

Figure 5.4: Time dependence of the muon asymmetry for α-BiPd. Measurements were carried out in zero field, at 0.1 K in the superconducting state of α-BiPd (orange squares) and at 4 K in the normal state of α-BiPd (blue circles). Lines are the fit to the data with Eq. 3.10. The solid line is a fit to the data obtained at 0.1 K and the dashed line – at 4 K.

No difference between the muon asymmetry spectra measured in the superconducting and normal state was observed (see Fig. 5.4), therefore no additional magnetic field, on top of the signal from the nuclear moments, was detected. Hence, no evidence of time reversal symmetry breaking in α-BiPd was observed within the limits of μSR measurements.

T (K)	A_0	Δ_{KT} (μs^{-1})	Λ (μs^{-1})	A_{bcg}
0.1	0.194 ± 0.001	0.158 ± 0.001	0.013 ± 0.002	0.034 ± 0.001
4	0.194 ± 0.001	0.156 ± 0.001	0.012 ± 0.002	0.036 ± 0.001

Table 5.1: Parameters of the fit with Eq. 3.10 to ZF-μSR spectra for the polycrystalline α-BiPd (see Fig. 5.4).

5.5.2 Muon Spin Rotation

Our muon spin rotation experiments were carried out in transverse field geometry with the magnetic field applied perpendicular to the muon beam polarization. Positrons from the muon decay were detected using a set of 64 detectors, which later were grouped by software to two orthogonal, virtual detectors. The TF-μSR measurements were carried out in the field-cooled conditions, so the sample was cooled in an applied magnetic field from the normal state to the base temperature and then the measurements were carried out during warming.

The time evolution of asymmetry of the muon polarization of α-BiPd measured for the sample at the temperature below and above the superconducting transition ($T_{\rm c}\sim$3.75) is shown in Fig. 5.5(a) (spectra at 0.1 K) and Fig. 5.5(b) (spectra at 3.9 K). For a sample in the superconducting state (see Fig. 5.5(a)), magnetic field penetrates the material, muons interact with different magnetic fields which causes the continuous dephasing of the detected asymmetry signal [8]. Fig. 5.5(b) shows the muon polarisation when α-BiPd is in the normal state and only the contribution from the nuclear moments is present. The time evolution of the asymmetry of muon polarisation (see Fig. 5.5) is described well using a function which consists of sinusoidal oscillations with Gaussian relaxation (Eq. 3.12). The TF-μSR spectra from two virtual orthogonal detectors were fitted simultaneously with Eq. 3.12. The temperature dependences of the muon depolarisation rate (σ) and the internal magnetic field (B) were obtain (see Fig. 5.6) and nature of the superconducting ground state of α-BiPd was studied. For the measurements in $H = 400$ Oe, interesting behaviour was found. In $H = 400$ Oe, $T_{\rm t1} = 2.1$ K is a cut-off value for the region of rapid decrease of the depolarisation rate (see Fig. 5.6) and usually would be seen as the value of $T_{\rm c}$, although a weak superconducting contribution was still detected below $T_{\rm t2} = 3.1$ K. Above $T_{\rm t2}$ clearly, only the contribution from the nuclear moments is present.

The muon depolarisation rate σ includes the superconducting (σ_{sc}) and

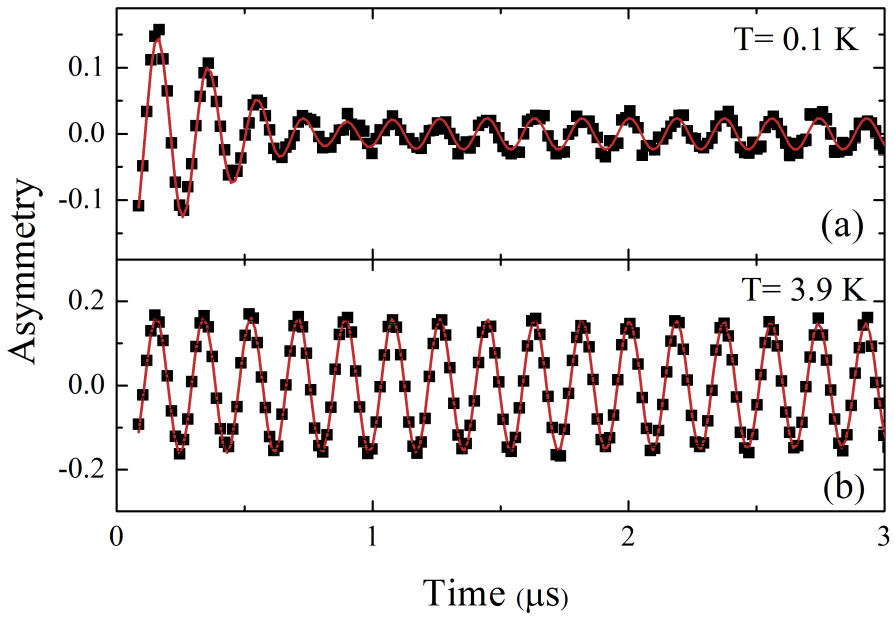

Figure 5.5: The time evolution of the asymmetry of muon polarisation in the superconducting ($T = 0.1$ K) and normal states ($T = 3.9$ K) of α-BiPd in the applied magnetic field, $H = 400$ Oe. Function, which include sinusoidal oscillations with Gaussian relaxation (see Eq. 3.12) was fitted to the data (red curve). Two datasets, from the two virtual orthogonal detectors were obtained and fitted simultaneously. Only one dataset is shown for clarity of presentation.

nuclear contribution (σ_n) and $\sigma^2 = \sigma_{sc}^2 + \sigma_n^2$. σ_n was constant during our measurements and was determined from the measurements above T_c. Fig. 5.7 shows the field dependence of σ_{sc} at $T = 0.1$ K. The significant field dependence of σ_{sc} provides further evidence that the upper critical field H_{c2} is low. Values of $H_{c2}(0.1\text{ K}) = 737$ Oe and $\lambda(0.1\text{ K}) = 118$ nm were obtained from fitting with Eq. 3.15. The magnetic penetration depth λ was calculated using Eq. 3.15 and values of $B_c(T)$ from magnetic measurements. λ provides information about the superfluid density, hence the superconducting order parameter can be determined. The London model describes the relation between λ and the superconducting gap δ as [154, 155]:

$$\frac{\lambda^{-2}(T,\Delta_{0,i})}{\lambda^{-2}(0,\Delta_{0,i})} = 1 + \frac{1}{\pi}\int_0^{2\pi}\int_{\Delta(T,\varphi)}^{\infty}\left(\frac{\partial f}{\partial E}\right)\frac{E\ \mathrm{d}E\mathrm{d}\Phi}{\sqrt{E^2-\Delta_i(T,\varphi)^2}} \tag{5.2}$$

where $f = [1+\exp(E/k_BT)]^{-1}$ is the Fermi function, φ is the angle along the

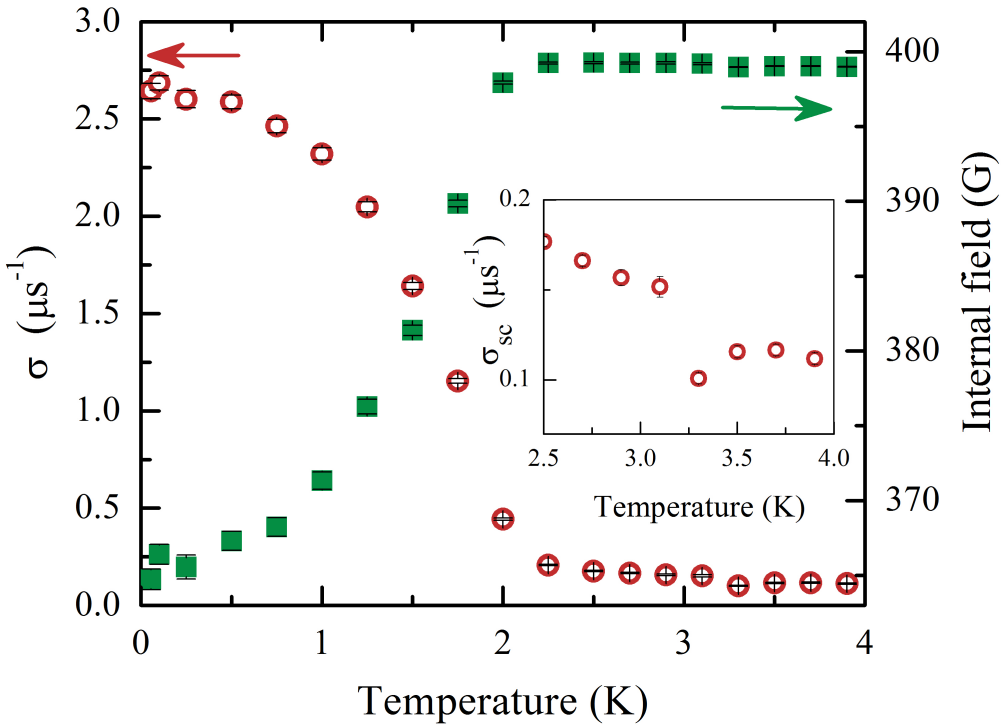

Figure 5.6: Temperature dependence of the muon depolarisation rate σ (empty red circles) and the internal magnetic field (filled green squares) for α-BiPd. Inset: The temperature dependence of σ in the temperature region, where a 'superconducting tail' was observed (see text for detail).

Fermi surface , index $i = 1$ or 2 denotes the respective superconducting gaps and $\Delta_i(T,\varphi) = \Delta_{0,i}\delta(T/T_c)g(\varphi)$, where $\delta(T/T_c) = \tanh\{1.82[1.018(T_c/T-1)]^{0.51}\}$ is the temperature dependence of a superconducting gap in the BCS theory. The angular dependence of the gap $g(\varphi)$ is 1 for an s-wave or s+s wave gap but is different for unconventional order parameters, e.g. $|\cos(2\varphi)|$ for a d-wave gap. The temperature dependence of the magnetic penetration depth $\lambda(T)$ can be described using Eq. 5.3:

$$\frac{\lambda^{-2}(T)}{\lambda^{-2}(0)} = \omega_1 \frac{\lambda^{-2}(T,\Delta_{0,1})}{\lambda^{-2}(0,\Delta_{0,1})} + \omega_2 \frac{\lambda^{-2}(T,\Delta_{0,2})}{\lambda^{-2}(0,\Delta_{0,2})} \tag{5.3}$$

where ω_1, ω_2 shows the contribution of each gap to $\lambda(T)$ and $\omega_1 + \omega_2 = 1$. The Eq. 5.3 can be adapted for a presence of single or multiple superconducting gaps and the estimation of the size and the superconducting order parameter is also possible.

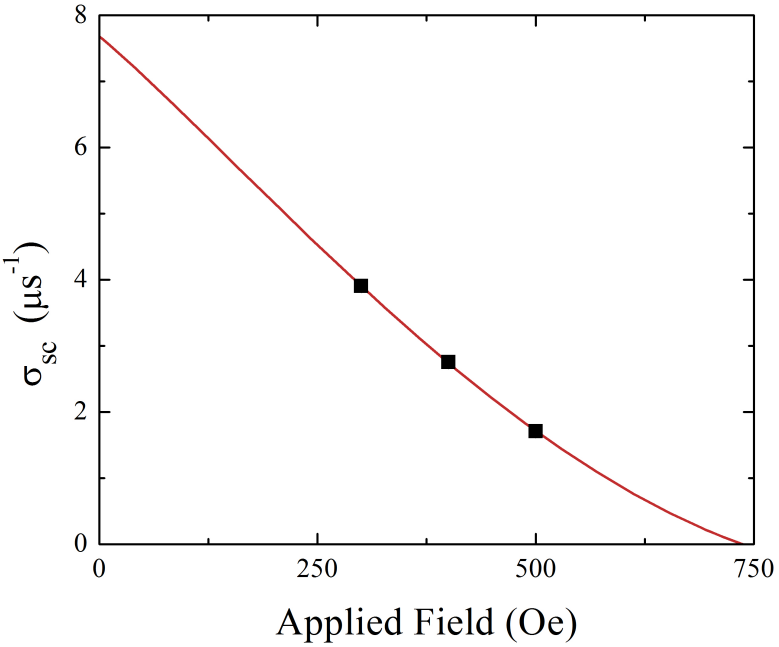

Figure 5.7: Field dependence of the superconducting contribution to the muon depolarisation rate σ_{sc} for α-BiPd at 0.1 K. The line is a fit to the data with Eq. 3.15.

λ^{-2}(T) for α-BiPd was derived from σ(T) using Eq.3.15. The temperature dependence of λ^{-2} was fitted with Eq. 5.3 (see Fig. 5.8). A presence of one or multiple superconducting gaps was considered, also existence of various superconducting order parameters (i.e. s-wave and d-wave) was considered (see Fig. 5.8). The residual plots for models with one superconducting gap, either s-wave or d-wave (see Fig. 5.8(b)) show that those models largely deviates from the experimental data. Hence the model with only one gap does not describe the temperature dependence of λ^{-2} for α-BiPd. For models with two s-wave gaps or two, s- and d-wave, gaps residuals are significantly closer to zero and randomly distributed, so those models represents good fits to the data. Temperature dependence of the magnetic penetration depth and model described with Eq. 5.3 gives evidence that either two s-wave gaps with $\Delta_{1,\mathrm{s}} = 0.46 \pm 0.03$ meV, $\Delta_{2,\mathrm{s}} = 0.20 \pm 0.05$ meV and $\omega_1 = 0.83 \pm 0.09$ are present in α-BiPd or the s- and d-wave gaps with energies $\Delta_{1,\mathrm{s}} = 0.38 \pm 0.02$ meV and $\Delta_{2,\mathrm{d}} = 0.8 \pm 0.2$ meV, respectively, and $\omega_1 = 0.65 \pm 0.06$ exist in α-BiPd.

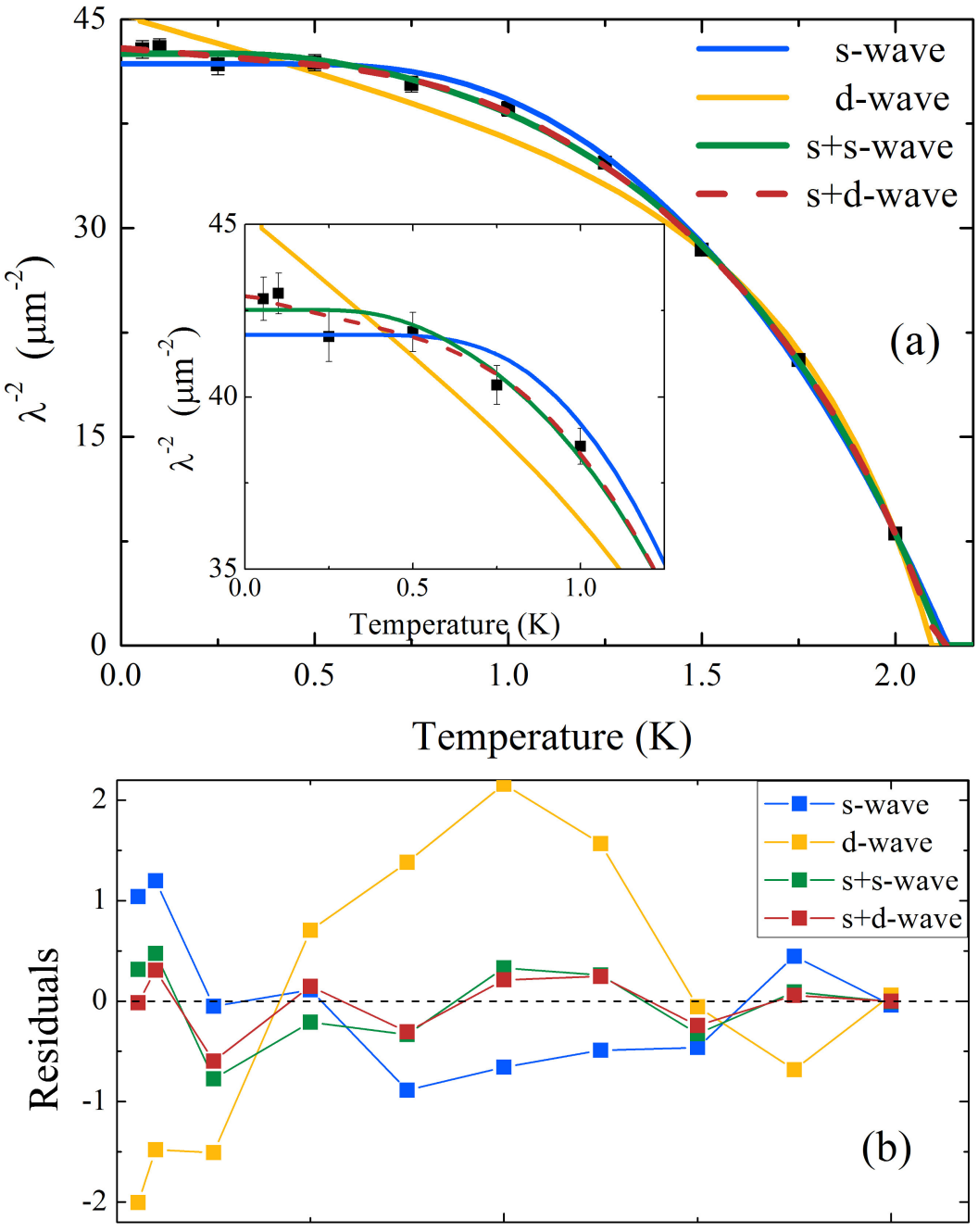

Figure 5.8: Temperature dependence of the magnetic penetration depth of α-BiPd in the applied magnetic field of 400 Oe. The lines are fits with Eq. 5.3, for two s-wave gaps (green line), single s-wave gap (blue line) and two gaps, where one is d-wave and another one is s-wave gap (red line). Inset of the graph shows the temperature range where significant deviations between fitted models appeared.

5.6 Conclusions

Muon spectroscopy, magnetic and transport measurements were performed to examine the properties of the non-centrosymmetric superconductor α-BiPd. Our TF-μSR measurements gives evidence that two superconducting gaps exist in α-BiPd, either two s-wave gaps or an s-wave and d-wave gaps are present in α-BiPd.

Our lower critical field value H_{c1}= 122 Oe, is much lower than the value measured by Joshi *et al.* [165] but it is in agreement with the value of H_{c1} they calculated. Our TF-μSR measurements suggest that α-BiPd is in the mixed state in magnetic fields much lower than the value measured by Joshi *et al.* An unusual behaviour of upper critical field of α-BiPd was observed and the H_{c2} estimated from different techniques did not give consistent results. This may require further study.

No evidence of time reversal symmetry breaking in α-BiPd was observed using the muon spin relaxation experiment in zero field. Our muon spin rotation experiments indicate that α-BiPd is multiband superconductor. The μSR measurements suggest the presence of either two s-wave gaps or s- and d-wave gaps in α-BiPd. Either two s-wave gaps with energies $\Delta_{1,s} = 0.46 \pm 0.03$ meV, $\Delta_{2,s} = 0.20 \pm 0.05$ meV and $\omega_1 = 0.83 \pm 0.09$ exist in α-BiPd or the s- and d-wave gaps with energies $\Delta_{1,s} = 0.38 \pm 0.02$ meV and $\Delta_{2,d} = 0.8 \pm 0.2$ meV, respectively, and $\omega_1 = 0.65 \pm 0.06$ are present in α-BiPd.

Chapter 6

Studies of the Heusler family members, superconducting compounds $ZrNi_2Ga$ and $NbNi_2Ga$

6.1 Chapter overview

Compounds which belong to the Heusler family are multifunctional materials, which attract attention due to their tunable electronic structure [168]. Of the Heusler family, superconducting $ZrNi_2Ga$ (T_c = 2.9 K [169]) and $NbNi_2Ga$ (T_c = 1.54 K [170]) are also of interest because elemental Ni is ferromagnetic, and yet no long range magnetic order has been found for $ZrNi_2Ga$ or $NbNi_2Ga$. To further understand the superconducting properties of the Heusler compounds, we performed muon spectroscopy measurements using the MuSR muon spectrometer in ISIS facility. We studied the flux line lattices of $ZrNi_2Ga$ and $NbNi_2Ga$ in the mixed state using muon spin rotation and muon spin relaxation techniques. A part of this work is in preparation for a publication and can be found in [171].

6.2 Overview of the Heusler compounds

In 1903 Fritz Heusler studied the properties of Cu_2MnAl and found it to be ferromagnetic, despite the fact that none of the constituent elements are magnetic by themselves [168]. However, Heusler compounds only gained wider attention in the 1980s. Nowadays more than 1000 compounds constitute the Heusler family, among which ternary non-centrosymmetric intermetallic compounds with stoichiometry 1:1:1 are known as half-Heusler compounds, and materials with 2:1:1 stoichiometry are Heusler compounds. Heusler compounds crystallise in the Cu_2MnAl-structure, with space group $Fm\bar{3}m$, which contains four interpenetrating *fcc* lattices. Some Heusler compounds crystallize with a $CuHg_2Ti$-structure, a so called inverse Heusler structure, with a space group $F\bar{4}3m$. Quaternary Heusler compounds have an LiMgPdSn-structure.

Due to their extremely versatile electronic structure, several different physical properties can be present in a single Heusler compound [168]. The Heusler compounds are combinations of several elements, but for many of them, their properties can be identified based solely upon the number of their valence electrons. Figure 6.1 presents various phenomena which exist in compounds from the Heusler family. Tunable properties of Heusler compounds make them outstandingly novel materials for electronics. For example the energy gap in Heusler semiconductors can be tuned by changing the constituent elements, which results in a wide range of possible energy gaps - a feature desirable in solar cell technology, thermoelectric and other energy applications. Heusler compounds have already had various industrial applications, mainly for magnetic recording, magnetic sensors or new materials for semiconductor spin injection devices. Their thermoelectric properties place them among recognized materials for thermoelectric elements and thermoelectric converters. More information about Heusler family compounds can be found for example in a recent review article by Graf *et al.* [168].

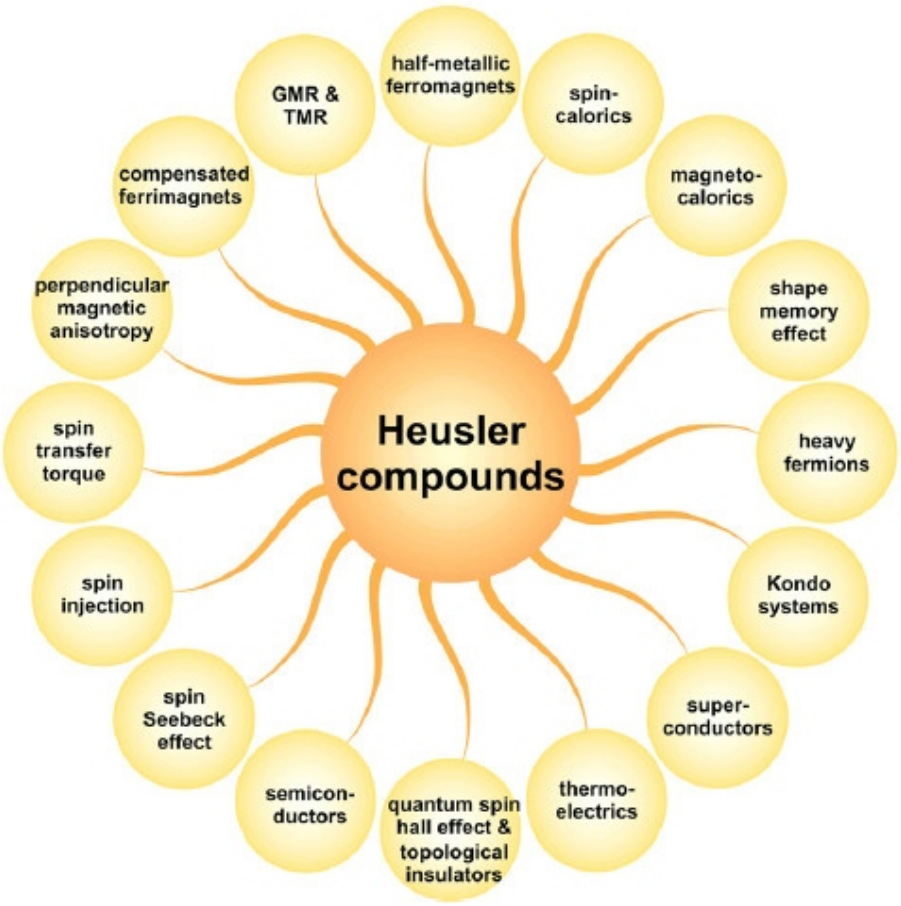

Figure 6.1: Phenomena present in compounds belonging to the Heusler family. Taken from [168].

6.3 Superconductivity in the Heusler family

Several compounds from Heusler family are found to be superconducting. In particular, non-magnetic 2:1:1 compounds with 27 valence electrons are superconducting [168]. Presence of the van Hove singularity close to Fermi energy also encourages superconducting behaviour in Heusler compounds. So far the highest T_c among the Heusler compounds was observed for Pd_2SnY, which is superconducting below $T_c = 4.9$ K [172]. Also relatively high superconducting transition temperatures were found in Pd_2ZrAl and Pd_2HfAl, T_c of 3.2 K and 3.4 K, respectively [173]. Ni_2NbSb is superconducting below $T_c = 3.4$ K and when Nb is substituted with

Ti (which has significantly different mass than Nb) or Ta (which introduces more valence electrons), T_c decreases and the strength of an the electron-phonon coupling is also reduced [174]. Wernick *et al.* studied various Heusler compounds using ac susceptibility. They discovered that Au_2InY is superconducting below $T_c = 1.74$ K and a partial substitution of Pd, in the place of Au, initially rises the transition temperature, up to $T_c = 2.68$ K for $Au_{1.3}Pd_{0.7}InY$, whilst a further addition of Pd causes a reduction of T_c, to become as low as $T_c = 1.07$ for Pd_2InY [172]. On the other hand, substitution of Er in superconducting $ErPd_2Sn$ by other rare earth elements, i.e. $(Er_{1-x}Y_x)Pd_2Sn$, causes a linear increase of T_c from $T_c = 1.17$ K in $ErPd_2Sn$ to $T_c \approx 5.2$ K in YPd_2Sn [175].

Among the half-Heusler compounds, so far only LaPtBi has been found to be superconducting below $T_c = 0.9$ K. Several other Heusler compounds are also superconducting and some examples are gathered in Table 6.1. Furthermore, coexistence of superconductivity and long range magnetic order was observed in $ErPd_2Sn$ [175] and Pd_2YbSn [176]. Nickel, which is ferromagnetic itself, can be found in a few superconducting Heusler family compounds, i.e. $ZrNi_2Ga$ and $NbNi_2Ga$ [169, 170] but no magnetic order was observed in those materials.

	T_c	
$YbPd_2Sn$	2.46 K	[168]
$ErPd_2Sn$	4.9 K	[168]
Ni_2HfAl	0.74 K	[172]
Ni_2ZrAl	1.38 K	[172]
Ni_2HfGa	1.12 K	[172]
$TmPd_2Sn$		[177]
$LuPd_2Sn$		[177]
Ni_2NbAl	2.15 K	[170]
Ni_2NbSn	2.9 K	[170]

Table 6.1: Selected superconducting Heusler compounds.

6.3.1 Properties of $ZrNi_2Ga$

A member of the Heusler family, $ZrNi_2Ga$ crystallises in a cubic structure with a lattice constant a = 6.103 Å [178] and an $Fm\overline{3}m$ space group [169]. The crystal structure of $ZrNi_2Ga$ is shown in Fig. 6.2.

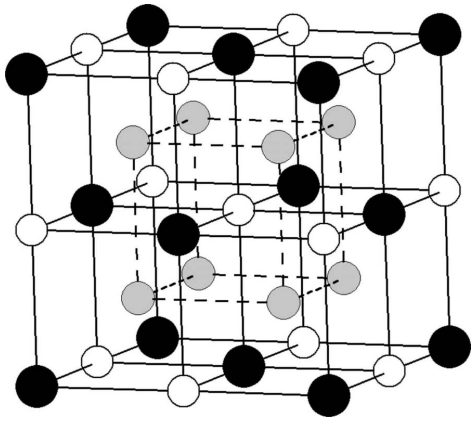

Figure 6.2: The crystal structure of $ZrNi_2Ga$. The black spheres represents zirconium atoms, nickiel atoms are grey and gallium atoms – white. Taken from [169].

$ZrNi_2Ga$ has a van Hove singularity close to the Fermi energy [177] and has 27 valence electrons, hence is superconducting below $T_c = 2.9$ K, which is a relatively high T_c among the other Ni-based Heusler compounds [169]. Winterlik *et al.* carried out density of states calculations, as well as magnetic, transport and specific heat measurements. The upper critical field of $ZrNi_2Ga$ is $H_{c2} = 1.5$ T, the value being obtained from data acquired using transport and specific heat measurements and fitted with the WHH model. Based upon specific heat measurements, Winterlik *et al.* found an isotropic energy gap in $ZrNi_2Ga$ and $\Delta(0) = 0.434$ meV, which they concluded is in good agreement with the weak coupling BCS model [169]. Additionally, using the isotropic Gizburg-Landau-Abrikosov-Gor'kov theory, the coherence length of $ZrNi_2Ga$ was found to be $\xi = 15$ nm and $\lambda_{G-L} = 350$ nm [169]. Winterlik *et al.* used their specific heat measurements and the McMillan formula to find $\lambda_{el-ph} = 0.551$. The electron phonon-coupling constant calculated by Ming *et al.* [177] was $\lambda_{el-ph} = 0.747$, which suggests the presence of much stronger electron-phonon interactions than

suggested by Winterlik *et al.* [169].

Ming *et al.* [177] based upon their *ab initio* density functional theory calculations show that $ZrNi_2Ga$ is a conventional phonon-mediated superconductor. Winterlik *et al.* [169] also concluded that $ZrNi_2Ga$ is a conventional s-wave superconductor, well described by the BCS-theory.

6.3.2 Properties of $NbNi_2Ga$

$NbNi_2Ga$, which has 27 valence electrons, crystallises in a cubic $Fm\overline{3}m$ structure with a lattice constant a = 5.958 Å [179] and also belongs to the Heusler family compounds. Waki *et al.* measured the electrical resistance of $NbNi_2X$ compounds and found that $NbNi_2Ga$ is superconducting below T_c = 1.54 K [170]. Using specific heat measurements and the McMillan formula, the electron-phonon coupling strenght λ_{el-ph} = 0.5 was calculated and Waki *et al.* reported that $NbNi_2Ga$ is an intermediate coupled superconductor. Waki *et al.* also calculated λ_{el-ph} for a few other $NbNi_2X$, where X = (Al, Ga, Sn), and concluded they were intermediate-coupled superconductors. $H_{c2}(0)$ for $NbNi_2Ga$ was extrapolated from only a few data points and the reported value was $H_{c2}(0)$ = 6.3 kOe [170] (see Fig. 6.3).

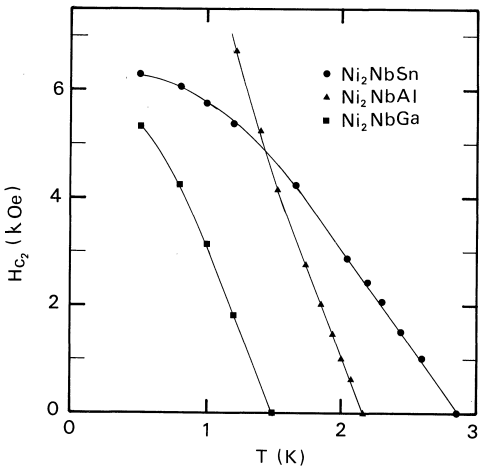

Figure 6.3: Temperature dependence of H_{c2} for a few Heusler compounds. Filled square symbols (■) represent data for $NbNi_2Ga$. Adapted from [170].

6.4 μSR studies of $ZrNi_2Ga$

To study the superconducting properties of $ZrNi_2Ga$, muon spectroscopy experiments in ZF and TF - modes were performed using the MuSR instrument in ISIS facility, Rutherford Appleton Laboratory, United Kingdom. The principles of the μSR techniques are described in Section 3.4. For the μSR experiments a polycrystalline sample was powdered and mounted on a silver plate with diluted GE varnish and covered by a silver foil. The sample was inserted into a dilution fridge and the measurements were performed.

6.4.1 TF-μSR studies of $ZrNi_2Ga$

TF-μSR measurements were carried out in field-cooled conditions for a range of temperatures and applied magnetic fields to investigate the FLL of $ZrNi_2Ga$. In a constant magnetic field, several measurements were carried out for $ZrNi_2Ga$ in the superconducting state, over a range of temperatures – from the cryostat base temperature ($\sim$0.06 K) up to 3 K. The data acquired from the 64 detectors were grouped in two orthogonal, virtual detectors and spectra were fitted simultaneously with Eq. 6.1. μSR spectra is well described by equation (Eq. 6.1), which contains sinusoidal oscillations with Gaussian relaxation:

$$G_x(t) = \sum_{i=1}^{2} A_i \exp\left(-\frac{\sigma_i^2 t^2}{2}\right) \cos\left(\omega_i t + \varphi\right) \tag{6.1}$$

where A is the initial asymmetry, σ is the muon depolarisation rate, φ is the phase offset of the two virtual detectors, ω is the frequency of muon spin precession. In the equation, the term of the sum with index i = 2 describes the background contribution. The contribution from silver dominates the background signal so no relaxation is expected, hence σ_2=0. The background contribution was found to be negligible, which allows us to set it to zero in the data analysis. The fits with Eq. 6.1 to the data are shown in Fig. 6.4 for μSR spectra measured in an applied magnetic field

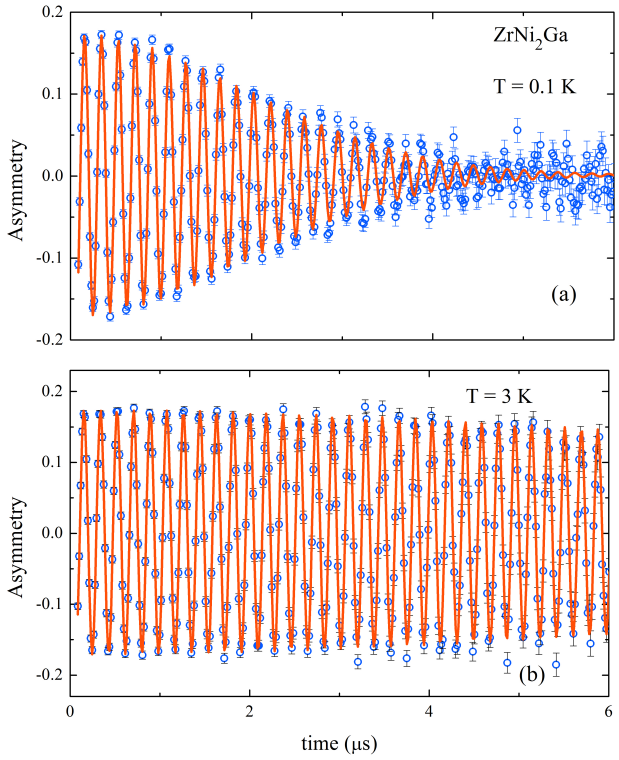

Figure 6.4: Time dependence of a muon spin asymmetry for $ZrNi_2Ga$ at (a) T= 0.1 K and (b) T= 3 K, when $ZrNi_2Ga$ in the superconducting and normal states, respectively. The measurements were performed in an applied magnetic field of 400 Oe. Two datasets were obtained from two virtual detectors. For a clarity of presentation, only one dataset is shown. The curves are fits to the data with a function containing sinusoidal oscillations with Gaussian relaxation (see Eq. 6.1).

of 400 Oe, in the superconducting and the normal states of $ZrNi_2Ga$, at T = 0.1 K and 3 K, respectively. In the superconducting state, due to the presence of the inhomogeneous field of the FLL, decaying oscillations were observed. For $ZrNi_2Ga$ in the normal state, muons were subjected to an uniform magnetic field hence no damping of the oscillations was present (see Fig. 6.4(b) for spectra at T = 3 K). Modelling with Eq. 6.1 provides information about the muon depolarization rate and the internal magnetic field. The temperature dependences of σ and internal magnetic field are shown in Figure 6.5. Measurements were taken in an applied magnetic field of 300 Oe (green triangles), 400 Oe (violet squares) and 600 Oe (orange circles).

Measured muon depolarisation rate is proportional to the superfluid density of

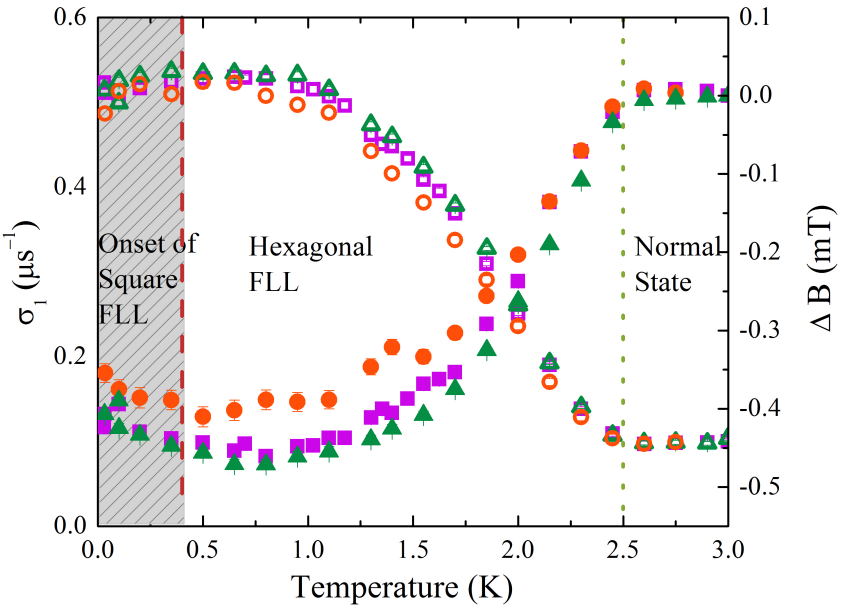

Figure 6.5: The temperature dependence of the depolarization rate, σ (hollow symbols) for $ZrNi_2Ga$ and the temperature dependence of the internal magnetic field, which was normalized to the applied magnetic field and $\Delta B = B_{mesured} - B_{applied}$ (filled symbols). The measurements were taken in the FC conditions, in an applied magnetic field of 300 Oe (green triangles), 400 Oe (violet squares) and 600 Oe (orange circles). The transition between the superconducting and normal states is marked with a dotted line. Also, regions where the square and hexagonal FLLs exist are marked on the graph. The grey shaded area of the graph marks a region where square FLL potentially appears.

$ZrNi_2Ga$. For a conventional BCS superconductor, well below T_c, changes of superfluid density are negligible. When the temperature increases above half-T_c up to T_c, the superfluid density rapidly decreases and saturates again above T_c, when the material is in the normal state. However, in $ZrNi_2Ga$ unusual σ behaviour was observed (see Figure 6.5). At low temperatures, the depolarisation rate slightly increases towards higher temperatures, only saturating above ~0.4 K. Little change in σ is observed up to ~1.2 K, then σ rapidly decreases when the temperature rises towards T_c. Above T_c σ remains constant so the T_c of $ZrNi_2Ga$ is around 2.5 K. This uncommon superfluid density behaviour at very low temperatures was observed for $ZrNi_2Ga$ in all measured magnetic fields (see Fig. 6.5) and is in agreement with the temperature evolution of an internal field distribution measured using TF-μSR

for $ZrNi_2Ga$. At low temperatures, the internal field distribution, instead of being constant, slightly decreases (see Fig. 6.5) to saturate above ∼0.4 K. Above ∼1.2 K, with increasing temperature, the internal magnetic field increases to saturate again above ∼2.5 K, when $ZrNi_2Ga$ is in the normal state. Above ∼2.5 K, the values of internal magnetic field does not change and are equal to the applied magnetic field value because in the normal state magnetic field homogeneously penetrates the sample. Hence, above T_c muons are effectively measuring the value of the applied magnetic field. This unusual temperature evolution of the superfluid density and the mean internal magnetic field of $ZrNi_2Ga$ might be evidence that a change in the FLL of $ZrNi_2Ga$ occurs in the low temperatures. Its origin was investigated in course of further analysis.

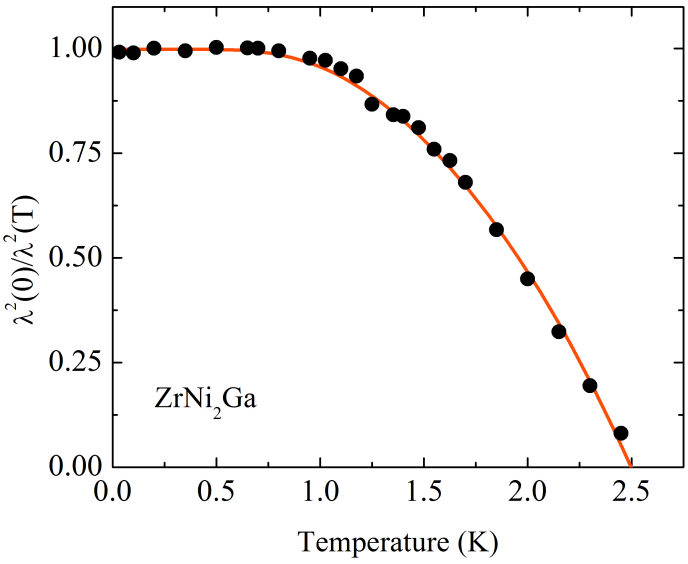

Figure 6.6: Temperature dependence of the magnetic penetration depth of $ZrNi_2Ga$. The μSR measurement were carried out in the applied magnetic field, H = 300 Oe. The data were normalized, for a clarity of presentation. The line is a fit to the data with Eq. 5.3, see details in the text.

The relation between σ_{sc} and a magnetic penetration depth (λ) is described with Equation 6.2, which can be adjusted accordingly for a square or hexagonal VL [114].

$$\sigma_{sc} = A(1-b)(1+1.21(1-\sqrt{b})^3)\lambda^{-2} \tag{6.2}$$

where b is the reduced field (b= B/ B_{c2}). Parameter A depends on a symmetry of the FLL, for a hexagonal FLL is $A = 4.83 * 10^4$ and $A = 5.07 * 10^4$ for a square vortex lattice. The temperature dependence of λ (shown in Fig. 6.6) was derived from σ_{sc}, assuming that a square FLL is present at the low temperatures (so in Eq. 6.2, $A = 5.07 * 10^4$) and a hexagonal FLL exists at higher temperatures (so $A = 4.83 * 10^4$ in Eq. 6.2). It was assumed that square FLL appears approximately below 0.4 K, but based on available data exact onset of square FLL cannot be determine. Fitting with the Eq. 5.3 (see Fig. 6.6) reveals that $ZrNi_2Ga$ is a single gap, s-wave superconductor with $\Delta = 0.44$ meV, which is consistent with a value predicted for a conventional BCS superconductor (see Section 2.2.1 and Equation 2.5 therein). This reinforce the conclusion that square FLL is present at low temperatures. Additionally, muon spin relaxation experiments in zero magnetic field were carried out to study a possibility of TRS breaking in $ZrNi_2Ga$.

6.4.2 ZF-μSR studies of $ZrNi_2Ga$

Among the Heusler compounds several exotic behaviours/states were observed (see Section 6.2) so it was expected that TRS might be broken in $ZrNi_2Ga$. Appearance of a spontaneous magnetic field, for a superconductor in zero field is evidence that TRS is broken. For the ZF-μSR experiments sample was cooled in zero field to the base temperature and measurements were carried out on warming in both superconducting (at T = 0.1 K) and normal states (at T = 3 K) of $ZrNi_2Ga$ (see Fig. 6.7).

No difference (in the range of errors) between the spectra was observed (see a difference plot in the inset of Fig. 6.7), so no evidence of TRS breaking was observed within the detection range of μSR.

6.4.3 Conclusions

μSR studies of the Heusler compound superconducting $ZrNi_2Ga$ were performed. Muons interacted with the flux line lattice of $ZrNi_2Ga$ and information about the

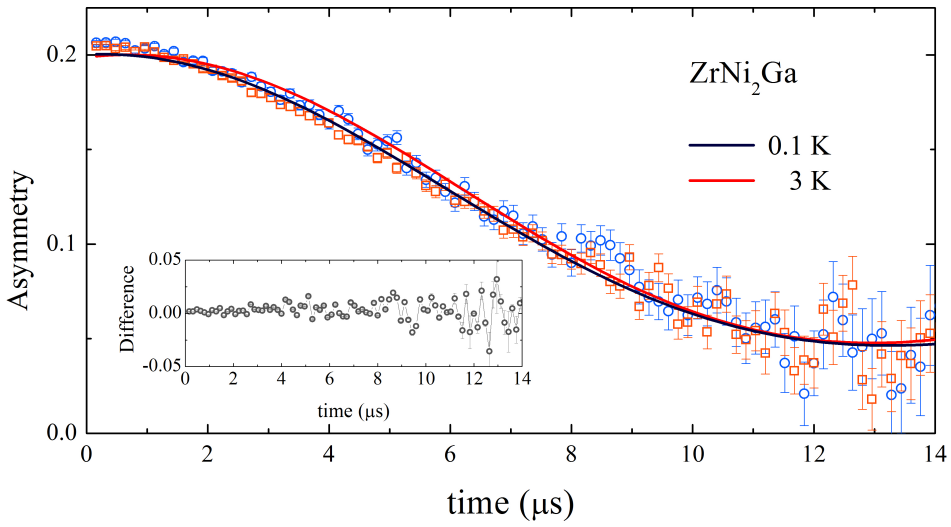

Figure 6.7: Time dependence of the muon asymmetry for $ZrNi_2Ga$. Measurements were performed in zero field, in the superconducting (T =0.1 K, marked with squares) and normal states (T = 3 K, marked with circles) of $ZrNi_2Ga$. The lines are fit to the data with function with Kubo-Toyabe depolarisation (see Eq. 3.10 and the fitted parameters are presented in Table 6.2). Inset shows a plot of difference between spectra taken in the superconducting and normal states of $ZrNi_2Ga$.

T (K)	A_0	Δ_{KT} (μs^{-1})	Λ (μs^{-1})	A_{bcg}
0.1	0.16 ± 0.006	0.131 ± 0.005	-0.01 ± 0.01	0.04
3	0.159 ± 0.006	0.133 ± 0.004	-0.02 ± 0.01	0.04

Table 6.2: Parameters of the fit with Eq. 3.10 to ZF-μSR spectra for $ZrNi_2Ga$ (see Fig. 6.7).

superconducting ground state were obtained. An unusual behaviour of the superfluid density was observed. The temperature evolution of the muon depolarisation rate, which is proportional to the superfluid density, gives evidence that an area of a square FLL exists in the $ZrNi_2Ga$ phase diagram at low temperatures. At higher temperatures, below T_c, a hexagonal FLL is present. The superfluid density behaviour also shows that $ZrNi_2Ga$ is a s-wave superconductor with a gap of 0.44 meV, which is in agreement with the gap value anticipated in the BCS theory. No evidence of TRS breaking was observed within the detection limit of μSR. Hence we can conclude that $ZrNi_2Ga$ is a conventional, BCS superconductor.

6.5 μSR studies of $NbNi_2Ga$

6.5.1 TF-μSR studies of $NbNi_2Ga$

The flux line lattice of another Heusler compound, $NbNi_2Ga$, was studied using the muon spin rotation technique. The principles of the experiment are described in Section 3.4. A polycrystalline powdered sample was mounted with GE varnish on a silver plate and covered by thin silver foil. The sample was cooled in a dilution refrigerator, allowing for temperatures as low as 60 mK, and measurements were carried out on warming in a range of magnetic fields and temperatures.

μSR measurements were carried out in the superconducting and normal states of $NbNi_2Ga$ in an applied magnetic field $H = 400$ Oe and Fig. 6.8 presents the time evolution of the muon asymmetry spectra for $NbNi_2Ga$ in $H = 400$ Oe. Spectra in the superconducting and normal states are shown, at $T = 0.075$ K (Fig. 6.8(a)) and $T = 2$ K, respectively (Fig. 6.8(b)). In the superconducting state, oscillations decay with time, due to the presence of the FLL. The asymmetry signal in the normal state is also slightly damped, possibly due to the presence of local magnetic moments of Ni (see Fig. 6.8(b)). Measured muon spectra (see. Fig. 6.8) are well described by the function with sinusoidal oscillations and Gaussian relaxation. Data from the two virtual orthogonal detectors were fitted simultaneously with an Eq. 6.1. The value of initial asymmetry A_2 for the background term, was obtained from the fitting to a spectra acquired at a base temperature and later, A_2 was fixed for all the other spectra. Figure 6.8 presents only spectra from one virtual detector for clarity of presentation. From the fitting with Eq. 6.1, the temperature dependence of the muon depolarisation rate and the internal magnetic field can be obtained. So the fundamental characteristics of $NbNi_2Ga$ can be examined with TF-μSR. In particular, the muon depolarisation rate is related to the magnetic penetration depth, and hence provides information about the superfluid density. The μSR measurements were carried out in several applied magnetic fields and Figure 6.9(a) shows the temperature

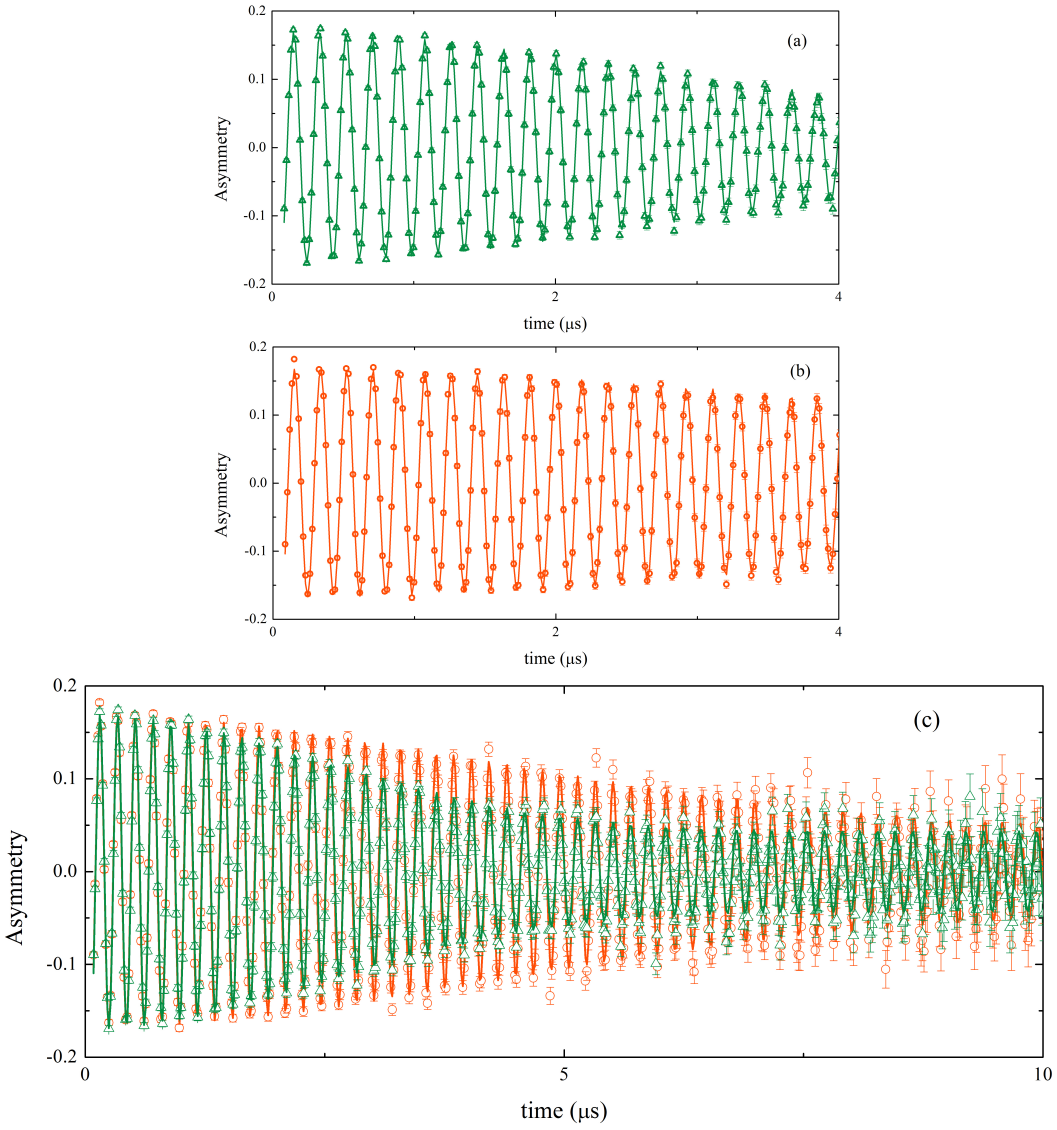

Figure 6.8: Muon asymmetry spectra for $NbNi_2Ga$ obtained using muon spin rotation technique. Measurements were performed in the applied magnetic field of 400 Oe, (a) at $T = 0.075$ K and (b) at $T = 2$ K, when sample in the superconducting and normal states, respectively. Curves are a result of a fitting with Eq. 6.1. (c) Both spectra in the superconducting (triangles) and normal states (circles) shown together for comparison. See text for details.

dependence of the muon depolarisation rate, for $NbNi_2Ga$ in the magnetic fields of 200 and 400 Oe. The depolarisation rate is constant at low temperatures. Above half-T_c, with temperature increases, σ decreases and saturates again at T_c=≈ 1.5 K, when $NbNi_2Ga$ in the normal state. So the temperature evolution of σ was as expected for a conventional BCS superconductor. Also, the temperature dependence of the mean internal magnetic field was acquired. Figure 6.9(b) shows the normalized magnetic field ΔB for $NbNi_2Ga$ in a function of temperature, where ΔB is the difference between the applied magnetic field, B_{applied}, and the magnetic field measured using μSR, B_{measured}. The values of internal magnetic field obtained from the fitting of the spectra with Eq. 6.1, were close to the values of the applied magnetic field which suggest significant pinning for the $NbNi_2Ga$ FLL. The transition temperatures observed for temperature dependence of σ as well as temperature dependence of ΔB are in agreement and $T_c \approx 1.5$ K can be concluded, which is in agreement with previously reported data [170].

Our μSR measurements shows that the value of σ, for $NbNi_2Ga$ in the low applied magnetic fields, is only weakly field-dependent (see Fig. 6.9(a) and Fig. 6.10), which suggests that the H_{c2} is relatively high. A relation between the superconducting contribution to the depolarisation rate (σ_{sc}) and a magnetic penetration depth is described well with Eq. 3.15. To determine the value of H_{c2}, the field dependence of σ_{sc} at $T = 0.4$ K was fitted with Eq. 3.15 and $H_{c2}(0.4) = 1.9$ T $\pm$ 0.6 T was obtained (see Fig. 6.10). Waki *et al.* [170] reported a much lower H_{c2} value of 0.6 T (see Section 6.3.2). Establishing H_{c2} would be crucial to the study of the magnetic penetration depth and the superconducting order parameter in $NbNi_2Ga$. If H_{c2} is high, for the FLL at low fields (where the μSR measurements were carried out), the distances between vortices are large and Eq. 3.14 describes well the relation between σ and λ. However if H_{c2} is low, the magnetic field need to be taken into consideration (due to the overlapping of the vortex cores) and σ and λ are related as in Eq. 3.15. Therefore H_{c2} would require further investigation. Furthermore, muon

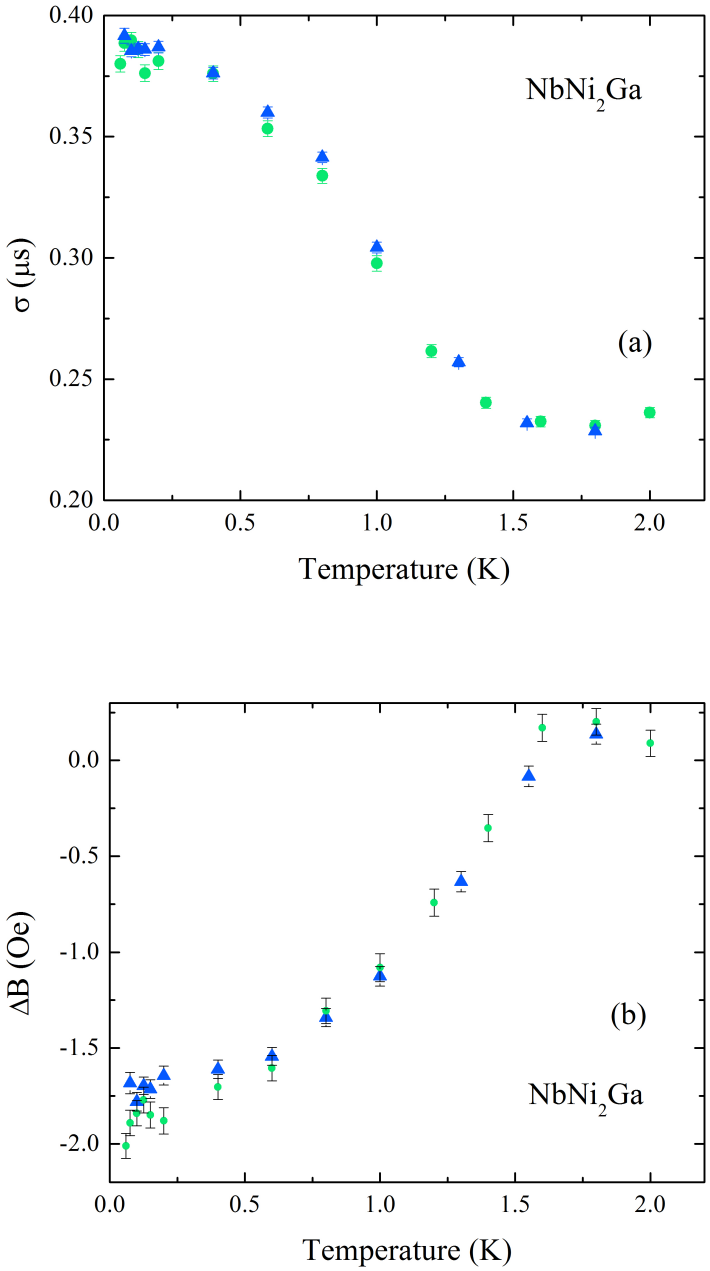

Figure 6.9: (a) Temperature dependence of muon depolarisation rate, σ_{sc} for $NbNi_2Ga$. Measurements were performed in an applied magnetic fields 200 Oe (triangles) and 400 Oe (circles).
(b) Temperature dependence of the normalized magnetic field ΔB for $NbNi_2Ga$, where $\Delta B = B_{\text{applied}} - B_{\text{measured}}$. Measurements were performed in 200 Oe (triangles) and 400 Oe (circles).

spin relaxation measurements in zero magnetic field were performed to investigate TRS for superconducting state of $NbNi_2Ga$.

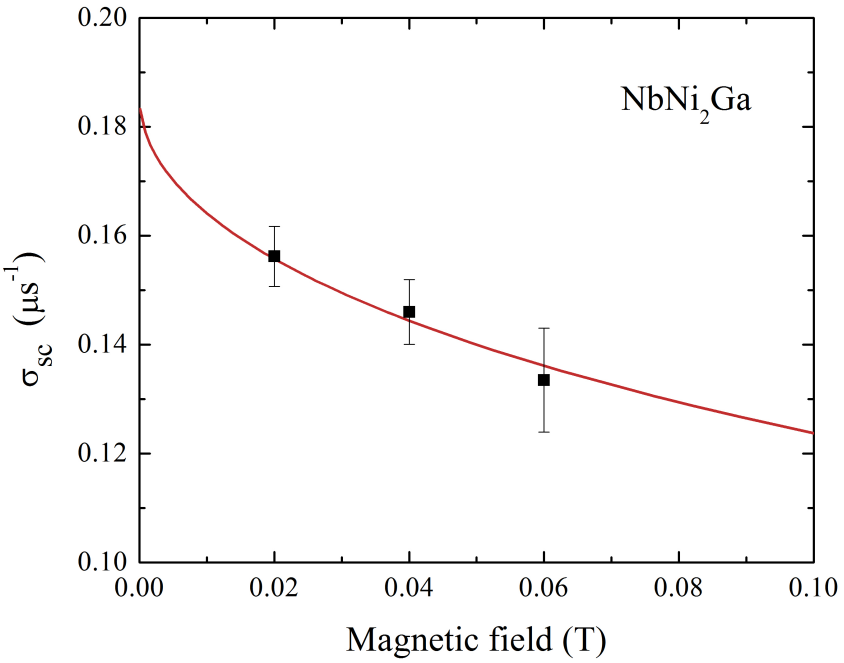

Figure 6.10: Field dependence of the muon depolarisation rate for $NbNi_2Ga$ at $T = 0.4$ K. A curve is a fit with Eq. 3.15. See text for details.

6.5.2 ZF-μSR studies of $NbNi_2Ga$

For a superconductor, which breaks TRS, a small spontaneous magnetic field can be observed, when measurements are performed in zero magnetic field. μSR can detect magnetic fields as low as 10^{-5} G and unlike many experimental techniques, do not require the applied magnetic field to perform the measurements, so is an ideal probe of TRS breaking. The sample on a silver holder was inserted into the dilution fridge. To ensure no external magnetic field is present, a set of compensation coils was used and ZF-μSR measurements were performed in the superconducting and normal states of $NbNi_2Ga$. No difference between the signals below and above T_c was observed, confirming that no spontaneous magnetic field was detected, hence no evidence of TRS breaking was observed within the detection limits of μSR.

6.6 Summary and conclusions

The studies of the flux line lattice in Heusler compounds, superconducting $ZrNi_2Ga$ and $NbNi_2Ga$ were performed using μSR. Observation of the FLL in a range of temperatures and magnetic fields provides informations about the superfluid density behaviour which is a fundamental characteristic of a superconductor. μSR studies shows that $ZrNi_2Ga$ is a conventional superconductor with a BCS, single isotropic s-wave gap. This may imply that the half-filled band at the Fermi surface is not contributing to the superconductivity of $ZrNi_2Ga$ or that the band is not half-filled. Moreover, an unusual temperature evolution of the superfluid density was observed, which could be evidence of a structural change in the flux line lattice. It was suggested that a square vortex lattice exists in $ZrNi_2Ga$ at low temperatures.

We examined another member of Heusler family, superconducting $NbNi_2Ga$ which again shows no evidence of unconventional behaviour. Although it was concluded that additional upper critical field studies would be required to carry out further analysis of the μSR spectra. Preliminary results indicate conventional superconductivity in $NbNi_2Ga$.

Additionally, the muon spin relaxation experiments in zero field were carried but no any spontaneous magnetic field was found, which gives evidence that TRS is preserved in $ZrNi_2Ga$ and $NbNi_2Ga$.

Chapter 7

Studies of the Vortex Lattice in ZrB_{12}

7.1 Chapter Outline

ZrB_{12} has a relatively high T_c∼6 K amongst the family of cubic dodecaborides. The nature of the complex superconductivity in ZrB_{12} has been extensively studied and several, sometimes contradictory models have been suggested to explain the physical properties of ZrB_{12} (see Section 7.2). It was reported that the value of the Ginzburg - Landau parameter κ lies near the crossover value of $1/\sqrt{2}$ between type I and type II superconductors [180, 181], so interesting behaviour in this marginal superconductor might be expected, i.e. even possibly 1.5 type superconductivity. Recently, the complete superconducting phase diagram was constructed using muon spectroscopy (see Fig. 7.2). In the magnetic phase diagram of ZrB_{12}, regions characteristic for a type I superconductors were observed, also regions, where ZrB_{12} behaves like a type II superconductor were reported, additionally, coexistence of a type I and type II behaviour was though to be present [182].

This rich superconducting phase diagram of ZrB_{12} was a motivation behind our SANS experiment. The morphology of the FLL was studied as a function of

magnetic field and temperature in the different states across the superconducting phase diagram.

7.2 Superconductivity in ZrB_{12}

ZrB_{12} crystallizes in the $Fm\bar{3}m$ space group with the UB_{12}-structure. In a face-centred cubic structure of ZrB_{12} (a = 7.408Å), each Zr atom is surrounded by a cage of 24 B atoms [183, 184] (see Fig. 7.1). Superconductivity in ZrB_{12} was first reported by Matthias *et al.* [185]. The T_c of ZrB_{12} is ∼6 K [186, 187] which is relatively high amongst the cubic dodecaborides. Several models have been suggested to explain the nature of the superconductivity in ZrB_{12}.

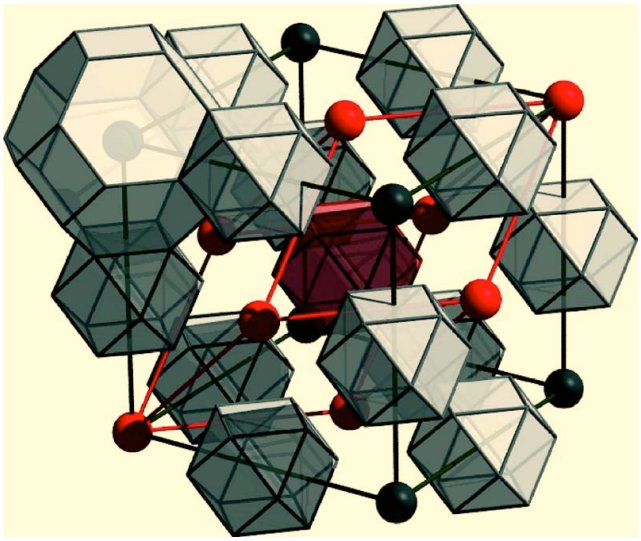

Figure 7.1: The structure of ZrB_{12}. Black and red spheres mark Zr and B atoms, respectively. Taken from [188].

Optical conductivity measurements indicate good metallic behaviour in ZrB_{12}, although some inconsistency from conventional metallic behaviour was pointed out [188]. The calculated band structure also predicts metallic-like behaviour in this compound [189]. It was found that in ZrB_{12}, B atoms are responsible for the metallic-like behaviour [189]. Zr atoms control the superconducting properties, because a larger isotope effect in ZrB_{12} was found for Zr, than for B [188]. Shein *et al.* compared

the band structure calculations for ZrB_{12} and YB_{12}, which is superconducting below $T_c = 4.7$ K and concluded that the increase of T_c corresponds to the increase in the contribution of metallic *4d* states to the total density of states [189].

Contradictory conclusions about the electron-phonon coupling strength in ZrB_{12} were reported. Some measurements suggest that ZrB_{12} is a weak-coupling superconductor with $\lambda_{el-ph} \sim 0.67$ [180] or a medium-strength-coupling superconductor with $\lambda_{el-ph} = 1.0(3)$ [188]. Other measurements implied that strong electron-phonon interactions are present, because the ratio $2\Delta_0/k_BT_c$ obtained using point-spectroscopy measurements and tunnelling measurements was 4.8, which is relatively large [180, 184]. These contradicting results were later associated with the presence of surface superconductivity in ZrB_{12} [180, 187]. Also further heat capacity measurements were carried out and the ratio $2\Delta_0/k_BT_c$ was found to be 3.7 [186], which is much closer to the BCS value.

It was suggested that ZrB_{12} has an s-wave superconducting order parameter [180, 184] with a superconducting gap $\Delta_0 \sim 1.2$ meV [187]. Gasparov *et al.* reported that two superconducting gaps exist in ZrB_{12}, they suggested the presence of two superconducting bands with the d- and p-wave order parameters and the gap energies of $\Delta_d(0) = 2.1$ meV and $\Delta_p(0) = 0.73$ meV, respectively [190].

The upper critical field value of 550 G for ZrB_{12} was found using heat capacity measurements and the WHH model [181]. Previously reported higher values of H_{c2} were obtained using surface-sensitive techniques [184, 190]. And these were later associated with surface superconductivity and $H_{c3} \sim 1000$ G [181]. The penetration depth of ZrB_{12} was found to be ~ 140 nm [187, 190]. The coherence length reported by Gasparov *et al.* is $\xi = 45$ nm [190]. Previously reported values of the Ginzburg - Landau parameter are $\kappa = 0.71$ [180] or $\kappa \equiv \kappa_1(T_c) = 0.65$ [181], so κ is near the crossover value of $1/\sqrt{2}$ between type I and type II superconductivity. Also the value of κ in ZrB_{12} changes with temperature [181]. Wang *et al.* studied ZrB_{12} using specific heat measurements in a range of the applied magnetic fields and

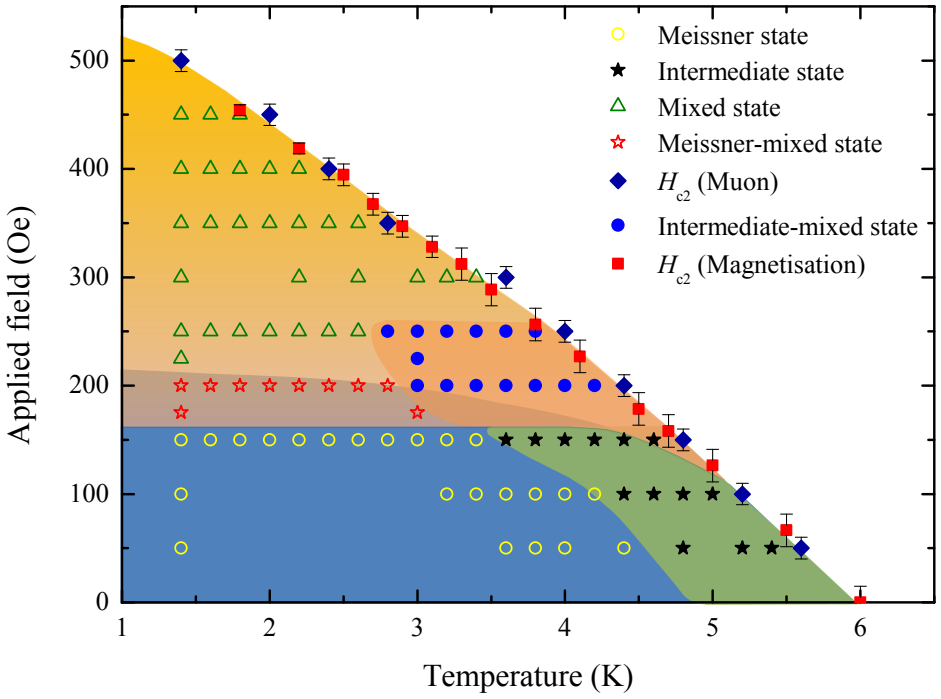

Figure 7.2: Phase diagram of ZrB_{12} determined from TF-μSR measurements. The upper critical field values are marked with red squares and were established from magnetization measurements. Several superconducting phases exist in ZrB_{12} and those are marked with different background colours. Experimentally obtained data points are marked on the figure. Taken from [182].

suggested the presence of superconducting states characteristic of type I and type II superconductors [181].

Recently, a complete superconducting phase diagram of ZrB_{12} (see Fig. 7.2) was determined using muon spectroscopy experiments [182]. TF-μSR measurements on single crystals of ZrB_{12} revealed the presence of the Meissner and intermediate states, typical for a type I superconductor, as well as the mixed state, which exists in a type II superconductor. Also coexistence between these superconducting phases was observed for certain fields-temperatures (see Fig. 7.2). The rich superconducting phase diagram of ZrB_{12} required a further examination, so SANS studies were carried out.

7.3 Small Angle Neutron Scattering studies of superconducting ZrB_{12}

7.3.1 $Zr^{11}B_{12}$ sample preparation

The single crystals of $Zr^{11}B_{12}$ were grown by Prof. G. Balakrishnan *et al.* using the floating zone technique in the four-mirror infrared image furnace, in high purity argon gas [157, 191]. The crystals have been grown starting with an enriched ^{11}B isotope to have a smaller absorption cross section for neutrons than normal boron. Prior to the SANS measurements, the crystal was aligned using Laue X-ray diffraction (the Laue diffraction technique was introduced in Section 3.1.3) and a slice from the crystal was cut using a spark cutter. Figure 7.3 shows the Laue diffraction pattern of the $Zr^{11}B_{12}$ piece, which was used in the SANS experiment. The [100], [010] and [001] axes are equivalent in a cubic system. So the [100] $\equiv$ [010] $\equiv$ [001] principal axis of the single crystal was parallel to the X-ray beam.

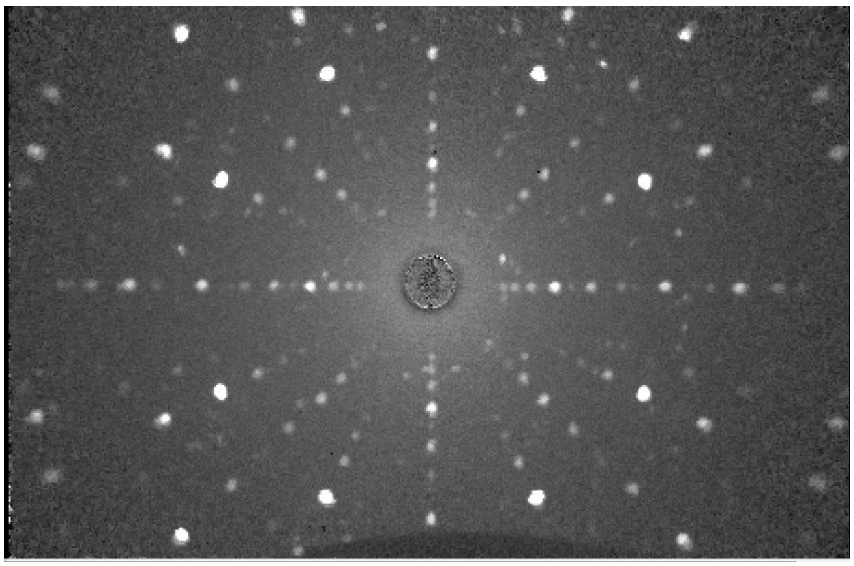

Figure 7.3: Laue diffraction pattern of $Zr^{11}B_{12}$ single crystal. The principal axis of the single crystal was parallel to the X-ray beam.

Magnetization measurements were carried out using an MPMS in a low magnetic field of 10 Oe. A T_c of $\sim$6 K was observed, which is in agreement with preciously reported

values [186, 187]. For SANS measurements, the slice of $Zr^{11}B_{12}$ single crystal was mounted on an aluminium holder (see Fig. 7.4) and covered with a thin aluminium foil to ensure better thermal contact.

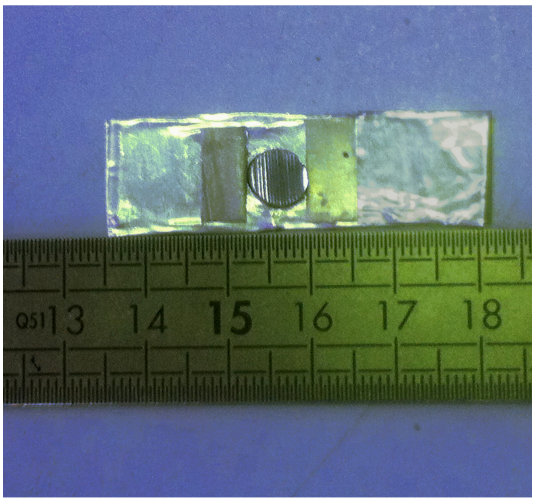

Figure 7.4: Sample for SANS experiments. A slice of the $Zr^{11}B_{12}$ single crystal was placed on an aluminium holder, which was then covered with a thin aluminium foil and inserted into the cryostat.

7.3.2 Results and discussion

SANS experiments were performed using the D22 instrument in the ILL, France. A slice of the $Zr^{11}B_{12}$ single crystal was mounted on an aluminium holder (see Fig. 7.4) and was inserted into a cryostat with the base temperature $T \approx 1.55$ K. Measurements were carried out in the field-cooled conditions, so a magnetic field was applied in the normal state of ZrB_{12} and then the sample was cooled to the base temperature and measurements were carried out on warming in a range of temperatures. Figure 7.5 shows a straight through diffraction pattern of the FLL in ZrB_{12} at the base temperature $T = 1.55$ K, in an applied magnetic field of 240 Oe. The SANS pattern for ZrB_{12} in the normal state was subtracted to correct for the background contributions. A smoothing function was applied to data for clarity of presentation.

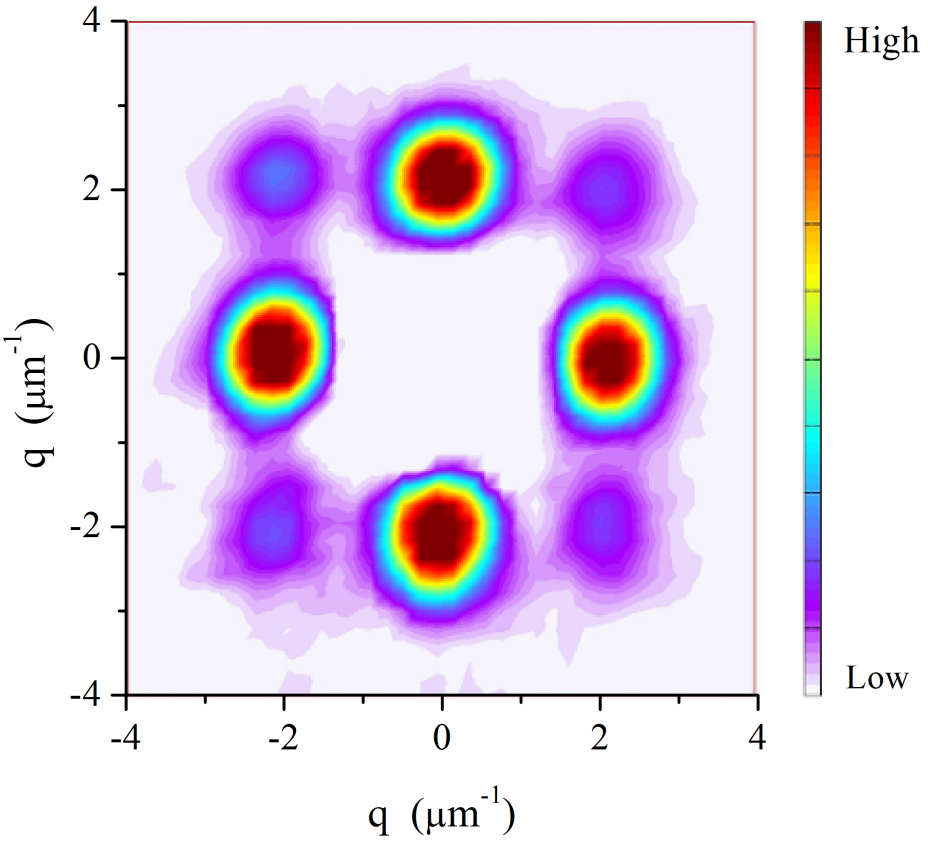

Figure 7.5: SANS diffraction pattern of ZrB_{12} FLL at $T = 1.55$ K in an applied magnetic field of 240 Oe. Measurements were performed using the D22 instrument in ILL and a wavelength $\lambda_{wv} = 14$ Å. A diffraction pattern measured at 7 K was subtracted to eliminate the background contribution and a smoothing function was applied.

Figure 7.5 shows four, spaced by 90°, (10) Bragg peaks of a square FLL. Higher order reflections, (11) Bragg peaks, were also visible (weaker reflections in Fig. 7.5). A FLL with a square symmetry was observed thorough the mixed state of ZrB_{12} for a range of applied magnetic fields and temperatures (45 Oe $< H <$ 350 Oe and 1.55 K $< T <$ 4.5 K). Measurements were also performed at higher temperatures and magnetic fields, but there was not enough intensity to observe the FLL and no measurements were performed below 1.55 K, which was the base temperature of the cryostat.

Magnetic flux in the mixed state of superconductors forms a periodic lattice to minimize the free energy (more information about the FLL can be found in Sections 2.1 and 3.4.3). A hexagonal vortex lattice minimizes the free energy, but the free energy for square vortex lattice is only 2% higher so the FLL in a superconductor can be square. Square FLLs have usually been observed in low-κ (i.e. borocarbides) or marginal superconductors (i.e. Nb) [19, 23].

To explain the presence of the square FLL several different mechanisms were suggested. In-plane anisotropy of the Fermi surface [19, 192] or the anisotropy of H_{c2} might cause a presence of a square FLL [193]. SANS studies have shown a square FLL in the superconducting YNi_2B_2C [23]. It was suggested that a square vortex lattice exists throughout the magnetic phase diagram of YNi_2B_2C due to non-local effects [194], which persist even close to T_c [195]. Eskildsen *et al.* show that a square FLL in $TmNi_2B_2C$ might be caused by the magnetic order with a square symmetry, which exist in this material [22]. A square vortex lattice cannot be explained using just the GL theory [196], to integrate a square vortex lattice in the GL theory, it is necessary to include additional higher-order gradient terms [19]. The presence of a square FLL can also be described using extended GL theories [19]. Kogan *et al.* presented a modified London equation, which includes non-local effects, hence allows for the presence of a square FLL [192, 197, 198].

ZrB_{12} has a cubic structure so no H_{c2} anisotropy was observed. Also, no magnetic order is present in ZrB_{12}. ZrB_{12} with its low-κ value is a marginal superconductor. The anisotropy of the Fermi surface influences the FLL, especially in marginal superconductors [21]. It was suggested that anisotropy of the Fermi surface or anisotropy of the superconducting energy gap can lead to a presence of non-local effects and hence to a presence of a square FLL [195]. For ZrB_{12}, Gasparov *et al.* reports evidences of two superconducting energy gaps, an isotropic s-wave gap and anisotropic d-wave gap, so it is a possible source of non-local effects in ZrB_{12}.

Previous reports suggests that H_{c1} of ZrB_{12} is ∼200 Oe [180], according to recent superconducting phase diagram, the Meissner state exists in the whole material only below ∼160 Oe [182]. Figure 7.6 shows a diffraction pattern for ZrB_{12} FLL measured at $T = 1.6$ K in the applied magnetic field of 95 Oe, so well below the reported H_{c1} value. Our SANS experiments suggest the presence of the signal in the applied magnetic field as low as 45 Oe (see Fig. 7.7). The presence of the FLL in a so low magnetic field, is possibly due to a strong pinning in the sample, similar to the pinning observed using SANS in YBCO [199].

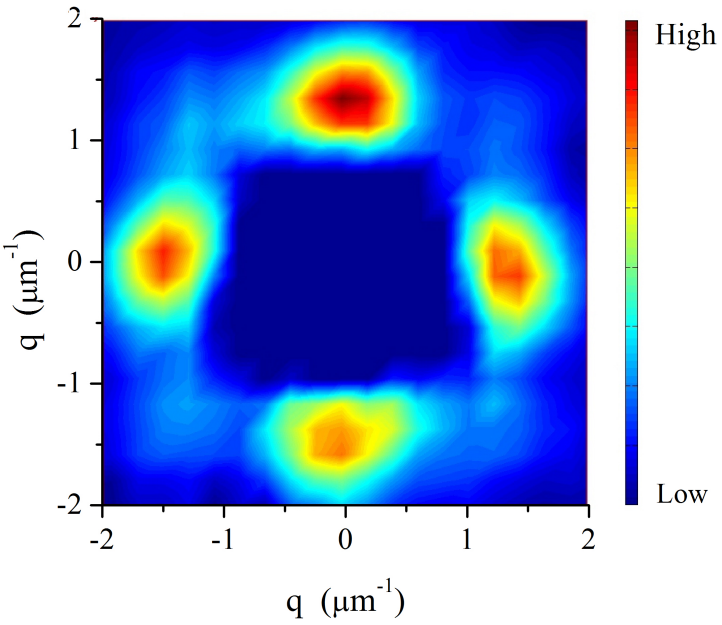

Figure 7.6: SANS diffraction pattern from the FLL in ZrB_{12}. Measurements were carried out at $T = 1.6$ K, in the applied magnetic field of 95 Oe. The direct beam contribution in the centre of the area-detector was masked and a smoothing function was applied for a clarity of presentation.

To study the magnetic field evolution of the superconducting state of ZrB_{12}, SANS diffraction patterns were measured in a range of magnetic fields, while the temperature was kept constant. The SANS measurements were carried out in a magnetic fields from 165 Oe to 500 Oe, however above ∼350 Oe the intensity was

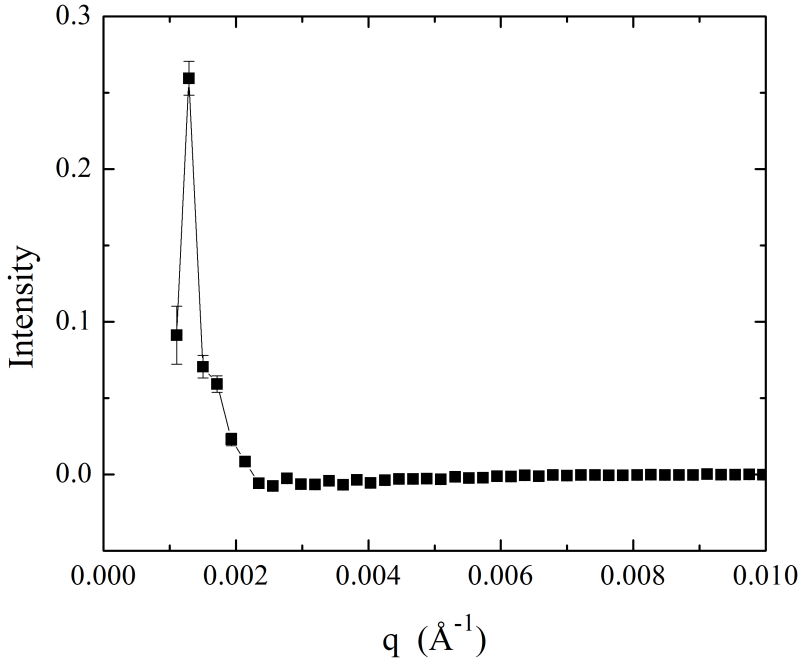

Figure 7.7: Radial intensity distribution from the detector area for ZrB_{12} in an applied field, $H = 45$ Oe. Lines are a guide to eye. Slightly negative intensity values at higher q are a result of the background subtraction. At higher q, the coherent scattering is week so the absolute values of intensity at high q have relatively large uncertainties [200, 201].

too low to observe the FLL. The neutron reflectivity for each of the (10) Bragg peaks was found using the 2D Gaussian fitting. The intensity integrated over a range of rotation angles to satisfy the Bragg conditions gives the absolute value of the neutron reflectivity. Our studies were focused on the observation of the FLL in the different superconducting phases, so measuring the absolute values was not so essential. Our measurements were performed with the position of the sample fixed on the particular san and phi angles (see Fig. 3.14). It was found to be a good approximation, because the values of the intensity have been similar for all four Bragg spots in a particular SANS pattern. A direct beam correction was applied to data so the measured neutron reflectivity was divided by incoming beam intensity and normalized to the time of the measurements.

Fig. 7.8 shows the field dependence of the neutron reflectivity for ZrB_{12} at

$T = 2$ K (blue circles) and, for comparison, at $T = 2.3$ K (orange squares). SANS

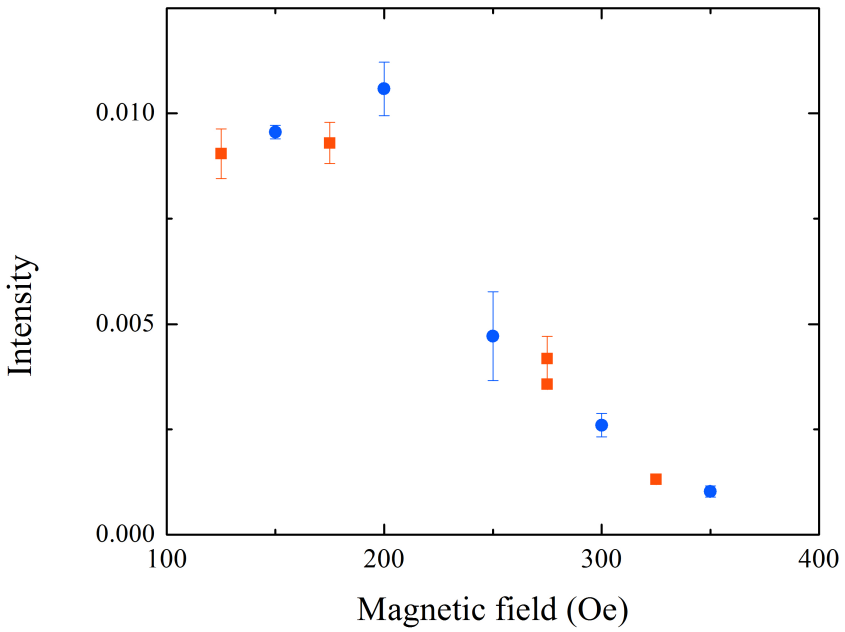

Figure 7.8: Field dependence of the neutron reflectivity for ZrB_{12}. SANS measurements were performed at 2 K (blue circles) and 2.3 K (orange squares) in a range of the magnetic fields.

pattern at the particular temperature includes four (10) Bragg spots and their values of intensity were derived. To determine a value of the neutron reflectivity at particular temperature, an average of the values from four spots was taken. And the values of the neutron intensity presented on the graph are the average values . Nearly identical field dependence of intensity was found at $T = 2$ K and at $T = 2.3$ K. The decrease of the intensity in the low magnetic fields could be evidence of changes in the FLL but fourfold symmetry was detected for ZrB_{12} FLL in the whole measured field range. This unusual temperature evolution of neutron reflectivity also may indicate changes in the character of the superconducting state. The superconducting phase diagram reported by Biswas [182] (see Fig. 7.2), shows that superconducting ZrB_{12} at 2 K is in the Meissner state in low magnetic fields, then above $H \sim 160$ Oe, it enters Meissner-mixed state and for $H > 220$ Oe, ZrB_{12} is in the mixed state. A similar field-dependence was observed at 2.3 K, which is consistent with our SANS studies.

A decrease of the intensity in the low magnetic fields (see Fig. 7.8) could be explain by the presence of Meissner state domains, where the magnetic flux is expelled and the SANS signal only comes from domains in the mixed state. Diffraction by the FLL occurs, but the intensity is lower than when the mixed state is present in the whole sample.

For a comparison, Fig. 7.9 shows the temperature dependence of the neutron reflectivity for ZrB_{12} in $H = 320$ Oe. According to Biswas, for $H = 320$ Oe, ZrB_{12} is in the mixed state in a whole temperature range. Measured neutron reflectivity (R) increases with decreasing temperature and probably tends to saturation at the low temperatures (see Fig. 7.9).

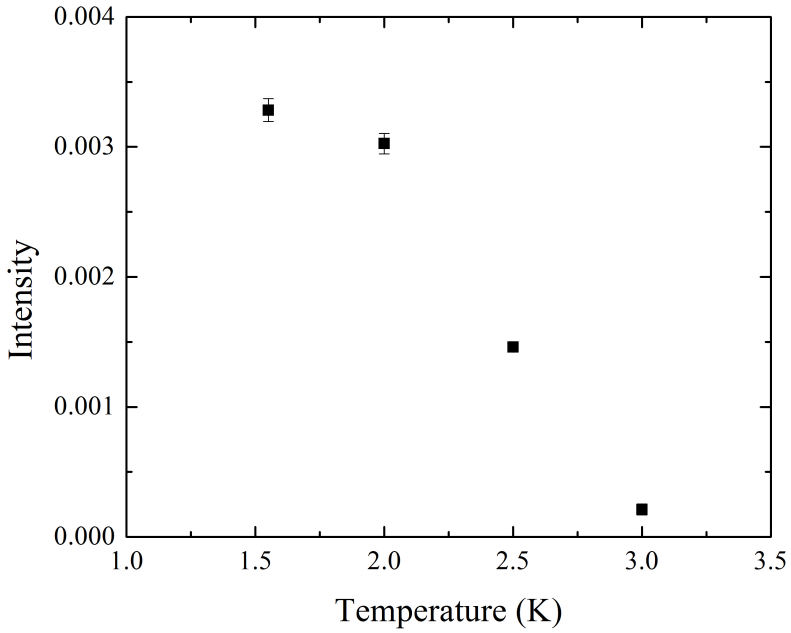

Figure 7.9: Temperature dependence of the neutron reflectivity in the mixed state of ZrB_{12}. SANS measurements were performed in $H = 320$ Oe.

According to the superconducting phase diagram reported by Biswas [182] (see Fig. 7.2), in the applied magnetic field of 240 Oe, ZrB_{12} is in the mixed state at the low temperatures and the intermediate-mixed state was observed above $\sim$3 K. So for ZrB_{12} in $H = 240$ Oe, SANS measurement were carried out in a range of

temperatures. In a low applied magnetic field, the distance between vortices is large so the Bragg spots appears at very small q values. A bright contribution from the direct beam, also appears at low-q, hence this is a significant complication for the measurements of the FLL in a low applied magnetic fields. An attempt was made to reduce this direct beam intensity. For some measurements, a 30 mm diameter hole was in place to attenuate the neutron beam before the collimation section of the instrument. In Fig. 7.10 data obtained using the attenuated beam are marked with filled squares and it could be noticed that those data have large errors. This is due to the less intense neutron beam, so a less favourable signal-noise ratio.

For ZrB_{12}, in $H = 240$ Oe, above $\sim$3 K the mixture of the intermediate and mixed state is present, so areas of the intermediate state, as well as areas of the mixed state exists in the material. SANS is a diffraction technique so it measures periodic structures but the intermediate state is a disordered state then the main observed diffraction signal comes from the FLL in the mixed state. Magnetic field present in the intermediate state would only cause a weak, diffuse, disordered scattering all over the q-domain. The presence of a disordered structure would not influence the value of the scattering vector q, because the spacing between the vortices remains unchanged so the spacing between the Bragg planes is unaffected. But the intensity of the Bragg peaks may be lower and peaks become broader due to the presence of a disordered structure in the sample.

For ZrB_{12} in $H = 240$ Oe, the radial intensity distributions for each SANS pattern measured in different temperature were obtained and a Gaussian fit was made to the data to find the values of the magnitude of the scattering vector (q) for the (10) Bragg peaks from the ZrB_{12} FLL (shown in Fig. 7.10). It was concluded that q_{10} was temperature independent as expected.

For a square FLL, the relation between the magnitude of the scattering vector and the magnetic field in the normal core of the FLL (B) can be written as in the

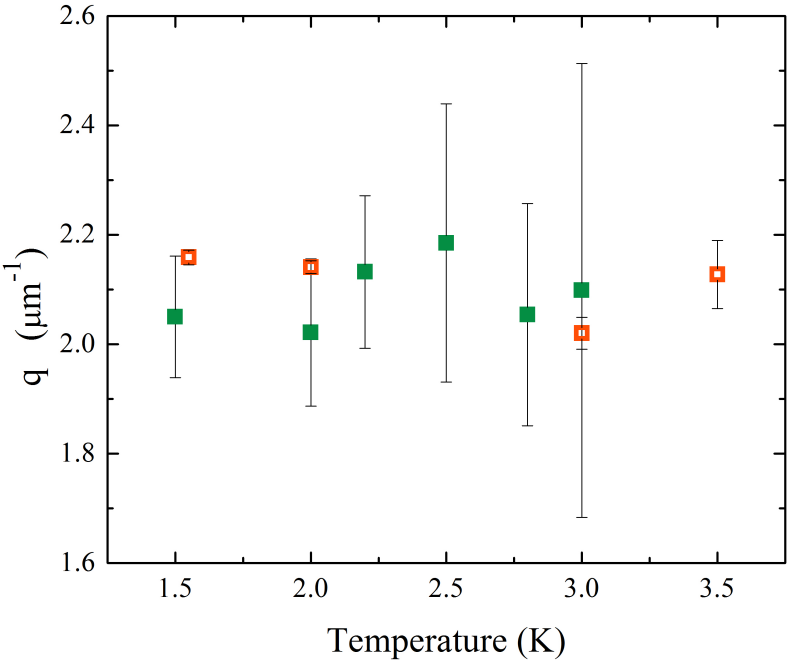

Figure 7.10: Magnitudes of the scattering vector (q) for the reflections from the FLL of ZrB_{12} as a function of temperature. Measurements were carried out in an applied magnetic field of 240 Oe. Filled square symbols marks the data acquired using the attenuated neutron beam, hollow symbols represent the data from the measurements without the attenuation. See the text for detail.

equation [161]:

$$a_0 = 2\pi/q_0 = (\phi_0/B)^{1/2} \tag{7.1}$$

where a_0 is the lattice parameter of the FLL. For (10) Bragg reflection $q_{10} = q_0$ because the scattering vector can be describe using equation [202]:

$$q_{hk} = q_0\sqrt{h^2 + k^2} \tag{7.2}$$

For ZrB_{12} in $H = 240$ Oe, the magnitudes of the scattering vector (q_0) in whole temperature range (as shown in Fig. 7.10) were averaged out and $q_0 = (0.00209 \pm 0.00002)$ Å^{-1} was derived. From Eq. 7.1, $q_0 = 0.00209$ Å^{-1} represents an internal magnetic field of (230±6) Oe.

The form factor is related to the penetration depth hence to the superfluid

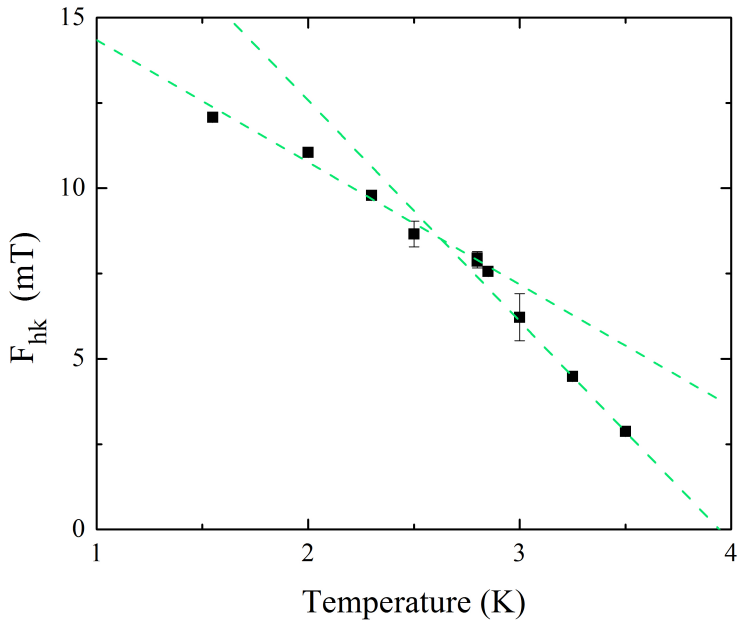

Figure 7.11: Temperature dependence of the vortex lattice form factor for ZrB_{12}. Measurements were taken in $H = 240$ Oe. Dashed line are a guide to eye, to mark an abrupt change in the slope (see text for detail).

density so potential changes in the superconducting ground state of ZrB_{12} can be studied. A form factor can be derived from the measured neutron reflectivity using Eq. 4.7. The neutron reflectivity was derived from SANS diffraction patterns measured with the sample placed at a fixed angular position and the direct beam correction was applied. The neutron reflectivity for each of the (10) Bragg peaks was found using 2D Gaussian fitting and the average of obtained 4 values (from 4 Bragg (10) spots in the SANS pattern) was used to find the F_{hk} from Eq. 4.7. Fig. 7.11 shows the temperature dependence of F_{hk} for ZrB_{12} in $H = 240$ Oe. A change in the form factor is related to a change in the superfluid density of ZrB_{12} and a visible change in the slope was observed around 3 K (two different slopes are marked with dashed lines on Fig. 7.11). Above 3 K, Biswas reports the presence of the intermediate-mixed state in ZrB_{12}. So observed change of neutron reflectivity may indicate that below 3 K ZrB_{12} is in a mixed state, and above 3 K intermediate-mixed state is present [182].

7.4 Summary

A marginal superconductor ZrB_{12} was studied using SANS. The presence of a square vortex lattice throughout the mixed state of ZrB_{12} was observed for a whole range of applied magnetic fields and temperatures (45 Oe $<$ H $<$ 350 Oe and 1.55 K $<$ T $<$ 4.5 K). Previously, extensive studies of ZrB_{12} were carried out using several techniques but this is a first report of a square VL in this compound. The presence of the square FLL in ZrB_{12} is caused by non-local effects.

Recently, the complete superconducting phase diagram was obtained using the μSR experiments [182] and superconducting characteristic of a type I, as well as a type II superconductor were identified. In addition, a coexistence of type I and type II superconductivity was observed. Our SANS measurements supports those observations and the existence of different superconducting states throughout the superconducting phase diagram of ZrB_{12} was confirmed.

Chapter 8

Conclusions and further work

Curiosity demands that we ask questions, that we try to put things together and try to understand this multitude of aspects as perhaps resulting from the action of a relatively small number of elemental things and forces acting in an infinite variety of combinations [93].

Richard P. Feynman: *The Feynman Lectures on Physics*

Discovered in the eighties of the 20th-century, unconventional superconductors continue to attract the attention of the scientific community. Unconventional superconductivity has been identified in numerous classes of compounds and extensive studies of those have been carried out. Yet to fully understand the mechanism of superconductivity, more theoretical and experimental undertakings are needed [1, 5]. This thesis presents muon and neutron studies of a few superconductors: Ru_7B_3, α-BiPd, ZrB_{12}, $ZrNi_2Ga$ and $NbNi_2Ga$ and expands our knowledge of unconventional superconductivity.

A superconductor with a NCS structure is a potential candidate for unconventional superconductivity because it breaks not only gauge symmetry, but translational symmetry as well. Polycrystalline samples and single crystals of the NCS superconductor Ru_7B_3 were studied using μSR and SANS. It was established that Ru_7B_3, which is a member of 7:3 family of compounds with the Th_7Fe_3-structure, is an

unconventional superconductor. In the absence of a magnetic field, the appearance of a small spontaneous magnetic field was observed using ZF-μSR. This is evidence that time-reversal symmetry is broken in superconducting Ru_7B_3. To date, TRS breaking has only been reported in two other NCS compounds. Evidence of two superconducting gaps was observed in polycrystalline Ru_7B_3 using muon spin rotation. Analysis of the TF-μSR spectra revealed the possible presence of two distinct s-wave gaps, with energies: $\Delta_{1,s} = 0.8 \pm 0.3$ meV, $\Delta_{2,s} = 0.32 \pm 0.06$ meV. The nature of superconducting gap(s) in the superconducting Ru_7B_3 was further studied using a single crystal but no evidence of multigap behaviour was found using TF-μSR. Unusual time evolution of the asymmetry of the muon polarization was observed, which implies an exotic behaviour of the FLL. For both the polycrystalline and a single crystal of Ru_7B_3, an unusual beating was observed in the measured TF-μSR spectra. This might be evidence for either the presence of a square FLL in Ru_7B_3 or an existence of the anisotropy of the FLL for different crystallographic directions. SANS is a direct probe of the morphology of the vortex lattice, so SANS experiments were performed using an isotopically enriched single crystal of $Ru_7{}^{11}B_3$ to reduce neutron absorption. SANS experiments show a distorted hexagonal lattice for the [001] and [100] directions of the Ru_7B_3 crystal. Extremely weak or no anisotropy of the FLL was found so the origin of the unusual behaviour of μSR spectra was not determined. SANS studies show the presence of a second, weaker domain, which may be further evidence of the existence of two different bands at the Fermi surface or the existence of even more exotic states in superconducting Ru_7B_3 (i.e. a non-straight FLL or even the FFLO).

Using muon and neutron studies, evidence was established that TRS is broken in the superconducting state of Ru_7B_3. Evidence of a multiband superconductivity was found in polycrystalline Ru_7B_3. Further studies of the Ru_7B_3 flux line lattice in higher magnetic fields, and in the vicinity of H_{c2}, would be required to advance our understanding of the FLL behaviour in the unconventional superconductor Ru_7B_3.

Another non-centrosymmetric superconductor α-BiPd was studied using muon spectroscopy, magnetic and transport measurements. The value of $H_{c1} = 122$ Oe was established, which is much lower than published values but agrees with the value previously calculated [165]. The presence of the mixed state above $H_{c1} = 122$ Oe was confirmed using μSR experiments. Magnetic and transport measurements show an unusual temperature behaviour of the upper critical field of α-BiPd. The H_{c2} estimated using different techniques did not give consistent results, so the H_{c2} of α-BiPd requires further studies.

Evidence of the presence of two superconducting gaps in α-BiPd has found using μSR measurements. Temperature dependence of the magnetic penetration depth suggest that either two s-wave gaps with energies $\Delta_{1,s} = 0.46 \pm 0.03$ meV, $\Delta_{2,s} = 0.20 \pm 0.05$ meV and $\omega_1 = 0.83 \pm 0.09$ exist in α-BiPd or the s-wave and d-wave gaps with energies $\Delta_{1,s} = 0.38 \pm 0.02$ meV and $\Delta_{2,d} = 0.8 \pm 0.2$ meV, respectively, and $\omega_1 = 0.65 \pm 0.06$ are present in α-BiPd. ZF-μSR studies indicates that TRS is preserved in α-BiPd, but the presence of two distinct superconducting gaps is evidence that non-centrosymmetric α-BiPd is an unconventional superconductor. μSR studies of the single crystal of α-BiPd are underway.

The μSR studies of the FLLs in a couple of the Heusler compounds, $ZrNi_2Ga$ and $NbNi_2Ga$, were carried out. The presence of several different physical properties in a particular Heusler compound is possible due to its tunable electronic structure [168]. The temperature evolution of the superfluid density in $ZrNi_2Ga$ agrees with the BCS theory prediction for a superconductor with a single s-wave gap. This may be an evidence that the half-filled band at the Fermi surface does not participate in the superconductivity of $ZrNi_2Ga$ or that this band is not half-filled. Also no evidence of TRS breaking was observed in the ZF-μSR measurements. It can be concluded that $ZrNi_2Ga$ is a conventional superconductor. Additionally, evidence of a structural change in the FLL was observed. μSR experiments suggest an unusual temperature evolution of the superfluid density at the low temperatures.

This is evidence that a square FLL might exist in $ZrNi_2Ga$ at low temperature and a hexagonal FLL is present in higher temperatures up to T_c. This conclusion would be reinforced using a more direct method of examining of the FLL morphology, i.e. SANS studies of the $ZrNi_2Ga$ would be required but a single crystal of $ZrNi_2Ga$ was not available during the period of this thesis.

Another member of the Heusler family, superconducting $NbNi_2Ga$ was also studied using muon spectroscopy. Again no evidence of unconventional behaviour was observed. However, additional studies of the upper critical field in this superconductor would be needed to perform further analysis of the μSR spectra. The preliminary results suggest that $NbNi_2Ga$ might also be a conventional superconductor.

The complex nature of superconductivity in the marginal superconductor ZrB_{12} makes it an attractive case for SANS studies. SANS experiments established the presence of a square vortex lattice throughout the mixed state of ZrB_{12} for a whole range of the applied magnetic fields and temperatures (45 Oe $<$ H $<$ 350 Oe and 1.6 K $<$ T $<$ 4.5 K). Studies of ZrB_{12} were carried out before, with a wide-range of techniques, but this is a first observation of a square FLL in ZrB_{12}. A square FLL in ZrB_{12} possibly exists as a result of non-local effects caused by the anisotropy of its Fermi surface. Additionally, it was interesting to observe that results of our SANS experiments support the recently presented superconducting phase diagram of ZrB_{12} [182]. Using SANS measurements, the observation of the existence of different superconducting states through the superconducting phase diagram of ZrB_{12} was confirmed. The relatively high critical temperature of ZrB_{12} and its good mechanical properties makes it attractive for potential applications. ZrB_{12} retains its properties even with some stoichiometry change [189], which puts less constraints for thin film preparation. De Bonis *et al.* prepared ZrB_{12} thin films [203], however no measurements of superconducting properties were reported, so a study of the superconducting properties of ZrB_{12} thin film would make an interesting case for further work.

This thesis contains muon and neutron studies of a few superconductors: Ru_7B_3, α-BiPd, ZrB_{12}, $ZrNi_2Ga$ and $NbNi_2Ga$. The presence of unconventional superconductivity was found in the NCS Ru_7B_3 and α-BiPd. The uncommon, square FLL was observed in a marginal superconductor ZrB_{12}, and evidence of a change from a square to hexagonal FLL was found in $ZrNi_2Ga$. No evidence of unconventional superconductivity was identify in $NbNi_2Ga$. This work expands the understanding of superconductivity and shows areas for further studies. The essence of studies of the unconventional superconductors would be appropriately described by a quote from T.M. Rice [204]:

> *One conclusion is, however, inescapable, we can look forward to a future of superconductivity that will likely be as unpredictable as its past [204].*
>
> *T.M. Rice*

Bibliography

[1] M. R. Norman. Unconventional Superconductivity. *ArXiv e-prints*, 2013, 1302.3176.

[2] Ch.P. Poole, H. A. Farach, R.J. Creswick, and Prozorov R. *Superconductivity*. Academic Press, Amsterdam; Boston, 2007.

[3] J. Bardeen, L. N. Cooper, and J. R. Schrieffer. Theory of superconductivity. *Phys. Rev.*, 108:1175, 1957.

[4] M. K. Wu, J. R. Ashburn, C. J. Torng, P. H. Hor, R. L. Meng, L. Gao, Z. J. Huang, Y. Q. Wang, and C. W. Chu. Superconductivity at 93 K in a new mixed-phase Y–Ba–Cu–O compound system at ambient pressure. *Phys. Rev. Lett.*, 58:908, 1987.

[5] M.R. Norman. The challenge of unconventional superconductivity. *Science*, 332:196, 2011.

[6] T. Imae, T. Kanaya, M. Furusaka, and N. Torikai, editors. *Neutrons in Soft Matter*. John Wiley & Sons, Inc., 2011.

[7] G.L. Squires. *Introduction to the Theory of Thermal Neutron Scattering*. Cambridge University Press, Cambridge; London; New York; Melbourn, 1978.

[8] S.J. Blundell. Spin - polarized muons in condensed matter physics. *Contemporary Physics*, 40(3):175, 1999.

[9] E.M. Forgan, R. Cubitt, M.T. Wylie, S.L. Lee, H. Keller, D.M^{c}K. Paul, M. Yethiraj, H.A. Mook, P.H. Kes, T.W. Li, A.A. Menovsky, Z. Tarnawski, N. Koshizuka, J. Ricketts, and K. Mortensen. Observation of the flux-line lattice by neutron diffraction and muon-spin rotation. In K. Yamafuji and T. Morishita, editors, *Advances in Superconductivity VII*. Springer Japan, 1995.

[10] A. D. Hillier, J. Quintanilla, and R. Cywinski. Evidence for time-reversal symmetry breaking in the noncentrosymmetric superconductor $LaNiC_2$. *Phys. Rev. Lett.*, 102:117007, 2009.

[11] V.L Ginzburg and L.D. Landau. *Zh. Exp. Teor. Fiz.*, 20:1064, 1950.

[12] M. Tinkham. *Introduction to superconductivity*. Dover Publications, Mineola, New York, 2004.

[13] L. Pitaevskii. Phenomenology and microscopic theory: Theoretical foundations. In K. Bennemann and J.B Ketterson, editors, *Superconductivity*. Springer, Berlin; London, 2008.

[14] V. Moshchalkov, M. Menghini, T. Nishio, Q. H. Chen, A. V. Silhanek, V. H. Dao, L. F. Chibotaru, N. D. Zhigadlo, and J. Karpinski. Type-1.5 superconductivity. *Phys. Rev. Lett.*, 102:117001, 2009.

[15] E. Babaev, J. Carlstrm, J. Garaud, M. Silaev, and J.M. Speight. Type-1.5 superconductivity in multiband systems: Magnetic response, broken symmetries and microscopic theory a brief overview. *Physica C*, 479:2, 2012.

[16] J. Carlström, J. Garaud, and E. Babaev. Semi-meissner state and nonpairwise intervortex interactions in type-1.5 superconductors. *Phys. Rev. B*, 84:134515, 2011.

[17] E.H. Brandt. The flux-line lattice in superconductors. *Rep. Prog. Phys.*, 58(11):1465, 1995.

[18] W. H. Kleiner, L. M. Roth, and S. H. Autler. Bulk solution of Ginzburg-Landau equations for type II superconductors: Upper critical field region. *Phys. Rev.*, 133:A1226, 1964.

[19] T. M. Riseman, P. G. Kealey, E. M. Forgan, A. P. Mackenzie, L. M. Galvin, A. W. Tyler, S. L. Lee, C. Ager, D. M^{c}K. Paul, and C. M. Aegerter. Observation of a square flux-line lattice in the unconventional superconductor Sr_2RuO_4. *Nature*, 404:629, 2000.

[20] R. Gilardi, J. Mesot, S. P. Brown, E. M. Forgan, A. Drew, S. L. Lee, R. Cubitt, C. D. Dewhurst, T. Uefuji, and K. Yamada. Square vortex lattice at anomalously low magnetic fields in electron-doped $Nd_{1.85}Ce_{0.15}CuO_4$. *Phys. Rev. Lett.*, 93:217001, 2004.

[21] U. Yaron, P. L. Gammel, A. P. Ramirez, D. A. Huse, D. J. Bishop, A. I. Goldman, C. Stassis, P. C. Canfield, K. Mortensen, and M. R. Eskildsen. Microscopic coexistence of magnetism and superconductivity in $ErNi_2B_2C$. *Nature*, 382:236, 1996.

[22] M. R. Eskildsen, K. Harada, P. L. Gammel, A. B. Abrahamsen, N. H. Andersen, G. Ernst, A. P. Ramirez, D. J. Bishop, K. Mortensen, D. G. Naugle, K. D. D. Rathnayaka, and P. C. Canfield. Intertwined symmetry of the magnetic modulation and the flux-line lattice in the superconducting state of $TmNi_2B_2C$. *Nature*, 393:242, 1998.

[23] M. Yethiraj, D. M^{c}K. Paul, C. V. Tomy, and E. M. Forgan. Neutron scattering study of the flux lattice in YNi_2B_2C. *Phys. Rev. Lett.*, 78:4849, 1997.

[24] F. Steglich, J. Aarts, C. D. Bredl, W. Lieke, D. Meschede, W. Franz, and H. Schafer. Superconductivity in the presence of strong Pauli paramagnetism: $CeCu_2Si_2$. *Phys. Rev. Lett.*, 43:1892, 1979.

[25] D. Jerome, A. Mazaud, M. Ribault, and K. Bechgaard. Superconductivity in a synthetic organic conductor $(TMTSF)_2PF_6$. *J. Phys. Lett. (Paris)*, 41(4):95, 1980.

[26] M. Sigrist and K. Ueda. Phenomenological theory of unconventional superconductivity. *Rev. Mod. Phys.*, 63:239, 1991.

[27] H.-R. Ott. High T_c superconductivity. In Z. Fisk and H.R. Ott, editors, *Superconductivity in new materials*. Elsevier, Amsterdam - Oxford, 2011.

[28] P.J. Ford and G.A. Saunders. *The rise of the superconductors*. CRC Press, London, 2005.

[29] D. R. Tilley and J. Tilley. *Superfluidity and Superconductivity*. Adam Hilger, Bristol, New York, 1990.

[30] F. Strocchi. *Symmetry Breaking*. Springer, 2008.

[31] J. Rosen. *Symmetry Rules: How Science and Nature are founded on Symmetry*. Springer, 2008.

[32] Y. Aoki, A. Tsuchiya, T. Kanayama, S. R. Saha, H. Sugawara, H. Sato, W. Higemoto, A. Koda, K. Ohishi, K. Nishiyama, and R. Kadono. Time-reversal symmetry-breaking superconductivity in heavy-fermion $PrOs_4Sb_{12}$ detected by muon-spin relaxation. *Phys. Rev. Lett.*, 91:067003, 2003.

[33] K. Maki. Gapless superconductivity. In R. D. Parks, editor, *Superconductivity in new materials*, volume 2. M. Dekker, New York, 1969.

[34] G. M. Luke, Y. Fudamoto, K. M. Kojima, M. I. Larkin, J. Merrin, B. Nachumi, Y. J. Uemura, Y. Maeno, Z. Q. Mao, Y. Mori, H. Nakamura, and M. Sigrist. Time-reversal symmetry-breaking superconductivity in Sr_2RuO_4. *Nature*, 394:558, 1998.

[35] A. Maisuradze, W. Schnelle, R. Khasanov, R. Gumeniuk, M. Nicklas, H. Rosner, A. Leithe-Jasper, Yu. Grin, A. Amato, and P. Thalmeier. Evidence for time-reversal symmetry breaking in superconducting $PrPt_4Ge_{12}$. *Phys. Rev. B*, 82:024524, 2010.

[36] L. Shu, W. Higemoto, Y. Aoki, A. D. Hillier, K. Ohishi, K. Ishida, R. Kadono, A. Koda, O. O. Bernal, D. E. MacLaughlin, Y. Tunashima, Y. Yonezawa, S. Sanada, D. Kikuchi, H. Sato, H. Sugawara, T. U. Ito, and M. B. Maple. Suppression of time-reversal symmetry breaking superconductivity in $Pr(Os_{1-x}Ru_x)_4Sb_{12}$ and $Pr_{1-y}La_yOs_4Sb_{12}$. *Phys. Rev. B*, 83:100504, 2011.

[37] G. M. Luke, A. Keren, L. P. Le, W. D. Wu, Y. J. Uemura, D. A. Bonn, L. Taillefer, and J. D. Garrett. Muon spin relaxation in UPt_3. *Phys. Rev. Lett.*, 71:1466, 1993.

[38] R. H. Heffner, D. W. Cooke, A. L. Giorgi, R. L. Hutson, M. E. Schillaci, H. D. Rempp, J. L. Smith, J. O. Willis, D. E. MacLaughlin, C. Boekema, R. L. Lichti, J. Oostens, and A. B. Denison. Muon spin rotation in the magnetic and superconducting ground states of (U,Th)Be_{13} and (U,Th)Pt_{13}. *Phys. Rev. B*, 39:11345, 1989.

[39] R. P. Singh, A.D. Hillier, B. Mazidian, J. Quintanilla, J. F. Annett, D. M^{c}K. Paul, G. Balakrishnan, and M. R. Lees. Detection of time-reversal symmetry breaking in the noncentrosymmetric superconductor Re_6Zr using muon-spin spectroscopy. *Phys. Rev. Lett.*, 112:107002, 2014.

[40] A. D. Hillier, J. Quintanilla, B. Mazidian, J. F. Annett, and R. Cywinski. Nonunitary triplet pairing in the centrosymmetric superconductor $LaNiGa_2$. *Phys. Rev. Lett.*, 109:097001, 2012.

[41] Manfred Sigrist, D.F. Agterberg, P.A. Frigeri, N. Hayashi, R.P. Kaur, A. Koga, I. Milat, K. Wakabayashi, and Y. Yanase. Superconductivity in

non-centrosymmetric materials. *J. Magn. Magn. Mater.*, 310(2, Part 1):536, 2007.

[42] R. S. Hayano, Y. J. Uemura, J. Imazato, N. Nishida, T. Yamazaki, and R. Kubo. Zero-and low-field spin relaxation studied by positive muons. *Phys. Rev. B*, 20:850, 1979.

[43] O.I. Bodak and E.P. Marusin. The crystal structure of $RNiC_2$ compounds (R = Ce, La, Pr). *Dopovidi Akademii Nauk Ukrains'koi RSR, Seriya A: Fiziko-Matematichni Ta Tekhnichni Nauki*, 41(12):1048, 1979.

[44] R. Gumeniuk, H. Borrmann, A. Ormeci, H. Rosner, W. Schnelle, M. Nicklas, Yu. Grin´, and A. Leithe-Jasper. Filled platinum germanium skutterudites MPt_4Ge_{12} (M = Sr, Ba, La-Nd, Sm, Eu): crystal structure and chemical bonding. *Z. Kristallog. - Crystalline Materials*, 225:531, 2010.

[45] K. Kaneko, N. Metoki, T. D. Matsuda, and M. Kohgi. Rattling of Pr in heavy-fermion superconductor $PrOs_4Sb_{12}$ revealed by neutron powder diffraction. *J. Phys. Soc. Jpn.*, 75(3):034701, 2006.

[46] J.S. Gardner, G. Balakrishnan, D.M^{c}K. Paul, and C. Haworth. Neutron diffraction and magnetisation studies of Sr_2RuO_4 below 2 K. *Physica C*, 265(34):251, 1996.

[47] B. Erdmann and C. Keller. The preparation of actinide - (zirconium and hafnium) - noble metal alloy phases by coupled reduction. *Inorganic and Nuclear Chemistry Letters*, 7:675, 1971.

[48] R. H. Heffner, J. L. Smith, J. O. Willis, P. Birrer, C. Baines, F. N. Gygax, B. Hitti, E. Lippelt, H. R. Ott, A. Schenck, E. A. Knetsch, J. A. Mydosh, and D. E. MacLaughlin. New phase diagram for (U,Th)Be_{13}: A muon-spin-resonance and H_{c1} study. *Phys. Rev. Lett.*, 65:2816, 1990.

[49] J.L. Smith, Z. Fisk, J.O. Willis, A.L. Giorgi, R.B. Roof, H.R. Ott, H. Rudigier, and E. Felder. Impurity effects in UBe_{13}. *Physica B+C*, 135(13):3, 1985.

[50] B.T. Matthias, V.B. Compton, and E. Corenzwit. Some new superconducting compounds. *J. Phys. Chem. Solids*, 19(12):130, 1961.

[51] Jorge Quintanilla, Adrian D. Hillier, James F. Annett, and R. Cywinski. Relativistic analysis of the pairing symmetry of the noncentrosymmetric superconductor $LaNiC_2$. *Phys. Rev. B*, 82:174511, 2010.

[52] W.H. Lee, H.K. Zeng, Y.D. Yao, and Y.Y. Chen. Superconductivity in the Ni based ternary carbide $LaNiC_2$. *Physica C*, 266(12):138, 1996.

[53] I. Bonalde, R. L. Ribeiro, K. J. Syu, H. H. Sung, and W. H. Lee. Nodal gap structure in the noncentrosymmetric superconductor $LaNiC_2$ from magnetic-penetration-depth measurements. *New J. Phys.*, 13(12):123022, 2011.

[54] A.P. Mackenzie and Y. Maeno. The superconductivity of Sr_2RuO_4 and the physics of spin-triplet pairing. *Rev. Mod. Phys.*, 75:657, 2003.

[55] M.-A. Measson, D. Braithwaite, J. Flouquet, G. Seyfarth, J. P. Brison, E. Lhotel, C. Paulsen, H. Sugawara, and H. Sato. Superconducting phase diagram of the filled skuterrudite $PrOs_4Sb_{12}$. *Phys. Rev. B*, 70:064516, 2004.

[56] E. Helfand and N. R. Werthamer. Temperature and purity dependence of the superconducting critical field, H_{c2}. II. *Phys. Rev.*, 147:288, 1966.

[57] N. R. Werthamer, E. Helfand, and P. C. Hohenberg. Temperature and purity dependence of the superconducting critical field, H_{c2}. III. electron spin and spin-orbit effects. *Phys. Rev.*, 147:295, 1966.

[58] S. V. Shulga, S.-L. Drechsler, G. Fuchs, K.-H. Müller, K. Winzer, M. Heinecke, and K. Krug. Upper critical field peculiarities of superconducting YNi_2B_2C and $LuNi_2B_2C$. *Phys. Rev. Lett.*, 80:1730, 1998.

[59] Sergey L. Bud'ko and Paul C. Canfield. Temperature-dependent H_{c2} anisotropy in MgB_2 as inferred from measurements on polycrystals. *Phys. Rev. B*, 65:212501, 2002.

[60] D. T. Adroja, A. D. Hillier, J.-G. Park, E. A. Goremychkin, K. A. McEwen, N. Takeda, R. Osborn, B. D. Rainford, and R. M. Ibberson. Probing the vortex state of $PrRu_4Sb_{12}$ through muon spin rotation and relaxation. *Phys. Rev. B*, 72:184503, 2005.

[61] V.H. Tran, A.D. Hillier, D.T. Adroja, and D. Kaczorowski. Muon spin rotation and relaxation studies of the filled skutterudite superconductor $ThPt_4Ge_{12}$. *J. Phys.: Condens. Matter*, 22(50):505701, 2010.

[62] V. K. Anand, A. D. Hillier, D. T. Adroja, A. M. Strydom, H. Michor, K. A. McEwen, and B. D. Rainford. Specific heat and μSR study on the noncentrosymmetric superconductor $LaRhSi_3$. *Phys. Rev. B*, 83:064522, 2011.

[63] E. Bauer, G. Rogl, Xing-Qiu Chen, R. T. Khan, H. Michor, G. Hilscher, E. Royanian, K. Kumagai, D. Z. Li, Y. Y. Li, R. Podloucky, and P. Rogl. Unconventional superconducting phase in the weakly correlated noncentrosymmetric Mo_3Al_2C compound. *Phys. Rev. B*, 82:064511, 2010.

[64] J. Chen, M. B. Salamon, S. Akutagawa, J. Akimitsu, J. Singleton, J. L. Zhang, L. Jiao, and H. Q. Yuan. Evidence of nodal gap structure in the noncentrosymmetric superconductor Y_2C_3. *Phys. Rev. B*, 83:144529, 2011.

[65] B. Mazidian, J. Quintanilla, A. D. Hillier, and J. F. Annett. Anomalous thermodynamic power laws near topological transitions in nodal superconductors. *Phys. Rev. B*, 88:224504, 2013.

[66] S. Kuroiwa, Y. Saura, J. Akimitsu, M. Hiraishi, M. Miyazaki, K. H. Satoh, S. Takeshita, and R. Kadono. Multigap superconductivity in sesquicarbides La_2C_3 and Y_2C_3. *Phys. Rev. Lett.*, 100:097002, 2008.

[67] I. Bonalde, R. L. Ribeiro, W. Brämer-Escamilla, G. Mu, and H. H. Wen. Possible two-gap behavior in noncentrosymmetric superconductor $Mg_{10}Ir_{19}B_{16}$: A penetration depth study. *Phys. Rev. B*, 79:052506, 2009.

[68] T. Klimczuk, F. Ronning, V. Sidorov, R. J. Cava, and J. D. Thompson. Physical properties of the noncentrosymmetric superconductor $Mg_{10}Ir_{19}B_{16}$. *Phys. Rev. Lett.*, 99:257004, 2007.

[69] K. Sugawara, T. Sato, S. Souma, T. Takahashi, and A. Ochiai. Anomalous superconducting-gap symmetry of noncentrosymmetric La_2C_3 observed by ultrahigh-resolution photoemission spectroscopy. *Phys. Rev. B*, 76:132512, 2007.

[70] E. Bauer, G. Hilscher, H. Michor, Ch. Paul, E. W. Scheidt, A. Gribanov, Yu. Seropegin, H. Noël, M. Sigrist, and P. Rogl. Heavy fermion superconductivity and magnetic order in noncentrosymmetric $CePt_3Si$. *Phys. Rev. Lett.*, 92:027003, 2004.

[71] M. Yogi, Y. Kitaoka, S. Hashimoto, T. Yasuda, R. Settai, T. D. Matsuda, Y. Haga, Y. Ōnuki, P. Rogl, and E. Bauer. Evidence for a novel state of superconductivity in noncentrosymmetric $CePt_3Si$: A ^{195}Pt-NMR study. *Phys. Rev. Lett.*, 93:027003, 2004.

[72] I. Bonalde, W. Brämer-Escamilla, and E. Bauer. Evidence for line nodes in the superconducting energy gap of noncentrosymmetric $CePt_3Si$ from magnetic penetration depth measurements. *Phys. Rev. Lett.*, 94:207002, 2005.

[73] N. Kimura, K. Ito, H. Aoki, S. Uji, and T. Terashima. Extremely high upper critical magnetic field of the noncentrosymmetric heavy fermion superconductor $CeRhSi_3$. *Phys. Rev. Lett.*, 98:197001, 2007.

[74] R. Settai, Y. Miyauchi, T. Takeuchi, F. Lévy, I. Sheikin, and Y. Ōnuki. Huge upper critical field and electronic instability in pressure-induced superconductor

$CeIrSi_3$ without inversion symmetry in the crystal structure. *J. Phys. Soc. Jpn.*, 77(7):073705, 2008.

[75] T. Akazawa, H. Hidaka, T. Fujiwara, T. C. Kobayashi, E . Yamamoto, Y. Haga, R. Settai, and Y. Ōnuki. Pressure-induced superconductivity in ferromagnetic UIr without inversion symmetry. *J. Phys.: Condens. Matter*, 16(4):L29, 2004.

[76] Z. Fisk and H.R. Ott, editors. *Superconductivity in new materials.* Elsevier, Amsterdam - Oxford, 2011.

[77] N. Plakida. *High-Temperature Cuprate Superconductors: Experiment, Theory, and Applications.* Springer, 2010.

[78] M. R. Norman and C. Pépin. The electronic nature of high temperature cuprate superconductors. *Rep. Prog. Phys.*, 66(10):1547, 2003.

[79] A. Ardavan, S. Brown, S. Kagoshima, K. Kanoda, K. Kuroki, H. Mori, M. Ogata, S. Uji, and J. Wosnitza. Recent topics of organic superconductors. *J. Phys. Soc. Jpn.*, 81(1):011004, 2012.

[80] A.Y. Ganin, Y. Takabayashi, P. Jeglič, D. Arčon, A. Potočnik, P.J. Baker, Y. Ohishi, M.T. McDonald, M.D. Tzirakis, A. McLennan, G.R. Darling, T. Masaki, M.J. Rosseinsky, and K. Prassides. Polymorphism control of superconductivity and magnetism in Cs_3C_{60} close to the Mott transition. *Nature*, 466(7303):221, 2010.

[81] M. Lang and J. Müller. Organic superconductors. In K.H. Bennemann and J.B. Ketterson, editors, *Superconductivity.* Springer Berlin Heidelberg, 2008.

[82] Z. Iqbal, R. H. Baughman, B. L. Ramakrishna, S. Khare, N. S. Murthy, H. J. Bornemann, and D. E. Morris. Superconductivity at 45 K in Rb/Tl codoped C_{60} and C_{60}/C_{70} mixtures. *Science*, 254(5033):826, 1991.

[83] O. Gunnarsson. Superconductivity in Fullerides. *Rev. Mod. Phys.*, 69:575, 1997.

[84] P. Coleman. Heavy fermions: Electrons at the edge of magnetism. In H. Kronmüller and S. Parkin, editors, *Handbook of magnetism and advance magnetic materials*, volume 1. John Wiley & Sons, 2007.

[85] G. R. Stewart. Heavy-fermion systems. *Rev. Mod. Phys.*, 56:755, 1984.

[86] J. D. Thompson and Z. Fisk. Progress in heavy-fermion superconductivity: Ce115 and related materials. *J. Phys. Soc. Jpn.*, 81(1):011002, 2012.

[87] E. Dagotto. *Colloquium*: The unexpected properties of alkali metal iron selenide superconductors. *Rev. Mod. Phys.*, 85:849, 2013.

[88] Y. Kamihara, T. Watanabe, M. Hirano, and H. Hosono. Iron-based layered superconductor La[$O_{1-x}F_x$]FeAs (x = 0.050.12) with T_c = 26 K. *J. Am. Chem. Soc.*, 130(11):3296, 2008.

[89] G. R. Stewart. Superconductivity in iron compounds. *Rev. Mod. Phys.*, 83:1589, 2011.

[90] D. C. Johnston. The puzzle of high temperature superconductivity in layered iron pnictides and chalcogenides. *Adv. Phys.*, 59(6):803, 2010.

[91] E. H. Brandt. Magnetic field density of perfect and imperfect flux line lattices in type II superconductors. I. Application of periodic solutions. *J. Low Temp. Phys.*, 73:355, 1988.

[92] AC arc furnace with auxiliary electromagnetic coil system for control of arc deflection. `http://www.freepatentsonline.com/6549557.html`. Accesed: 22/07/2014.

[93] R.P. Feynman, M.L Sands, and Leighton R. B. *The Feynman lectures on physics*, volume I. Pearson/Addison-Wesley, San Francisco, 2006.

[94] B. D. Cullity and S.R. Stock. *Elements of X-ray diffraction*. Prentice Hall, Upper Saddle River, N.J, 2001.

[95] The X-ray diffraction. `http://www2.warwick.ac.uk/fac/sci/physics/research/condensedmatt/x-ray/`. Accessed: 22/07/2014.

[96] J. Wormald. *Diffraction methods*. Clarendon Press, Oxford, 1973.

[97] C. Hammond. *Introduction to crystallography*. Oxford University Press, Oxford, 1992.

[98] CCP14 tutorials and examples. `http://www.ccp14.ac.uk/tutorial/lmgp/orientexpress.htm`. Accessed: 22/07/2014.

[99] Laboratory measurements. `http://www2.warwick.ac.uk/fac/sci/physics/research/condensedmatt/supermag/group_and_user_facilities/laboratory_measurements/`. Accessed: 22/07/2014.

[100] M. McElfresh. Fundamental of magnetism and magnetic measurements featuring Quantum Design's Magnetic Property Measurement System. Technical report, Quantum Design, 1994.

[101] Magnetic Property Measurement System. Technical report, Quantum Design, 2000.

[102] D. Martien. Introduction to: AC Susceptibility. Technical report, Quantum Design.

[103] Sub-two-kelvin Magnetic Measurement System iHelium3. `http://www.qdusa.com/sitedocs/productBrochures/IQuantum_brochure_LoRes_6-07-1.pdf`. Accessed: 22/07/2014.

[104] Physical Property Measurement System resistivity option user's manual. Technical report, Quantum Design, 1999.

[105] J.E. Sonier and S. Fraser. Muon spin rotation/relaxation/resonance μSR. http://www.chem.ubc.ca/sites/default/files/wysiwyg_uploads/affiliated-research-centres/musrbrochurefinal_april11.pdf, 2011. Accessed: 12/07/2014.

[106] A. Yaouanc and P. Dalmas de Réotier. *Muon spin rotation, relaxation, and resonance : applications to condensed matter.* Oxford University Press, Oxford ; New York, 2011.

[107] A. Schenck. *Muon spin rotation spectroscopy : principles and applications in solid state physics.* Hilger, Bristol, 1985.

[108] S.L. Lee, S.H. Kilcoyne, and R. Cywinski, editors. *Muon science: Muons in physics, chemistry and materials: proceedings of the fifty first Scottish universities summer school in physics, St. Andrews, August 1998.* Taylor & Francis Group, Abingdon, 1999.

[109] D.C. Walker. *Muon and muonium chemistry.* Cambridge University Press, Cambridge; New York, 1983.

[110] Dilution refrigerator. http://www.isis.stfc.ac.uk/instruments/musr/sample-environment/dilution-refrigerator8745.html. Accessed: 22/07/2014.

[111] S. Giblin. Practical aspects of μSR. http://www.isis.stfc.ac.uk/groups/muons/muon-training-school/2008-practical-aspects-spc7875.pdf, 2012. Accessed: 22/07/2014.

[112] P. K. Biswas, G. Balakrishnan, D. M^{c}K. Paul, M. R. Lees, and A. D. Hillier. Two-gap superconductivity in $Lu_2Fe_3Si_5$: A transverse-field muon spin rotation study. *Phys. Rev. B*, 83:054517, 2011.

[113] R. Khasanov, A. Shengelaya, I. M. Savić, C. Baines, and H. Keller. Comment on "Muon-spin-rotation study of the superconducting properties of Mo_3Sb_7". *Phys. Rev. B*, 82:016501, 2010.

[114] E. H. Brandt. Properties of the ideal Ginzburg-Landau vortex lattice. *Phys. Rev. B*, 68:054506, 2003.

[115] A. Sidorenko, V. Smilga, and V. Fesenko. Muonic study of type II superconductors. *Hyperfine Interact.*, 63:49, 1990.

[116] E.H. Brandt and A. Seeger. Muon-spin rotation as a tool for investigating the diffusion of positive muons in type-II superconductors. *Adv. Phys.*, 35(2):189, 1986.

[117] A.D. Sidorenko, V.P. Smilga, and V.I. Fesenko. μSR and determination of vortex lattice characteristics of anisotropic high-T_C superconductors. *Physica C*, 166:167, 1990.

[118] A. Furrer, editor. *Frontiers of Neutron Scattering: proceedings of the seventh Summer School on Neutron Scattering*. World Scientific, Singapure; New Jersey; London; Hong Kong, 2000.

[119] Description of the ILL HFR (high-flux reactor). `http://www.ill.eu/reactor-environment-safety/high-flux-reactor/technical-characteristics/`. Accessed: 22/07/2014.

[120] Large dynamic range small-angle diffractometer D22. `http://www.ill.eu/instruments-support/instruments-groups/instruments/d22/`. Accessed:22/07/2014.

[121] D22 manual. `http://www.ill.eu/instruments-support/instruments-groups/instruments/d22/more/documentation/d22-manual/`. Accessed: 22/07/2014.

[122] Characteristics. http://www.ill.eu/instruments-support/instruments-groups/instruments/d33/characteristics/. Accessed: 22/07/2014.

[123] A 3D drawing of d33. http://www.ill.eu/en/instruments-support/instruments-groups/instruments/d33/description/layout-3d/. Accesed: 22/07/2014.

[124] M. Laver, C. J. Bowell, E. M. Forgan, A. B. Abrahamsen, D. Fort, C. D. Dewhurst, S. Mühlbauer, D. K. Christen, J. Kohlbrecher, R. Cubitt, and S. Ramos. Structure and degeneracy of vortex lattice domains in pure superconducting niobium: A small-angle neutron scattering study. *Phys. Rev. B*, 79:014518, 2009.

[125] Discussion about published brightness evaluations of the ILL. http://www.ill.eu/fileadmin/users_files/img/instruments_and_support/support_facilities/computing_for_science/Computing_for_Science/Virtual_instruments_and_experiments/ILL_Brightness.pdf, 2011. Accessed: 22/07/2014.

[126] C. D. Dewhurst. GRASP - graphical reduction and analysis SANS program for Matlab®. http://www.ill.eu/instruments-support/instruments-groups/groups/lss/grasp/. Accessed: 22/07/2014.

[127] R. Cubitt, M. R. Eskildsen, C. D. Dewhurst, J. Jun, S. M. Kazakov, and J. Karpinski. Effects of two-band superconductivity on the flux-line lattice in magnesium diboride. *Phys. Rev. Lett.*, 91:047002, 2003.

[128] A. D. Bianchi, M. Kenzelmann, L. DeBeer-Schmitt, J. S. White, E. M. Forgan, J. Mesot, M. Zolliker, J. Kohlbrecher, R. Movshovich, E. D. Bauer, J. L. Sarrao, Z. Fisk, C. Petrovi, and M. R. Eskildsen. Superconducting vortices in $CeCoIn_5$: Toward the Pauli-limiting field. *Science*, 319(5860):177, 2008.

[129] Y. Matsuda and H. Shimahara. Fulde–Ferrell–Larkin–Ovchinnikov state in heavy fermion superconductors. *J. Phys. Soc. Jpn.*, 76(5):051005, 2007.

[130] J. V. Florio, N. C. Baenziger, and R. E. Rundle. Compounds of thorium with transition metals. II. Systems with iron, cobalt and nickel. *Acta Crystallogr.*, 9(4):367, 1956.

[131] B.T. Matthias, V.B. Compton, and E. Corenzwit. Some new superconducting compounds. *J. Phys. Chem. Solids*, 19(12):130 – 133, 1961.

[132] S. K. Malik, W. E. Wallace, and T. Takeshita. Hydrogen induced change from superconducting to magnetically ordered state in Th_7Fe_3. *Solid State Commun.*, 28(5):359, 1978.

[133] S. Rayaprol, V. Siruguri, A. Hoser, P. Henry, and E. V. Sampathkumaran. Neutron diffraction studies on an exotic magnetic system, Nd_7Rh_3. *J. Phys.: Conference Series*, 340(1):012064, 2012.

[134] K. Sengupta and E. V. Sampathkumaran. Field-induced first-order magnetic phase transition in an intermetallic compound Nd_7Rh_3: Evidence for kinetic hindrance, phase coexistence, and percolative electrical conduction. *Phys. Rev. B*, 73(2), 2006.

[135] K. Sengupta, S. Rayaprol, and E. V. Sampathkumaran. Large magnetoresistance anomalies in Dy_7Rh_3. *J. Phys.: Condens. Matter*, 16(45):L495, 2004.

[136] K. Sengupta, S. Rayaprol, and E. V. Sampathkumaran. Large magnetoresistance in the magnetically ordered state as well as in the paramagnetic state near 300 K in an intermetallic compound, Gd_7Rh_3. *Europhys. Lett.*, 69(3):454, 2005.

[137] K. Sengupta, K.K. Iyer, and E.V. Sampathkumaran. Magnetic and magnetoresistance behavior of Tb_7Rh_3, an intermetallic compound with a negative

temperature coefficient of electrical resistivity in the paramagnetic state. *Solid State Commun.*, 139(7):351, 2006.

[138] A. Tanaka, Y. Haga, T. Tsutaoka, and T. Shigeoka. Magnetic and electrical properties of Pr_7Ni_3 single crystal. *J. Phys.: Conference Series*, 150(4):042203, 2009.

[139] K. Umeo, T. Takabatake, H. Ohmoto, T. Pietrus, H. v. Lohneysen, K. Koyama, S. Hane, and T. Goto. Low-temperature specific heat and magnetic susceptibility near the pressure-induced quantum phase transition in Ce_7Ni_3. *Phys. Rev. B*, 58(18):12095, 1998.

[140] T. Tsutaoka and A. Tanaka. Pressure effect on the magnetic transitions in Nd_7Ni_3 single crystal. *J. Phys.: Conference Series*, 150(4):042219, 2009.

[141] V. H. Tran, A. D. Hillier, D. T. Adroja, and Z. Bukowski. Muon-spin-rotation study of the superconducting properties of Mo_3Sb_7. *Phys. Rev. B*, 78:172505, 2008.

[142] V. H. Tran, A. D. Hillier, and D. T. Adroja. Reply to "Comment on 'Muon-spin-rotation study of the superconducting properties of Mo_3Sb_7' ". *Phys. Rev. B*, 82:016502, 2010.

[143] R. Khasanov, P. W. Klamut, A. Shengelaya, Z. Bukowski, I. M. Savić, C. Baines, and H. Keller. Muon-spin rotation measurements of the penetration depth of the Mo_3Sb_7 superconductor. *Phys. Rev. B*, 78:014502, 2008.

[144] J. L. Smith, J. C. Lashley, H. M. Volz, R. A. Fisher, and P. S. Riseborough. Thermodynamics and superconductivity of the Th_7(Fe, Ru, Os, Co, Rh, Ir)$_3$ system. *Philos. Mag.*, 88(18-20):2847, 2008.

[145] P. Pedrazzini, G. Schmerber, M. Gmez Berisso, J.P Kappler, and J.G Sereni. Magnetic and superconducting properties of A_7B_3 compounds (A=Th or La and B=Ni, Co, Fe or Pd, Rh, Ru). *Physica C*, 336(12):10, 2000.

[146] E. Talik, M. Klimczak, R. Troc, J. Kusz, W. Hofmeister, and A. Damm. Comparison of the magnetic properties of Gd_7T_3 (T=Pd and Rh) single crystals. *J. Alloys Compd.*, 427(1-2):30, 2007.

[147] E. Talik, M. Klimczak, R. Troc, J. Kusz, Wolfgang Hofmeister, and A. Winiarski. Comparison of magnetic and transport properties of Gd_6YPd_3 and Gd_7Pd_3 single crystals. *J. Alloys Compd.*, 460(12):1, 2008.

[148] B. Aronsson. The crystal structure of Ru_7B_3. *Acta Chem. Scand.*, 13:109–114, 1959.

[149] M. Khachfi, E. Bauer-Grosse, J. P. Morniroli, T. Lundstroem, and M. Gantois. Microstructural study of borides of the type Ru_7B_3. Relationships with M_7C_3 carbides. *Wegliki, Azotki, Borki, Miedzynar. Konf., 3rd*, page 40, 1984.

[150] L. Fang, H. Yang, X. Zhu, G. Mu, Z.-S. Wang, L. Shan, C. Ren, and H.-H. Wen. Physical properties of the non-centrosymmetric superconductor Ru_7B_3. *Phys. Rev. B*, 79:144509, 2009.

[151] N. Kase and J. Akimitsu. Superconducting state of the binary boride Ru_7B_3 with the non-centrosymmetric crystal structure. *J. Phys. Soc. Jpn.*, 78(4):044710, 2009.

[152] A.J. Blake and W. Clegg. *Crystal structure analysis: Principles and practice.* Oxford University Press, Oxford, 2009.

[153] B.D. Rainford and G.J. Daniell. μsr frequency spectra using the maximum entropy method. *Hyperfine Interact.*, 87(1):1129, 1994.

[154] A. Carrington and F. Manzano. Magnetic penetration depth of MgB_2. *Physica C*, 385(12):205, 2003.

[155] H. Padamsee, J.E Neighbor, and C.A. Shiffman. Quasiparticle phenomenology for thermodynamics of strong-coupling superconductors. *J. Low Temp. Phys.*, 12(3-4):387, 1973.

[156] R.P. Singh, N.A. Parzyk, M.R. Lees, D.M^{c}K. Paul, and G. Balakrishnan. Crystal growth and properties of the non-centrosymmetric superconductor, Ru_7B_3. *J. Cryst. Growth*, 395:22, 2014.

[157] G. Balakrishnan, M.R. Lees, and D.M^{c}K. Paul. Growth of large single crystals of rare earth hexaborides. *J. Cryst. Growth*, 256(12):206, 2003.

[158] M. R. Eskildsen, L. Ya. Vinnikov, T. D. Blasius, I. S. Veshchunov, T. M. Artemova, J. M. Densmore, C. D. Dewhurst, N. Ni, A. Kreyssig, S. L. Bud'ko, P. C. Canfield, and A. I. Goldman. Vortices in superconducting $Ba(Fe_{0.93}Co_{0.07})_2As_2$ studied via small-angle neutron scattering and Bitter decoration. *Phys. Rev. B*, 79:100501, 2009.

[159] P. K. Biswas, M. R. Lees, G. Balakrishnan, D. Q. Liao, D. S. Keeble, J. L. Gavilano, N. Egetenmeyer, C. D. Dewhurst, and D. M^{c}K. Paul. First-order reorientation transition of the flux-line lattice in CaAlSi. *Phys. Rev. Lett.*, 108:077001, 2012.

[160] L. J. Campbell, M. M. Doria, and V. G. Kogan. Vortex lattice structures in uniaxial superconductors. *Phys. Rev. B*, 38:2439, 1988.

[161] M. R. Eskildsen, P. L. Gammel, B. P. Barber, A. P. Ramirez, D. J. Bishop, N. H. Andersen, K. Mortensen, C. A. Bolle, C. M. Lieber, and P. C. Canfield. Structural stability of the square flux line lattice in YNi_2B_2C and $LuNi_2B_2C$ studied with small angle neutron scattering. *Phys. Rev. Lett.*, 79:487, 1997.

[162] V.M. Ionov, N.A. Tomilin, A.E. Prozorovskii, A.N. Klimenko, Yu.V. Titov, S.G. Zhukov, and G.V. Fetisov. Anisotropy of physical properties and crystal structure of Pd Bi in the intervall 293-570 K. *Kristallografiya*, 34:829, 1989.

[163] Y.C Bhatt and K Schubert. Kristallstruktur von PdBi.r. *J. Less-Common Met.*, 64(2):P17, 1979.

[164] N.N. Zhuravlev. Structure of superconductors. X. thermal, microscopic and X-ray investigation of the bismuth-palladium system. *Zh. Eksp. Teor. Fiz.*, 5:1064, 1957.

[165] B. Joshi, A. Thamizhavel, and S. Ramakrishnan. Superconductivity in non-centrosymmetric BiPd. *Phys. Rev. B*, 84:064518, 2011.

[166] L. Jiao, J. L. Zhang, Y. Chen, Z. F. Weng, Y. M. Shao, J. Y. Feng, X. Lu, B. Joshi, A. Thamizhavel, S. Ramakrishnan, and H. Q. Yuan. Anisotropic superconductivity in noncentrosymmetric BiPd. *Phys. Rev. B*, 89:060507, 2014.

[167] M. Mondal, B. Joshi, S. Kumar, A. Kamlapure, S. Ch. Ganguli, A. Thamizhavel, S. S. Mandal, S. Ramakrishnan, and P. Raychaudhuri. Andreev bound state and multiple energy gaps in the noncentrosymmetric superconductor BiPd. *Phys. Rev. B*, 86:094520, 2012.

[168] T. Graf, C. Felser, and S.S.P. Parkin. Simple rules for the understanding of Heusler compounds. *Prog. Solid State Chem.*, 39(1):1, 2011.

[169] J. Winterlik, G. H. Fecher, C. Felser, M. Jourdan, K. Grube, F. Hardy, H. von Löhneysen, K. L. Holman, and R. J. Cava. Ni-based superconductor: Heusler compound $ZrNi_2Ga$. *Phys. Rev. B*, 78:184506, 2008.

[170] Shinya Waki, Yuji Yamaguchi, and Kazuyoshi Mitsugi. Superconductivity of Ni_2NbX (X = Al, Ga and Sn). *J. Phys. Soc. Jpn.*, 54(5):1673, 1985.

[171] A. D. Hillier, N. Parzyk, and D. Mck Paul. Probing the superconducting state of the Heusler supercoductor: $ZrNi_2Ga$. *ArXiv e-prints*, 2012, 1206.1182.

[172] J.H. Wernick, G.W. Hull, T.H. Geballe, J.E. Bernardini, and J.V. Waszczak. Superconductivity in ternary Heusler intermetallic compounds. *Materials Letters*, 2(2):90, 1983.

[173] J. Winterlik, G.H. Fecher, and C. Felser. Electronic and structural properties of palladium-based Heusler superconductors. *Solid State Commun.*, 145(910):475, 2008.

[174] M.A.S. Boff, G.L.F. Fraga, D.E. Brand ao, and A.A. Gomes. Specific heat of $Ni_2(Nb_{1x}T_x)Sn$, T = Ti, Ta, superconducting Heusler compounds. *J. Magn. Magn. Mater.*, 153(12):135, 1996.

[175] R. N. Shelton, L. S. Hausermann-Berg, M. J. Johnson, P. Klavins, and H. D. Yang. Coexistence of superconductivity and long-range magnetic order in $ErPd_2Sn$. *Phys. Rev. B*, 34:199, 1986.

[176] H. A. Kierstead, B. D. Dunlap, S. K. Malik, A. M. Umarji, and G. K. Shenoy. Coexistence of ordered magnetism and superconductivity in Pd_2YbSn. *Phys. Rev. B*, 32:135, 1985.

[177] W. Ming, Y. Liu, W. Zhang, J. Zhao, and Y. Yao. First-principles study of the electronic, vibrational, electronphonon interaction and thermodynamics properties of $ZrNi_2Ga$. *J. Phys.: Condens. Matter*, 21(7):075501, 2009.

[178] V.Y. Markiv and A.I. Storozhenko. Investigation of Zr-Ni-Ga and Zr-Cu-Ga systems. *Izvestiya Akademii Nauk SSSR, Metally*, 4:151, 1974.

[179] V.Y. Markiv, Y.V. Voroshilov, P.I. Kripyakevich, and E.E. Cherkashin. New compounds of the $MnCu_2Al$ and $MgZn_2$ types containing alummiunum and gallium. *Kristallografiya*, 9(5):619, 1964.

[180] M. I. Tsindlekht, G. I. Leviev, I. Asulin, A. Sharoni, O. Millo, I. Felner, Y. B. Paderno, V. B. Filippov, and M. A. Belogolovskii. Tunneling and magnetic characteristics of superconducting ZrB_{12} single crystals. *Phys. Rev. B*, 69(21):212508, 2004.

[181] Y. Wang, R. Lortz, Y. Paderno, V. Filippov, S. Abe, U. Tutsch, and A. Junod. Specific heat and magnetization of a ZrB_{12} single crystal: Characterization of a type-II/I superconductor. *Phys. Rev. B*, 72(2):024548, 2005.

[182] P.K. Biswas. *Studies of Unconventional Superconductors*. PhD thesis, University of Warwick, June 2012.

[183] V. I. Matkovich, J. Economy, and R. Barrett. The structure of metallic dodecarborides. *Acta Crystallogr.*, 19(6):1056, 1965.

[184] D. Daghero, R. S. Gonnelli, G. A. Ummarino, A. Calzolari, V. Dellarocca, V. A. Stepanov, V. B. Filippov, and Y. B. Paderno. Andreev-reflection spectroscopy in ZrB_{12} single crystals. *Supercon. Sci. Technol.*, 17(5):S250, 2004.

[185] B. T. Matthias, T. H. Geballe, K. Andres, E. Corenzwit, G. W. Hull, and J. P. Maita. Superconductivity and antiferromagnetism in boron-rich lattices. *Science*, 159(3814):530, 1968.

[186] R. Lortz, Y. Wang, S. Abe, C. Meingast, Y. B. Paderno, V. Filippov, and A. Junod. Specific heat, magnetic susceptibility, resistivity and thermal expansion of the superconductor ZrB_{12}. *Phys. Rev. B*, 72(2):024547, 2005.

[187] R. Khasanov, D. Di Castro, M. Belogolovskii, Y. Paderno, V. Filippov, R. Brutsch, and H. Keller. Anomalous electron-phonon coupling probed on the surface of superconductor ZrB_{12}. *Phys. Rev. B*, 72(22):224509, 2005.

[188] J. Teyssier, A. B. Kuzmenko, D. van der Marel, F. Marsiglio, A. B. Liashchenko, N. Shitsevalova, and V. Filippov. Optical study of electronic structure and electron-phonon coupling in ZrB_{12}. *Phys. Rev. B*, 75(13):134503, 2007.

[189] I. R. Shein and A. L. Ivanovskii. Band structure of superconducting dodecaborides YB_{12} and ZrB_{12}. *Physics of the Solid State*, 45(8):1429, 2003.

[190] V. A. Gasparov, N. S. Sidorov, and II Zverkova. Two-gap superconductivity in ZrB_{12}: Temperature dependence of critical magnetic fields in single crystals. *Phys. Rev. B*, 73(9):094510, 2006.

[191] S. Thakur, D. Biswas, N. Sahadev, P.K. Biswas, G. Balakrishnan, and K. Maiti. Complex spectral evolution in a BCS superconductor, ZrB_{12}. *Sci. Rep.*, 3, 2013.

[192] V. G. Kogan, M. Bullock, B. Harmon, P. Miranovic, Lj. Dobrosavljevic-Grujic, P. L. Gammel, and D. J. Bishop. Vortex lattice transitions in borocarbides. *Phys. Rev. B*, 55:R8693, 1997.

[193] Y. De Wilde, M. Iavarone, U. Welp, V. Metlushko, A. E. Koshelev, I. Aranson, G. W. Crabtree, and P. C. Canfield. Scanning tunneling microscopy observation of a square abrikosov lattice in $LuNi_2B_2C$. *Phys. Rev. Lett.*, 78:4273, 1997.

[194] D. M^{c}K. Paul, C. V. Tomy, C. M. Aegerter, R. Cubitt, S. H. Lloyd, E. M. Forgan, S. L. Lee, and M. Yethiraj. Nonlocal effects and vortex lattice transitions in YNi_2B_2C. *Phys. Rev. Lett.*, 80:1517, 1998.

[195] C. D. Dewhurst, S. J. Levett, and D. M^{c}K. Paul. Vortex-lattice symmetry near T_c in YNi_2B_2C. *Phys. Rev. B*, 72:014542, 2005.

[196] E.H. Brandt. The stability of triangular and square flux-line lattices in type-II superconductors. *Phys. Lett. A*, 38(2):71, 1972.

[197] V. G. Kogan, A. Gurevich, J. H. Cho, D. C. Johnston, Ming Xu, J. R. Thompson, and A. Martynovich. Nonlocal electrodynamics and low-temperature magnetization of clean high–κ superconductors. *Phys. Rev. B*, 54:12386, 1996.

[198] V. G. Kogan, P. Miranovic, Lj. Dobrosavljevic-Grujic, W. E. Pickett, and D. K. Christen. Vortex lattices in cubic superconductors. *Phys. Rev. Lett.*, 79:741, 1997.

[199] M. Yethiraj, H. A. Mook, G. D. Wignall, R. Cubitt, E. M. Forgan, D. M^{c}K. Paul, and T. Armstrong. Small-angle neutron scattering study of flux line lattices in twinned $YBa_2Cu_3O_7$. *Phys. Rev. Lett.*, 70:857, 1993.

[200] I. Grillo. Small-angle neutron scattering and applications in soft condensed matter. In R. Borsali and R. Pecora, editors, *Soft-matter characterization*. Springer, Netherlands, 2008.

[201] A. Brûlet, D. Lairez, A. Lapp, and J.-P. Cotton. Improvement of data treatment in small-angle neutron scattering. *J. Appl. Cryst.*, 40(1):165, 2007.

[202] J. M. Densmore, P. Das, K. Rovira, T. D. Blasius, L. DeBeer-Schmitt, N. Jenkins, D. M^{c}K. Paul, C. D. Dewhurst, S. L. Bud'ko, P. C. Canfield, and M. R. Eskildsen. Small-angle neutron scattering study of the vortex lattice in superconducting $LuNi_2B_2C$. *Phys. Rev. B*, 79:174522, 2009.

[203] A. De Bonis, A. Santagata, J.V. Rau, A. Latini, T. Mori, L. Medici, and R. Teghil. Two-phase zirconium boride thin film obtained by ultra-short pulsed laser ablation of a ZrB_{12} target. *Appl. Surf. Sci.*, 283:715, 2013.

[204] T. M. Rice. The future of superconductivity viewed through a cloudy crystal ball. In Z. Fisk and H.R. Ott, editors, *Superconductivity in new materials*. Elsevier, Amsterdam - Oxford, 2011.